Progress in Nuclear Magnetic Resonance Spectroscopy 109 (2018) 1–50

Contents lists available at ScienceDirect

Progress in Nuclear Magnetic Resonance Spectroscopy

journal homepage: www.elsevier.com/locate/pnmrs

Pros and cons of ultra-high-field MRI/MRS for human application

Mark E. Ladd [a,b,c,d,*], Peter Bachert [a,c], Martin Meyerspeer [e,f], Ewald Moser [e,f], Armin M. Nagel [a,g], David G. Norris [h,d], Sebastian Schmitter [a,i], Oliver Speck [j,k,l,m], Sina Straub [a], Moritz Zaiss [n]

[a] *Medical Physics in Radiology, German Cancer Research Center (DKFZ), Heidelberg, Germany*
[b] *Faculty of Medicine, University of Heidelberg, Heidelberg, Germany*
[c] *Faculty of Physics and Astronomy, University of Heidelberg, Heidelberg, Germany*
[d] *Erwin L. Hahn Institute for MRI, University of Duisburg-Essen, Essen, Germany*
[e] *Center for Medical Physics and Biomedical Engineering, Medical University of Vienna, Vienna, Austria*
[f] *MR Center of Excellence, Medical University of Vienna, Vienna, Austria*
[g] *Institute of Radiology, University Hospital Erlangen, Friedrich-Alexander-Universität Erlangen-Nürnberg (FAU), Erlangen, Germany*
[h] *Donders Institute for Brain, Cognition and Behaviour, Radboud University Nijmegen, Nijmegen, Netherlands*
[i] *Physikalisch-Technische Bundesanstalt (PTB), Braunschweig and Berlin, Germany*
[j] *Department of Biomedical Magnetic Resonance, Otto-von-Guericke-University Magdeburg, Magdeburg, Germany*
[k] *German Center for Neurodegenerative Diseases, Magdeburg, Germany*
[l] *Center for Behavioural Brain Sciences, Magdeburg, Germany*
[m] *Leibniz Institute for Neurobiology, Magdeburg, Germany*
[n] *High-Field Magnetic Resonance Center, Max-Planck-Institute for Biological Cybernetics, Tübingen, Germany*

Edited by David Gadian and David Neuhaus

ARTICLE INFO

Article history:
Received 6 March 2018
Accepted 7 June 2018
Available online 8 June 2018

Keywords:
MRI
MRS
Ultra-high field
7 Tesla
Human

ABSTRACT

Magnetic resonance imaging and spectroscopic techniques are widely used in humans both for clinical diagnostic applications and in basic research areas such as cognitive neuroimaging. In recent years, new human MR systems have become available operating at static magnetic fields of 7 T or higher ($\geq$300 MHz proton frequency). Imaging human-sized objects at such high frequencies presents several challenges including non-uniform radiofrequency fields, enhanced susceptibility artifacts, and higher radiofrequency energy deposition in the tissue. On the other side of the scale are gains in signal-to-noise or contrast-to-noise ratio that allow finer structures to be visualized and smaller physiological effects to be detected. This review presents an overview of some of the latest methodological developments in human ultra-high field MRI/MRS as well as associated clinical and scientific applications. Emphasis is given to techniques that particularly benefit from the changing physical characteristics at high magnetic fields, including susceptibility-weighted imaging and phase-contrast techniques, imaging with X-nuclei, MR spectroscopy, CEST imaging, as well as functional MRI. In addition, more general methodological developments such as parallel transmission and motion correction will be discussed that are required to leverage the full potential of higher magnetic fields, and an overview of relevant physiological considerations of human high magnetic field exposure is provided.

Contents

---

* Corresponding author at: Medical Physics in Radiology, German Cancer Research Center (DKFZ), Im Neuenheimer Feld 280, 69120 Heidelberg, Germany.
E-mail addresses: mark.ladd@dkfz.de (M.E. Ladd), p.bachert@dkfz.de (P. Bachert), martin.meyerspeer@meduniwien.ac.at (M. Meyerspeer), ewald.moser@meduniwien.ac.at (E. Moser), armin.nagel@uk-erlangen.de (A.M. Nagel), david.norris@donders.ru.nl (D.G. Norris), sebastian.schmitter@ptb.de (S. Schmitter), oliver.speck@ovgu.de (O. Speck), sina.straub@dkfz.de (S. Straub), moritz.zaiss@tuebingen.mpg.de (M. Zaiss).

https://doi.org/10.1016/j.pnmrs.2018.06.001
0079-6565/

1. Introduction

Magnetic resonance imaging (MRI) is a form of nuclear magnetic resonance (NMR) that uses magnetic field gradients to generate images. In the early 1970s, Damadian published a promising report showing that the NMR characteristics of malignant tumor tissue, in particular T1 and T2 relaxation times, differed from normal tissue [1]. This led to the prospect that in some way a useful diagnostic method based on hydrogen (^{1}H) NMR might arise. The practical recording of images based on magnetic resonance was subsequently made possible by the work of Lauterbur [2] as well as Mansfield and Grannell [3]. They applied a position-dependent magnetic field (gradient) in addition to the static background magnetic field. Due to the linear dependence of the resonance frequency of the nuclear spin on the external magnetic field and with the aid of Fourier analysis, it became feasible to quickly reconstruct the spatial distribution of the spins within a slice in the form of a 2D image. For this work, which led to the birth of MRI, Lauterbur and Mansfield shared the Nobel Prize in Medicine in 2003.

Since the introduction of MRI into clinical use in the early 1980s, this technique has developed into a widespread medical imaging method for depicting a variety of anatomical regions and answering a large range of morphological and functional questions. Within a short period, this imaging method has emerged as one of the most important diagnostic examination methods in medical imaging and continues to expand its role to this day. In a survey around the turn of the century, physicians were asked to classify the 30 most important developments in medicine in the last 25 years [4]. Number one on this list were the sectional imaging methods MRI and computed tomography (CT).

The significance of MRI in modern diagnostics is demonstrated by the ever-increasing number of imagers installed all over the world. Although MRI was not established into clinical settings until the early to mid-1980s, there are now more than 40,000 installations worldwide (8520 in the US in 2016 [5]), most of them with a magnetic field strength of 1.5 or 3 T. MRI has become one of the most flexible tools in diagnostic imaging; in 2015 an estimated 39 million MRI examinations were conducted in the USA. The annual growth rate is around 4% since 2011 [5], although this development is part of a general trend toward more imaging studies in the diagnosis and treatment of patients [6].

Despite manifold technical advances in recent years, the low sensitivity of MRI remains a significant limitation. In most relevant situations for human imaging, the measurement noise is dominated by the sample and not by the measurement hardware. Thus, the most promising approach for overcoming fundamental limits in the signal-to-noise ratio (SNR) is to increase the spin polarization of the sample. This can be achieved by injecting exogenous substances that have been prepared by a number of hyperpolarization techniques [7–9], but there is great interest in utilizing higher static magnetic fields to increase the thermal equilibrium spin polarization of the entire sample in vivo.

Although until recently 3 T was the highest clinical field strength available, higher magnetic fields up to 9.4 T have been explored under appropriate ethical permission for neuroscientific and clinical research since the late 1990s [10–12]. For the purposes of this article, we will consider any magnetic field strength $\geq$7 T to be “ultra-high field” or UHF. The first system in this range was the 8 T system at Ohio State University in 1998 [13], followed closely by the first 7 T system at the University of Minnesota in 1999 [14]. In the meantime, there are over 70 systems with field strengths at or above 7 T available for human research. The large majority of these systems are operating at 7 T (300 MHz Larmor proton resonant frequency), with a handful operating at 9.4 T (400 MHz proton resonant frequency). The first 7 T system with approval as a medical device entered the market in 2017 [15], so the number of UHF systems is expected to increase even more rapidly in the coming years.

The purpose of this article is to introduce the challenges that have been encountered when applying such high magnetic fields to human MRI as well as provide an overview of some of the methodological improvements that have been achieved to address these challenges. Primarily, however, our goal is to present the promise and potential of imaging at higher magnetic fields. Given the large number of research groups with access to UHF MRI systems, there have now been numerous pilot investigations demonstrating the potential to capture extraordinary information in the context of fundamental research questions regarding healthy physiology, pathological processes, and brain function.

1.1. Advantages and disadvantages of UHF MRI/MRS

Table 1 summarizes a variety of physical characteristics that affect MR imaging and MR spectroscopy (MRS) at high magnetic fields. In a few cases the changes in these parameters are decisively positive. In a few other cases the changes can be considered decisively negative. However, for a majority of the changes the impact depends on the goal of the underlying imaging experiment and the particular method used: in some cases the effect is beneficial, in others a hindrance. As almost any given experiment is affected by a complex interplay between multiple parameters, it is not possible to directly translate approaches from lower fields strengths without adjusting and optimizing imaging parameters and where necessary introducing new imaging hardware to achieve the full potential at UHF. Thus, it is typical that several years transpire after the introduction of a new field strength before its full impact can be appreciated.

1.1.1. SNR – sensitivity

The most striking positive change with field strength that is also most widely named when justifying the expense and effort of pursuing higher magnetic fields is SNR. The thermal equilibrium spin polarization for nuclei with spin nuclear number I is given by:

$$\rho_0 \frac{\gamma^2 \hbar^2 I(I+1)}{3kT} B_0 \tag{1}$$

In this equation ρ_0 is the spin density, γ the gyromagnetic ratio, $\hbar$ is the Planck constant divided by 2π, k is Boltzmann’s constant, T is the absolute temperature, and B_0 is the polarizing static magnetic field. The equilibrium polarization depends linearly on the polarizing field. To determine the impact on SNR, it is necessary to account for the oscillating voltage that can be induced in a detector coil by the precessing magnetization as well as the frequency dependence of the noise associated with signal reception. The final result is in particular dependent on whether the noise is dominated by the

Table 1
A partial overview of potential pros and cons when increasing the magnetic field strength. Note that the consequences – pro or con – may depend on technical and anatomical details. Modified and expanded from [24].

Characteristic	Trend as $B_0 \uparrow$	Pro	Con
SNR	$\uparrow$	Higher resolution, shorter scan time, X-nuclei feasible	None
SAR	$\uparrow$	None	Fewer slices, smaller flip angle, longer TR, longer breathhold
Physiological side-effects	$\uparrow$	None	Dizziness, nausea, metallic taste
Relaxation times	T1 $\uparrow$[a]	TOF, ASL, cardiac tagging	Longer scan time
	T2 $\downarrow$[b]		DWI, DTI
	$T2^* \downarrow$	SWI, BOLD	
RF field uniformity	$\downarrow$	Parallel reception Parallel transmission	Position-dependent flip angle, poor inversion, unexpected contrast
Susceptibility effects	$\uparrow$	BOLD, SWI, $T2^*$	Geometric distortions, intravoxel dephasing
Chemical shift	$\uparrow$	Fat saturation, CEST, MR spectroscopy	Fat/water and metabolite misregistration

[a] Although for most applications T1 increases with B_0, an increasing contribution from chemical shift anisotropy can also result in a decrease in T1 relaxation times (e.g. in ^{31}P MRS; cf. Section 6.1).

[b] Although for most applications T2 decreases with B_0, for quadrupolar nuclei T2 can also increase with field strength (cf. Section 6.1).

sample or by the system hardware. As already mentioned, the measurement noise is dominated by the sample in most situations relevant for human imaging.

For the case of sample-dominated noise, early work demonstrated that SNR increases linearly with B_0 [16,17]. This linear increase has been experimentally confirmed for hydrogen at lower field strengths, e.g. 0.12–1.5 T [18]. One of the key assumptions made at these lower frequencies is the quasi-static approximation. Consider the full form of Ampere's law:

$$\oint_C \vec{H}\cdot d\vec{l} = \iint_S \left(\vec{J}+\frac{\partial}{\partial t}\vec{D}\right)\cdot d\vec{s} \tag{2}$$

In the quasi-static regime, only currents in conductors $\vec{J}$ are taken into consideration, and displacement currents $\vec{D}$ are ignored [19]. In this case, no fields can detach from the sources and propagate. For lower static fields B_0, the electrical size of typical MR-related RF problems is considered small because of the long wavelength. The phase distribution of the fields can be assumed uniform, and effects from phase delays can be neglected. Thus, aside from a phase offset due to dielectric losses in the body tissue, the time dependency of the fields is in phase with the time dependency of the sources, e.g. the RF currents in the transmit coils, and no constructive or destructive interference associated with propagating waves occurs.

For higher static fields and, thus, higher Larmor frequencies, the electrical size increases and a transition from the quasi-stationary regime to the electromagnetic regime takes place. In the electromagnetic regime Ampère's law is extended to take into account contributions to the magnetic field associated with the displacement current density D in addition to the magnetic field linked with the electric current density in electric conductors. The displacement current density explains why electromagnetic fields can detach from sources and propagate in space under certain conditions. An electromagnetic wave is thus formed by electric and magnetic fields interdependently produced by time-dependent changes in the other type of field.

If the complete Maxwell equations are considered as is necessary at UHF, the variation of SNR with field strength becomes a complex function of object size, object shape, and object composition. In general, most derivations lead to a more than linear increase in SNR with field strength in the UHF regime above 3 T. Unfortunately, it is quite difficult to perform experimental comparisons between field strengths due to differences in radiofrequency (RF) coils and other hardware considerations. An interesting concept that provides very useful theoretical insight is ultimate intrinsic SNR (uiSNR) [20]. This calculation provides the maximum theoretically achievable SNR for a particular object sample independent of any prescribed RF coil geometry, while enforcing compatibility with Maxwell's equations. Thus, the calculation is not constrained by any practical considerations that might hamper the realization of a physical receive coil.

Initial calculations of uiSNR targeted cylinders or elliptic cylinders [20–22], half spaces [22], or spheres [21]. In all cases these targets were composed of a material with uniform dielectric properties. Only recently has it become feasible using numerical techniques to examine more realistic sample geometries that consider the actual shape of the human head and its composition [23]. This work indicates a field-strength dependence that varies with the position within the head. For voxels near the surface of the head, the SNR increases roughly linearly. For deeper-lying voxels, the increase is more than linear (Fig. 1). For voxels near the center of the head, the SNR increases roughly with a power factor ${B_0}^x$, where x is approximately 2.1; near the surface, x is only approximately 1.2 [23].

This variation is compatible with experimental observations made comparing SNR at 3 T, 7 T, and 9.4 T, where a power dependency of x = 1.65 was found [25]. An interesting finding of [23] was

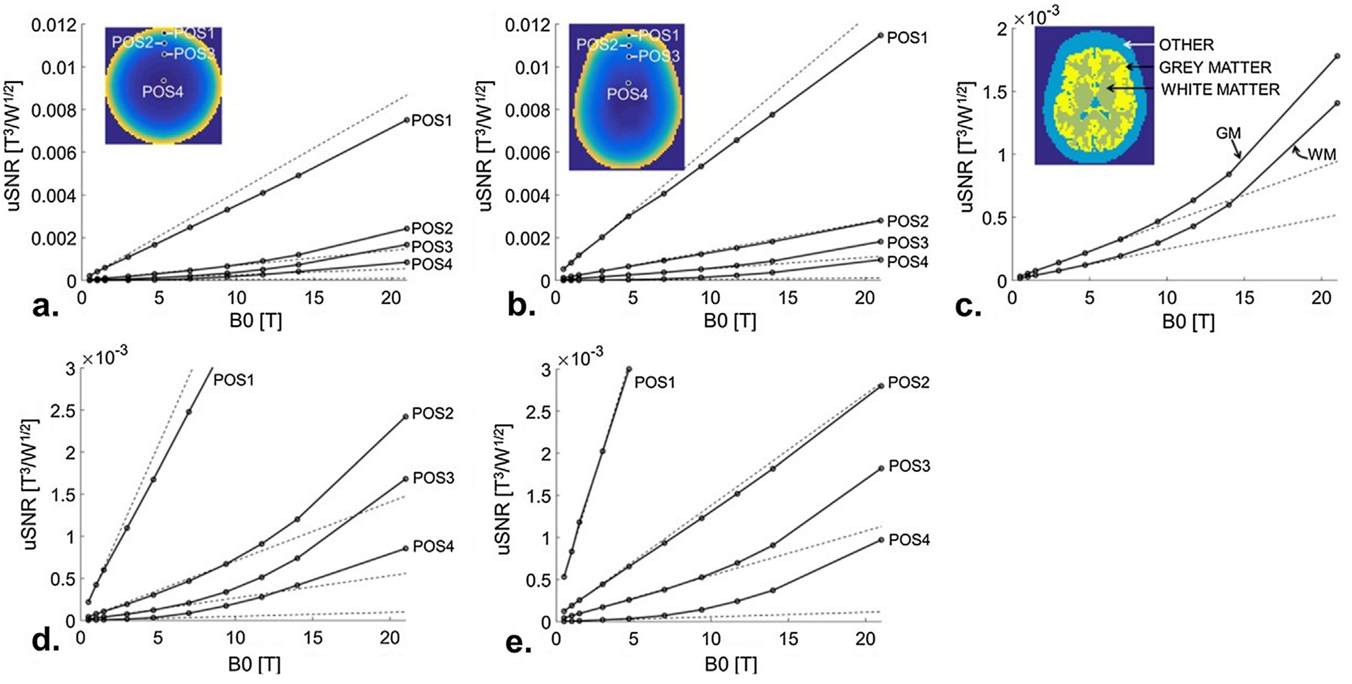

Fig. 1. SNR (linear scale) as a function of position and field strength in a uniform sphere as computed with the dyadic Green's function method. (d) Same figure as (a), but with the y-axis scaled differently to zoom in on the inner positions. (b) Same as (a), but in the Duke head model [28], computed with the generalized uiSNR approach. (e) Same as (b), but with the y-axis scaled differently to zoom in on the inner positions. (c) Gray matter and white matter averages of the uiSNR in Duke as a function of field strength. For figures (a), (b), (d), and (e), the positions #1, #2, #3, and #4 are located at 1, 2, 3, and 9 cm away from the top edge of the sphere/head. For all figures, the dashed black lines show linear uiSNR extrapolations at low field. Reproduced from [23].

that the SNR increase is also dependent on the parallel imaging acceleration factor. At higher acceleration factors, the advantage of higher field strengths is larger than for non-accelerated imaging. This can be intuitively explained by observing that the minimum achievable geometry factor of the receive coil array decreases with field strength concurrent with the increase in SNR [23].

The increase in SNR associated with higher magnetic fields benefits almost every existing application. The elevated SNR can be invested into higher spatial resolution (cf. e.g. Section 4.2) or into higher temporal resolution in the case of dynamic processes. At 7 T, a spatial resolution of 200 μm has been achieved for applications such as time-of-flight (TOF) angiography [26] or 250 μm for whole-brain T1-weighted structural imaging [27].

Although such improvements in existing applications are certainly promising, improved SNR can also bring new applications into the scope of feasibility for basic research or even clinical diagnostics. For practical reasons, MRI examinations involving human subjects are typically limited to a time window of about 1 h. Subjects are not willing or able to remain in the imager for significantly longer times. This constraint is particularly important in the clinical context, where patients are often older and suffering from physical ailments that limit their ability to lie still for extended times.

Among all the nuclei found in the human body that have a non-zero nuclear spin (e.g., ^{1}H, ^{13}C, ^{17}O, ^{19}F, ^{23}Na, ^{31}P), hydrogen is by far the dominant nucleus of interest for clinical MRI. Not only is the ^{1}H nucleus particularly common (in water, which makes up about 73% of the fat-free mass of the human body, but also in fat, proteins, and sugars), but in addition ^{1}H has a particularly high gyromagnetic ratio γ leading to a strong interaction with external magnetic fields. These characteristics imply that ^{1}H images with sufficient SNR can be obtained in a reasonably short time. Higher magnetic fields can improve the sensitivity of MR enough to open up applications involving spectroscopic analysis of metabolites such as ^{1}H and ^{31}P (cf. Sections 7 and 8) or direct imaging of other nuclei like ^{17}O, ^{23}Na, and ^{35}Cl (cf. Section 6).

1.1.2. CNR – specificity

For diagnostic imaging, in many cases SNR turns out not to be the most relevant parameter to characterize the ability of MRI to detect lesions of interest. A more direct measure is given by the contrast-to-noise ratio (CNR):

$$\frac{S_2 - S_1}{noise} \tag{3}$$

where S_2 is the signal within the lesion, S_1 is the signal in the surrounding healthy tissue, and *noise* is the noise of the acquisition. The clinical value of MRI is in large part based on the availability of several different physical parameters that can be leveraged to modify the acquired signal. Almost all clinically relevant diagnostic applications of MRI are based on the contrast produced by the different magnetic properties of hydrogen nuclei (protons) in different biochemical environments. Even if one is restricted to hydrogen, the obtained MRI signal thus depends on a large number of physical properties in the tissue [29,30]. This makes MRI extremely versatile and is in stark contrast to other biomedical imaging methods that can primarily present only a single physical parameter of the tissue. In MRI, a wide range of morphological and functional information such as diffusion, perfusion, flow rates, temperature, magnetic susceptibility, etc. can be obtained.

Given the large number of imaging parameters that are dependent on field strength (see Table 1), it is possible to identify MRI applications that particularly profit from an increase in magnetic field strength because they benefit not only from the underlying increase in SNR but also from an increase in tissue contrast. A prime example is given by functional MRI (fMRI, cf. Section 9), which provides mapping of areas of cortical activation when subjects perform particular cognitive or motor tasks. Most of these studies rely on the blood-oxygen-level-dependent (BOLD) contrast [31], which is provoked by changes in $R_2{}^*$ relaxation related to changes in the oxygenation level of blood. The expected double benefit of higher SNR and increased sensitivity to tissue susceptibility χ through changes in $R_2{}^*$ for fMRI was actually a prime driver for pursuing UHF imagers in the early years [14,32].

Applications that benefit from supralinear increases in CNR due to elevated susceptibility sensitivity include not only fMRI (cf. Section 9) but also susceptibility-weighted imaging (SWI) and quantitative susceptibility mapping (QSM) (cf. Section 5). Another positive example of a synergistic parameter change at higher magnetic fields is the lengthening of tissue T_1 relaxation times; the resulting enhanced background suppression benefits several techniques such as TOF (cf. Section 4.2), arterial spin labeling (ASL), and cardiac tagging.

A full discussion of each of the parameters in Table 1 is beyond the scope of this review. Nevertheless, several of them and their impact on UHF imaging will be discussed in greater detail in the following sections. Before getting into specific MR techniques and their applications, we begin with a discussion of the physiological effects of high static magnetic field exposure (cf. Section 2) followed by an introduction to parallel transmission (cf. Section 3), which is one of the most promising methodological developments to address issues with the transmit RF field that emerge at high Larmor frequencies.

2. Physiological considerations

Since it involves the application of only non-ionizing electromagnetic fields, MR has been considered a non-invasive modality since its first application in human subjects and animals. This does not imply that the electromagnetic fields used have no effects on living organisms, and indeed exposure limits for static magnetic, gradient, and radiofrequency fields have been established, mainly to avoid unpleasant sensory effects such as nerve stimulation and tissue damage due to RF heating. Thus, non-invasiveness stands for the absence of negative health effects or side effects outlasting the MR examination.

With regard to the three basic electromagnetic fields utilized in MRI, the most obvious difference at UHF is the higher static magnetic field. The gradient magnetic fields are comparable to those used at lower fields, and the same exposure limits apply at UHF as at lower field strengths [33,34]. These limits are chosen to largely avoid stimulation of peripheral nerves during gradient switching [35,36]. For RF fields, the goal is to avoid excessive heating in the electrically conducting tissue caused by the electric field. Also here, the limits are unchanged versus lower magnetic field strengths, although there are several issues that are particular to UHF that need to be considered [19]. One of the most important differences versus lower field strengths is that it is much more likely that foci of RF heating will occur due to the shorter wavelength. Thus, limits for local specific absorption rate (SAR) are considered for all transmit RF coils, and these limits are generally more constraining than the limits for whole or partial body SAR [19]. To comply with the regulatory limits, it is often necessary to adjust imaging and spectroscopic sequence parameters, for instance by lengthening the repetition time or reducing the number of acquired slices, which is one of the greatest practical challenges at UHF.

When moving to UHF, exposure to higher static magnetic fields is obviously required. Consequently, a central concern is possible physiological effects of high static magnetic fields. These include effects that may be induced by movement through the static magnetic field, which introduces a time dependency. Such effects can be categorized into transitory effects that disappear immediately or shortly after exposure and into permanent effects that have long-term negative health consequences. Obviously, the latter are of greatest concern and will be discussed in Section 2.2, but the former are also of relevance to daily system operation and will be discussed in the following section.

2.1. Vestibular and other transient effects

It has long been known that static magnetic fields can introduce transient physiological effects including dizziness, nausea, magnetophosphenes, or metallic taste [37]. The emphasis here is on the transient nature of the effects; they are expected to vanish either immediately after termination of exposure to the static magnetic field or within a relatively short period of time thereafter. A further well-known effect is distortion of the electrocardiogram when in high magnetic fields, characterized in particular by an elevated T-wave, which corresponds to the cardiac phase in which the electrically-conducting blood is being pumped at high speed through the aortic arch [38,39]. Such electrocardiogram changes can make imaging sequences that are dependent on cardiac triggering or gating difficult to realize at UHF.

A related concern is that the blood pressure might be elevated due to the additional effort required to transport blood through the static magnetic field. Early modeling studies predicted that this effect would present a practical barrier to MRI examinations at 10 T or higher [40]. However, more accurate modeling of the magnetohydrodynamic equations that accounts for magnetic fields generated in the flowing fluid indicates that a 10 T field changes the pressure in human vasculature by less than 0.2% [38]; multiple experimental investigations of blood pressure changes during exposure of humans or large animals to high magnetic fields have not revealed any relevant effects at field strengths up to 9.4/10.5 T [41,42]. Any differences between exposed and non-exposed are below changes related to postural changes, e.g. between standing and lying down.

In addition to the aforementioned effects, about which there is consensus that they can be induced by exposure to UHF systems, there are ongoing investigations about transient cognitive effects. Here the literature is unclear, and there are reports of positive correlations with field exposure [43–45] as well as reports in which no correlation could be found [41,46–48]. Mechanistically, magnetic-field-associated vertigo and nausea are believed to be related to interactions with the vestibular system. Similar to motion sickness, the disturbance of the vestibular organ leads to an incongruence between sensory information being received from the vestibular, proprioceptive, and visual systems [49,50]. Cognitive tests may thus reveal a definite effect due to the disturbance of the vestibular system [45,51].

When the first UHF systems became available, there were concerns that unpleasant transient effects such as vertigo and nausea might lower the willingness of subjects to undergo an examination. These effects have been studied extensively at 7 T and 9.4 T, and although the reports of side effects are higher than at lower magnetic fields, the effects do not significantly affect the acceptance of the technique [37,52]. In a multi-center study, only 1% of participants reported that they would be unwilling to undergo a further UHF MRI examination [52]. However, the most often reported sources of discomfort were exam duration, acoustic noise, and the need to lie still, i.e. sources not directly related to the magnetic field strength [52].

Transient effects may be more relevant to workers exposed to the magnetic field of the MRI (cf. Section 2.3). Although most occupational exposure scenarios involve magnetic fields much lower than at the isocenter of the magnet, workers performing system maintenance or cleaning the interior of the system might be exposed to very high magnetic fields. Of particular concern are possible cognitive effects. Both for patients and workers, investigations continue regarding the extent and duration of any cognitive effects. Even short-term effects might require advisories to avoid certain activities such as driving immediately after magnetic field exposure.

2.2. DNA effects

For ionizing radiation, such as X-rays, the detrimental biologic effects including long-term effects are well established and on a cellular level are often characterized by DNA damage. DNA damage includes single-base errors, single-strand breaks (SSB), and double-strand breaks (DSB). The first two can be repaired very effectively due to the presence of the undamaged second strand. DSB, however, are more difficult to repair and can lead to cell death via apoptosis or even to cell degeneration and cancerogenesis. Free radicals (mainly OH^-) generated through the interaction of high-energy photons with tissue water are the main damage mechanism.

Established markers for the detection and visualization of DNA DSB are the γ-H2AX (gamma histone 2AX) assay or formation of micronuclei. DNA DSB induction can result in post-translational modification of the histone tail, such as phosphorylation of the histone variant H2AX (γ-H2AX). Due to its sensitivity, efficiency, and mechanistic relevance, this assay allows detection of individual cells and visualization of discrete γ-H2AX foci [53–55]. Several different mechanisms can be involved in the formation of micronuclei. Micronuclei containing chromosome fragments may result from direct DNA DSB or conversion of DNA SSB to DSB after cell replication, or from inhibition of DNA synthesis [56].

While the current discussion about possible effects of MRI on DNA is not directly related to UHF, the B_0 field exposure does increase, and most methods require more RF energy at higher field strength. The SAR limits for RF are identical for all field strengths, albeit with higher RF frequency, i.e. higher photon quantum energy. Magnetic field gradients (slew rate and strength) are similar across field strengths. Nevertheless, most researchers and regulatory bodies may be more concerned about DNA effects at higher field strength, and thus careful consideration is indicated.

Only a few studies have examined the potential impact of MRI on DNA. The results are inconsistent and even contradictory in part. Four studies evaluated SSB or the formation of micronuclei in human blood lymphocytes with variable findings [57–60]. Two out of seven studies that investigated DNA DSB before and after MRI exposure of either blood cells in vitro or of blood cells after in-vivo exposure reported increased γ-H2AX staining [61–67]. While Fichter et al. reported significant DSB increases immediately after contrast-enhanced cardiac MRI at 1.5 T, Lancellotti et al. detected no increase in DSB markers 1 and 2 h after non-contrast-enhanced cardiac MRI but did detect an increase after 2 days and 1 month. Concerns have been raised regarding the absence of positive and negative control groups in some studies and the contribution of other potential DSB-inducing factors that are difficult to control. The in-vitro and in-vivo studies with the largest subject groups, the highest field strength (up to 7 T), and inclusion of frequently exposed subjects did not find any significant changes in either γ-H2AX or micronuclei formation [61,64,65]. In a recent publication, the authors note that this latter evidence “may serve as a means to put an end to this controversy” and thus conclude that DNA damage induced by MRI up to a field strength of 7 T is not a relevant concern [68].

Evidence from experimental studies can never prove the absence of an effect but only estimate lower effect limits. It is important to also perform research into potential damage mechanisms and improve our understanding of the interactions between the electromagnetic fields involved in MRI and relevant biological molecules and cells. No strong hypotheses regarding DNA damage mechanisms from exposure to low-energy electromagnetic fields have been proposed. It may be insightful to consider the energies involved in MR. On a molecular level, the photon quantum energy is most relevant for direct interaction mechanisms. While the ionization or excitation energies in molecules, such as H_2O or DNA, are on the order of 1 eV, the RF quantum energy at 7 T (about 10^{-6} eV) is 6 orders of magnitude smaller and about 10,000 times smaller than the Boltzmann thermal energy equivalent at body temperature (about 27 meV). It may be, however, that direct MRI-related induction of DNA damage does not occur at all, but that repair of continuously ongoing DNA lesions is altered through low-frequency electromagnetic fields as applied in MRI. This is speculative, and no specific altered repair mechanism has been proposed nor experimental evidence presented; on the other hand, it can equally not be excluded.

From the most current scientific reports, three recent reviews [69–71], and the recent statement from the International Commission on Non-Ionizing Radiation Protection (ICNIRP) [72], it can be concluded that potential effects of MRI on DNA damage are very much smaller than for ionizing radiation. If such effects exist at all, they are close to the detection limit of the most sensitive methods that are currently available or similar to naturally occurring variations in DNA DSB due to everyday activities. Therefore, the current practice of performing medically indicated MR examinations for diagnostic purposes does not require reconsideration. Potential effects may be of more concern for research applications of MRI in humans, where no direct benefit for the subject is present. However, no reliable evidence exists that indicates the need to change the current practice of including research subjects into MRI studies.

Hundreds of millions of patients have been examined with MRI to date as well as tens of thousands of subjects at 7 T with an excellent safety record. For the even higher magnetic field strengths available in the future, larger studies with the statistical power to exclude even small effects may be required and may further increase our confidence in the safe application of lower field MRI.

2.3. Occupational exposure

When considering MRI examinations, typical exposure scenarios can be subdivided into clinical exposure, research exposure, and occupational exposure. Clinical exposure refers to the exposure of a human patient during an MR examination that is medically indicated. In this case, the risk-benefit ratio will be much different than for subjects who undergo a research examination for which they have no direct personal benefit. Occupational exposure for workers is particularly critical, since they also do not have a direct personal benefit from the examination, and they are likely to be exposed repeatedly over a period of years during their employment lifetime.

In the European Union, minimum standards for occupational exposure have been set for electromagnetic exposure covering a large frequency range that includes the static magnetic field, the gradient magnetic fields, and the RF fields used in MRI [73]. These exposure limits apply for workers across all sectors of the economy and are not restricted to MRI or medical diagnostic scenarios. They equally apply for the radiation technologists performing the examinations, physicians, cleaning personnel, service personnel from the imager manufacturer, and any other workers who may be in the examination room during an active examination or at other times when only the static magnetic field is on.

At UHF, the only significant exposure change is the static magnetic field, as the regulatory limits for gradient magnetic field and RF exposure remain unchanged at higher magnetic field strength. The EU Electromagnetic Field Directive [73] prescribes the following upper limits for static magnetic field exposure: 2 T for normal working conditions, 8 T for localized exposure of the limbs, and 8 T for controlled working conditions. For all work procedures that do not involve approaching the opening of the magnet or reaching into the bore of the magnet, it is straightforward to demonstrate compliance. For some service and maintenance tasks or for cleaning the inside of the magnet bore, these limits may become relevant, requiring special documentation of work procedures to avoid overexposure. The directive additionally provides a derogation permitting even higher exposure than the above limits in the case of MRI-related work procedures if particular prerequisites are fulfilled.

It should be noted that the limits of the aforementioned directive were chosen to address possible short-term effects of occupational exposure. The directive explicitly “does not address suggested long-term effects of exposure to electromagnetic fields, since there is currently no well-established scientific evidence of a causal relationship” [73].

3. Parallel transmission

3.1. Technical aspects

A major challenge on the path to clinical UHF MRI is to cope with the spatial magnitude and phase variations of the magnetic (B_1^+) and electric (E) field components of the transmitter RF fields. These variations are caused by the shortened RF wavelengths compared to lower fields that become similar to the spatial dimensions of the human head and body at UHF. While spatial variations in B_1^+, particularly local B_1^+ voids, affect the signal and the contrast of the MR image, variations in the E-field lead to local peaks in the SAR and, therefore, to localized heating of the tissue as mentioned in the previous section. Many proposed techniques attempt to reduce such variations, while others aim at modulating the variations over the course of an MRI acquisition.

Many approaches that address spatial B_1^+ variations are linked to changes and progress in RF coil design. State-of-the-art head coils with a single transmit (Tx) and up to 32 receive (Rx) channels are commercially available that sufficiently limit B_1^+ field variations over the whole brain and thus enable a large range of applications in the head at 7 T. Although similar approaches exist for the body, a single-channel RF coil that allows for high-quality imaging of different organs with varying location and size currently does not exist and therefore other techniques are needed. This is one of the reasons why the progress in UHF body MRI has been fairly slow compared to progress in UHF head imaging.

A promising route for body imaging as well as for further enhanced image quality in the head is the use of multi-Tx-channel coils with typically 8 but also 16 or more transmitting channels. Such coils allow for transmitting N independent RF pulses on the N Tx channels, a method that is termed parallel transmission (pTx) [74–76]. It is the complex superposition $B_1^+(\mathrm{r},t) = \sum_{n=1}^{N} B_{1,n}^+(\mathrm{r},t) = \sum_{n=1}^{N} b_n(t) S_n(\mathbf{r})$ of the complex fields $B_{1,n}^+(\mathrm{r},t)$ generated by the N coil elements with transmit sensitivity $S_n(\mathbf{r})$ driven by RF pulses $b_n(t)$ that determines the interaction with the magnetization; therefore, modifying $b_n(t)$ can be used to achieve spatiotemporal steering of the resulting B_1^+ fields. In practice, two different approaches are applied: static pTx, often also termed “B_1^+ shimming”, and dynamic pTx.

In B_1^+ shimming [16] the RF pulse of each channel $b_n(t) = w_n \cdot b(t)$ consists of a shared, channel-independent RF pulse shape $b(t)$, such as a sinc-shaped pulse, weighted by a time-independent amplitude and phase term $w_n = a_n e^{i\phi_n}$. In the case of a fixed amplitude $a_n = a$, the term "B_1^+ phase shimming" is often used. Thus, the spatiotemporal field $B_1^+(\mathrm{r}, t) = b(t)\sum_{n=1}^{N} w_n S_n(\mathbf{r})$ separates into a spatial field term $S(r) = \sum_{n=1}^{N} w_n S_n(\mathbf{r})$ multiplied by the time-dependent RF pulse b(t). The aim is to optimize $S(\mathbf{r})$ within a region of interest by finding a shim set $\mathbf{w} = (w_1, .., w_N)^T$ with optimal a_n and ϕ_n, while the pulse properties of b(t) such as slice selectivity are not affected by shimming. For the optimization, the transmit sensitivity maps $S_n(r)$ of each channel need to be measured via B_1^+ or flip angle mapping methods, which will be explained in more detail later.

B_1^+ shimming is often applied to mitigate the B_1^+ field heterogeneity within a given region of interest, similar to B_0 shimming. The heterogeneity is quantified for example by the root-mean-square error (RMSE) between actual and desired field pattern or by the coefficient of variation (CV) of the achieved B_1^+ field pattern. From a practical view, the success of homogeneous shimming inversely scales with size of the target ROI: for small ROIs such as the prostate or a localized brain region, B_1^+ (phase) shimming achieves not only homogeneous B_1^+ magnitudes but also a high transmit efficiency, i.e. high B_1^+ values per input voltage. For larger organs such as the liver or the whole brain, the technique typically either fails or it results in poor transmit efficiency. For such cases the time-interleaved acquisition of modes (TIAMO) method [77] is a useful alternative, as it acquires two (or more) identical scans but with different B_1^+ shim weights, with the resulting images being merged to achieve a single image without B_1^+ dropouts and with diminished contrast variations. Besides achieving homogeneous excitation patterns, B_1^+ shimming can also be used to maximize the transmit efficiency within a given ROI by co-aligning the individual complex $B_{1,n}^+$ fields within that ROI.

It should be noted that for the B_1^+ shimming optimizations, only relative B_1^+ phase maps and not absolute B_1^+ maps of each channel are needed, which is advantageous as the relative maps can be quickly acquired within a few seconds with high quality. For conventional, non-adiabatic RF pulses, the B_1^+ shim set does not affect the properties of the pulse such as the slice selectivity or the bandwidth, and B_1^+ shimming can be applied independently without modifications of the sequence itself.

In some cases, different shim settings w_n are required for different RF pulses within the same pulse sequence (excitation, refocusing, inversion, saturation, and others), for example when they target different ROIs or when different requirements in terms of homogeneity or efficiency exist. Here, the shim set remains constant during a given RF pulse, but it is toggled between pulses. This technique is sometimes termed "dynamic B_1^+ shimming" [78], but it should not be confused with dynamic pTx.

In contrast to static pTx, the RF pulses in dynamic pTx do not share a common pulse shape $b(t)$. Here, either the weights w_n change over the course of an RF pulse or N entirely independent RF pulses $b_n(t)$ are applied to the system. Furthermore, the goal in dynamic pTx is not to manipulate the resulting B_1^+ field but the resulting flip angle. The flip angle, however, which is described by the Bloch equations, depends on the applied B_1^+ field, the local B_0 field, as well as the gradient trajectory that is switched over the course of the excitation. A burden for RF pulse design is given by the non-linearity of the Bloch equation, which can be addressed for small flip angles by applying the small-tip-angle approximation (STA). In this case, the excitation profile can be described by a Fourier transform of the weighted gradient trajectory, as demonstrated by Pauly et al. [79]. The formulation has been extended for the pTx case in the "spatial domain method" [80], which serves as the basis for many RF pulse designs that are described in more detail in [81]. In pTx, not only are the N RF pulse shapes $b_n(t)$ typically optimized during the design process, but also the gradient trajectory G(t). Furthermore, the pulse design typically considers maps of the local static magnetic field B_0 that are measured in vivo at the beginning of each session. In practice, dynamic pTx is applied for global (non-selective) excitation, for slice or slab-selective excitation, and for 2D or 3D local excitation.

"pTx spokes RF pulses" [82,83] are a frequently-used technique for slice-selective dynamic pTx (Fig. 2). Here, the RF pulse consists of a train of S slice-selective sub-pulses (spokes), e.g. sinc pulses, including their slice-selection gradients; for each of the sub-pulses a different shim set $\mathbf{w}^s$ (s = 1..S) is applied that remains constant during the sub-pulse but changes between sub-pulses. In addition to the slice-selection gradients that can be played out either in monopolar or bipolar fashion, small gradient blips are played out between sub-pulses typically orthogonal to the slice-selection direction. As a result, the excitation k-space trajectory consists of several spokes in the k_z direction that are distributed in the $k_x k_y$-plane.

The spokes RF pulse train is inherently slice selective, independent of $\mathbf{w}^s$ and the gradient blips, which has the substantial practical advantage that the acquisition of 2D B_1^+ maps (and corresponding 2D B_0 maps) covering the slice of interest is sufficient for the RF pulse design. During the optimization process, optimal values for the different $\mathbf{w}^s$ as well as for the spokes locations in the $k_x k_y$-plane are found that, for example, maximize the flip angle homogeneity within a target region of the slice.

Spokes pulses were used initially in combination with a single-Tx (N = 1) system [82] and then later extended to parallel transmission at UHF [83]. The optimal number of spokes depends on the number of transmit channels, the target size, the field strength, on the desired excitation fidelity, and on other parameters, with practical values typically ranging between 2 and 4 spokes. In practice, either the RF pulse duration increases with the number of spokes and/or the gradients must be switched more rapidly, which can impact the excitation fidelity. For spokes as for other dynamic pTx techniques, a precise synchronization between the RF pulses and gradients is needed, which may require additional calibration steps [84,85]. Spoke pulses are not restricted to 2D slice selection; they have also been applied to 3D slab-selective excitations, where the optimization in addition addressed flip angle variations in the slab direction.

Spoke pulses have been combined with simultaneous multi-slice imaging (SMS), also termed "multiband imaging" [86–89]. Here, multiple slices are excited simultaneously and the images of the individual slices are reconstructed from an aliased image of all slices through knowledge of the sensitivity patterns of multiple receiving coils. pTx allows optimization of slice-specific pTx RF pulses, which are subsequently summed up for simultaneous imaging of all slices [89]. A comprehensive summary of different SMS techniques, including pTx, is provided by [88].

Another class of relevant dynamic pTx RF pulses are the so-called "kt-points pulses" [90] that allow for homogeneous 3D excitations. The principle of kt-points pulses is similar to spokes pulses (see Fig. 2). The train of slice-selective RF pulses is replaced by non-selective, rectangular pulses that are applied without concurrent switching of a gradient. The gradient blips between the rectangular pulses can occur in all three spatial directions, which results in a 3D excitation where RF energy is deposited at distinct positions in excitation k-space. As for the spokes RF pulses, the combination of different shim settings $\mathbf{w}$ for each kt-point as well as the gradient switching is used to achieve a homogeneous flip angle. kt-points are typically applied for whole-brain imaging, and an increasing number of kt-points typically improves the excitation fidelity. Practical numbers range between 3 and 5 for the head.

A drawback of this method is that the RF pulse design requires B_1^+ maps of the entire 3D region with sufficient coverage, which can

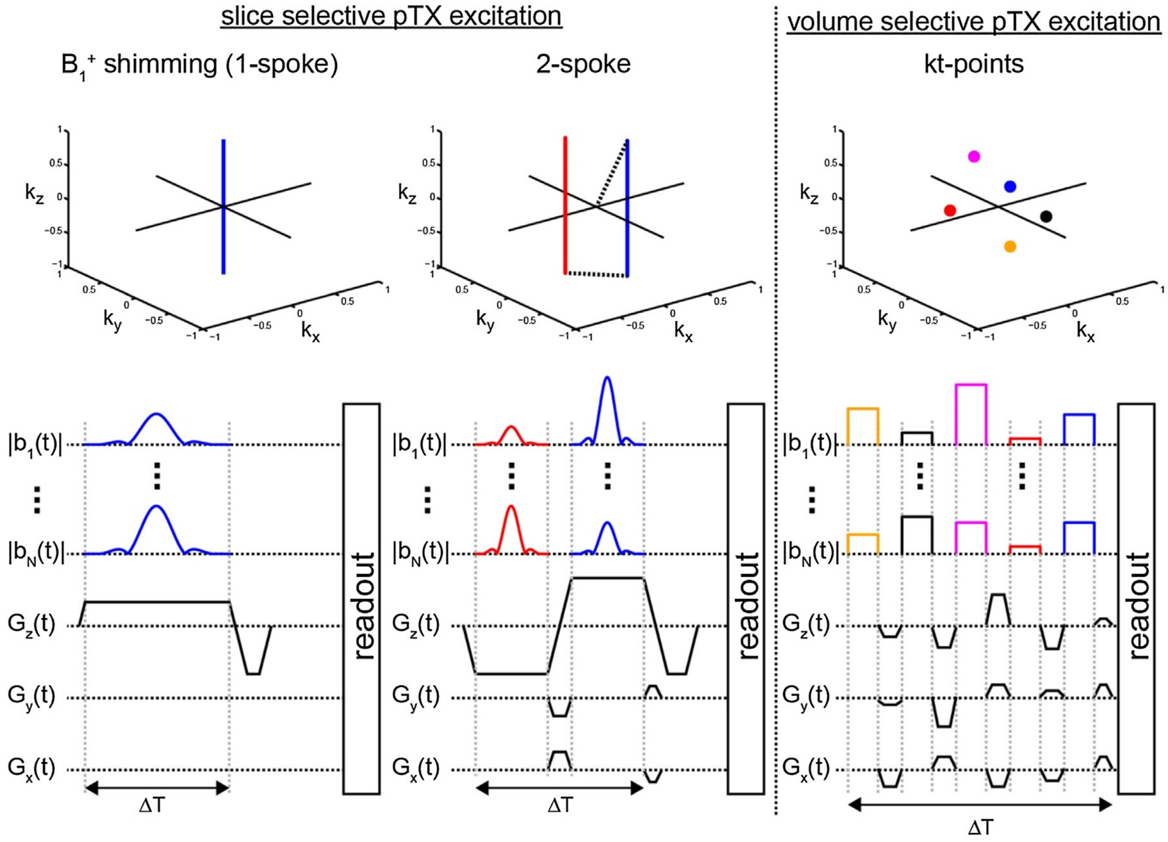

Fig. 2. Sequence scheme and k-space excitation trajectory for slice-selective (spokes) and volume-selective (kt-points) dynamic pTx. Individual RF pulses are color-coded in the scheme and k-space trajectory. The duration ΔT typically increases with rising number of spokes or kt-points.

be time-consuming. Therefore, a recent study has investigated the use of "universal" kt-pulses [91] that were designed based on the B_1^+ maps of six subjects; subsequently, such pulses were successfully applied in six different subjects not used for the pulse optimization without acquiring additional calibration data. This approach has high potential for clinical UHF imaging, as it substantially reduces the time for calibration and does not require online RF pulse design.

A third major class of dynamic pTx pulses are 2D or 3D spatially-selective pTx RF pulses that are used, for example, for localized excitation. Similar to slice-selective pulses (1D), the 2D/3D selective pulses restrict the field of excitation (FOX), but in two or three dimensions. Often the FOX is given by a bar, a cylinder, or a cube, but also a complex-shaped 3D FOX can be realized that specifically excites a given structure. In principle, such techniques are also feasible using a single-channel transmit system [79]. However, such complex excitation patterns require fairly long gradient trajectories, and parallel transmission with multiple channels can be used to undersample the excitation k-space while maintaining excitation fidelity. This technique, termed "transmit SENSE" [75], was actually one of the first dynamic pTx applications.

The RF pulse shapes and gradient switching of transmit SENSE pulses differ from kt-points and spokes pulses in that no common RF waveform b(t) can be defined, even for subsections of the RF pulse. Also, the optimization problem is often more complex. For spokes RF pulses and kt-points pulses, each spoke and kt-point is typically treated as an instantaneous, zero-duration pulse during the optimization; thus, N spokes (N kt-points) are represented in time by only N sample points, with dwell times between the sample points of several hundreds of microseconds. This is different from transmit SENSE where the entire RF and gradient waveforms are sampled on a fine raster with dwell times of a few microseconds. As a result, the number of sample points can be two or three orders of magnitude larger than for spokes. Gradient trajectories for such applications typically include 2D and 3D spirals of various forms, 3D shells, or other complex trajectories [92].

Localized excitations are beneficial for MR imaging purposes, as they allow for restricting the field of view to the FOX and thus reducing the number of k-space lines. The gain in acquisition time can then be invested into increasing the resolution, if SNR permits. It should be noted that all local excitations will excite magnetization outside the intended FOX to some degree. From an application point of view it is often more relevant to minimize the residual signal outside the intended FOX than optimize the homogeneity within the FOX, because any residual signal will alias into the field of view. Furthermore, for many imaging applications the excitation of 2D geometries such as bars or cylinders is often sufficient, as the third dimension can coincide with the readout direction. For spectroscopy, however, 3D-shaped excitations are of high interest, as they allow for quantification of metabolites within a given region only.

All parallel transmission techniques require 2D or 3D transmit sensitivity maps of the individual channels that can be obtained with various flip angle mapping or B_1^+ mapping techniques. Prominent methods are the magnitude-based actual flip angle (AFI) technique [93], originally a 3D technique that has been adapted to 2D mapping [94]; the DREAM method [95], a fast, magnitude-based 2D technique; or the 2D phase-based Bloch-Siegert shift method [96]. Spokes or other slice-selective pTx methods require at least a 2D B_1^+ map, while 3D or localized pTx methods require 3D B_1^+ maps. In addition, maps of the local static magnetic field B_0 are typically acquired and included in the RF pulse design.

So far, only challenges that result from the magnetic component of the transmit RF field have been regarded. In addition, the electric field as well as the associated specific absorption rates, defined as $\mathrm{SAR}(\vec{r}) = \frac{\sigma}{2\rho}\left|\vec{E}(\vec{r})\right|^2$ (σ: conductivity; ρ the mass density of the tissue) and used as a measure for the RF power deposited in the tissue, cause substantial problems at UHF as already mentioned in Section 2. Not only does the required RF power increase with field strength, but also SAR becomes increasingly spatially heterogeneous, forming local areas of high SAR values ("hot spots") at UHF. As the absorbed power is transformed into heat, the transmitted RF increases the general body temperature and too high local SAR values can potentially cause local tissue damage. To ensure patient safety, the maximum temperature increase as well as maximum local and global SAR values are limited according to international guidelines [33].

In practice, the SAR limits often require workarounds such as stretching the RF pulses in time, lowering the flip angle, or lengthening the repetition time. However, the global SAR, the peak 10 g-averaged local SAR, the transmit power as well as the temperature increase can be constrained during RF pulse design [97]. Although research is being done to derive SAR and temperature from MRI measurements, at present the electric field components, the SAR, and the temperature are obtained from numerical electromagnetic simulations using a virtual coil and a virtual human body model. SAR and temperature are then provided in matrices or compressed matrices [98] that can be included into the RF pulse design. Thus, such pulse design methods combine measured sensitivity maps with simulated SAR or temperature constraints; therefore, it is essential that the simulation matches the real experiment to reasonable accuracy [19].

It should be noted that the preceding paragraphs cover only a portion of current pTx techniques. Further techniques as well as various optimization algorithms exist, the coverage of which is beyond the scope of this article. However, the reader is referred to a more comprehensive review paper on parallel transmission by Padormo et al. [81].

3.2. Applications

Although the concept of pTx has existed for about 15 years, the transition of pTx into in-vivo studies or ultimately into clinical routine is still fairly slow. Some state-of-the-art 3 T systems now include a pTx system with 2 transmit channels, typically used for body applications, which promotes the application of pTx at high field [99]. At UHF, which will be the focus in the following, pTx is still mostly a research tool, although UHF systems are often equipped with 8 Tx channels and a few even with 16 or 32 Tx channels. The majority of applications at UHF have so far targeted the human head, although parallel transmission techniques are no less essential in body applications, undoubtedly even more so due to the dimensions of the body compared to the head. In the head, however, respiratory or cardiac motion can be disregarded when investigating novel pTx techniques, which otherwise would add another level of complexity to the MR sequence, the MR acquisition, and potentially to the RF pulse design.

Despite progress in single-Tx-channel UHF RF head coil design and transmit performance that has enabled the acquisition of high-quality 7 T head images without substantial B_1^+ dropouts, the use of pTx for UHF brain imaging has been shown to be highly beneficial for a large range of applications. Static pTx B_1^+ shimming has been applied in the head mostly in order to locally or globally increase the B_1^+ amplitude, or to increase the B_1^+ homogeneity across a region [100], a single slice, for multiple slices [101], across a slab [102,103], or across the brain volume [101]. Localized shimming, which typically aims at increasing the B_1^+ efficiency, has been applied in the brain particularly for MR spectroscopy at 7 T [100,104–106] and at 9.4 T [107], but also for other applications such as functional MRI [108]. Whole-brain efficiency shimming has also been demonstrated [109], but in the case of phase-only shimming, an efficient shim may result in local B_1^+ dropouts. Homogeneous B_1^+ shimming in the brain has been achieved; however, it has also been demonstrated that B_1^+ shimming applied to larger ROIs substantially reduces the transmit efficiency or increases SAR values, which in turn increases RF power requirements and imposes restrictions on pulse sequence parameter choices [101,102]. Furthermore, it has been observed at 9.4 T, where spatial variations of B_1^+ magnitudes and phases are stronger compared to 7 T, that solutions to cost functions enforcing homogeneity sometimes cannot be obtained without local B_1^+ voids [110] and therefore other cost functions such as the inverse of the minimum B_1^+ amplitude need to be chosen. Further successful applications of B_1^+ shimming at 9.4 T have been demonstrated in [111–113].

B_1^+ shimming has further been applied to a large range of targets in the human body, for which in most cases B_1^+ shimming is necessary in order to achieve sufficient transmit B_1^+ amplitudes and/or acceptable image quality. 7 T prostate MRI and MRS [114–119] were among the first applications in the body. For MRS, B_1^+ shimming is required [120], and in all cases shim settings enforcing high transmit efficiency were applied, which is facilitated by the limited size of the prostate. B_1^+ shimming has further been applied to cardiac MRI [121] as well as to aortic flow imaging [122,123] using different shimming approaches. A practical challenge in cardiac MRI is given by cardiac and respiratory motion, the effects of which increase with field strength to a certain extent. The detection of and synchronization with cardiac motion is difficult at 7 T due to the magnetohydrodynamic effect [39] that affects heart beat detection by an ECG (cf. Section 2.1), and respiratory motion detection is difficult due to heterogeneous B_1^+ magnitudes that potentially affect respiration navigators. Such issues have been addressed e.g. by using an acoustic cardiac triggering system [124] or by applying dynamic RF shimming with dedicated shims for the navigators [123]. Other approaches have investigated the possibility to detect such motions by analyzing modulations of the RF scattering matrix while using dedicated RF shim sets [125]. It has further been demonstrated that respiratory motion also affects the B_1^+ field and therefore may impact B_1^+ shimming results [126]. Other targets of body MR with B_1^+ shimming are the liver and kidneys [78,127–133]. Both are organs that are intrinsically more difficult to shim than the prostate or heart due to their size and geometry. B_1^+ shimming has further been applied at 7 T to unilateral [134,135] and bilateral [136,137] hip imaging, to imaging of the shoulder [138], to spine imaging [139] and to breast imaging [140], among others.

Some applications require the use of dynamic shimming techniques to switch the shim setting within the sequence. Dynamic shimming has been applied, for example, in MRS [100,104] to toggle between shims for excitation and saturation, or in the body to toggle between inversion and excitation [78].

The TIAMO technique [77] has been widely applied, which merges typically two images of the same target obtained with different, complementary shim sets. The reconstructed images yield sufficient signal homogeneity at 7 T even in large-sized abdominal targets [128,129,141], in the extremities [142,143], or in the brain at 9.4 T [144]. In another study TIAMO enabled the identification of lymph nodes over a large pelvic region [145]. An example of applying TIAMO to a large region is highlighted in Fig. 3, for which a 32-Tx-channel prototype body coil was used.

Although dynamic pTx using slice-selective spokes RF pulses achieves improved flip angle homogeneity within the slice compared to B_1^+-shimmed slice-selective excitations, such RF pulses

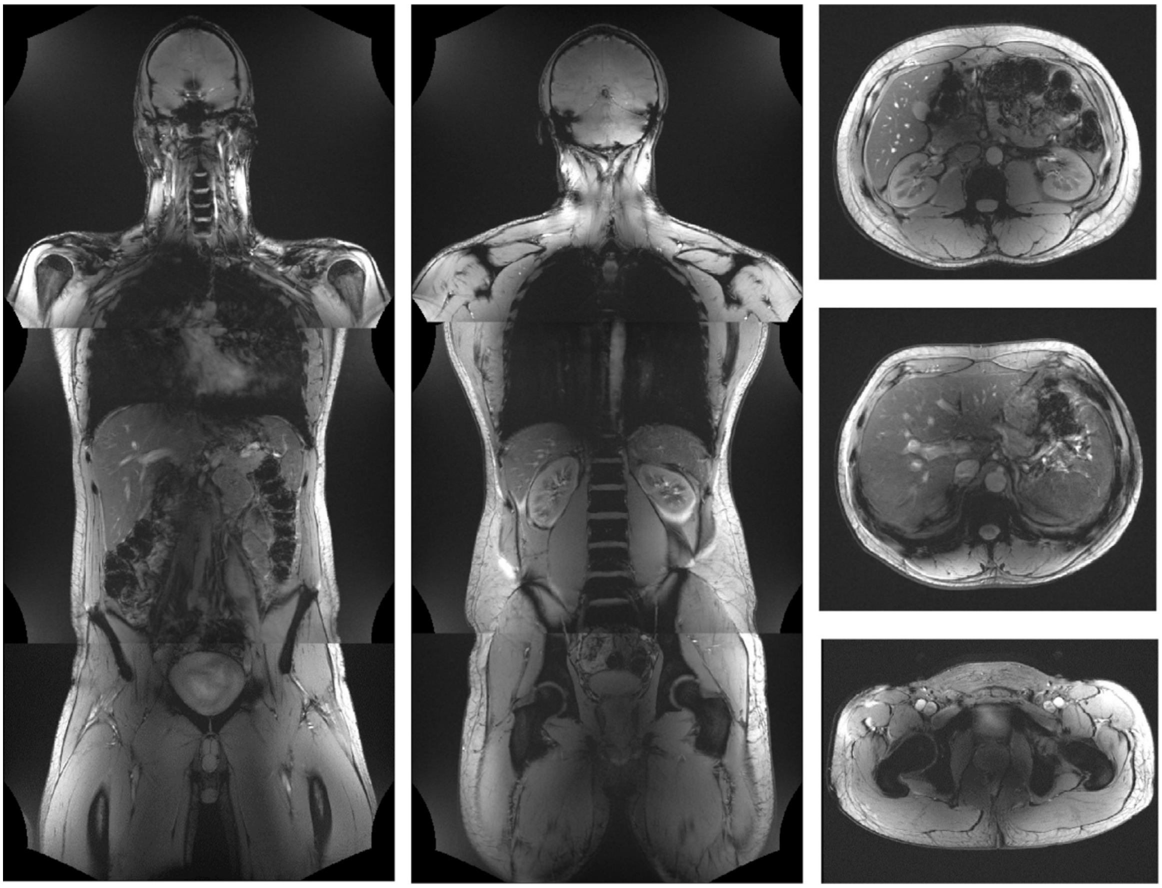

Fig. 3. Multi-station 2D gradient-echo acquisition of a male subject (92 kg, 185 cm) at 7 T using the TIAMO technique. A prototype 32-channel transmit system feeding a 32-channel body coil [146] was used during acquisition. Other parameters: field of view 50 cm, resolution 1.1 × 1.1 × 5 mm^3, TR/TE 50 ms/6.1 ms. Courtesy of Erwin L. Hahn Institute, Essen, Germany.

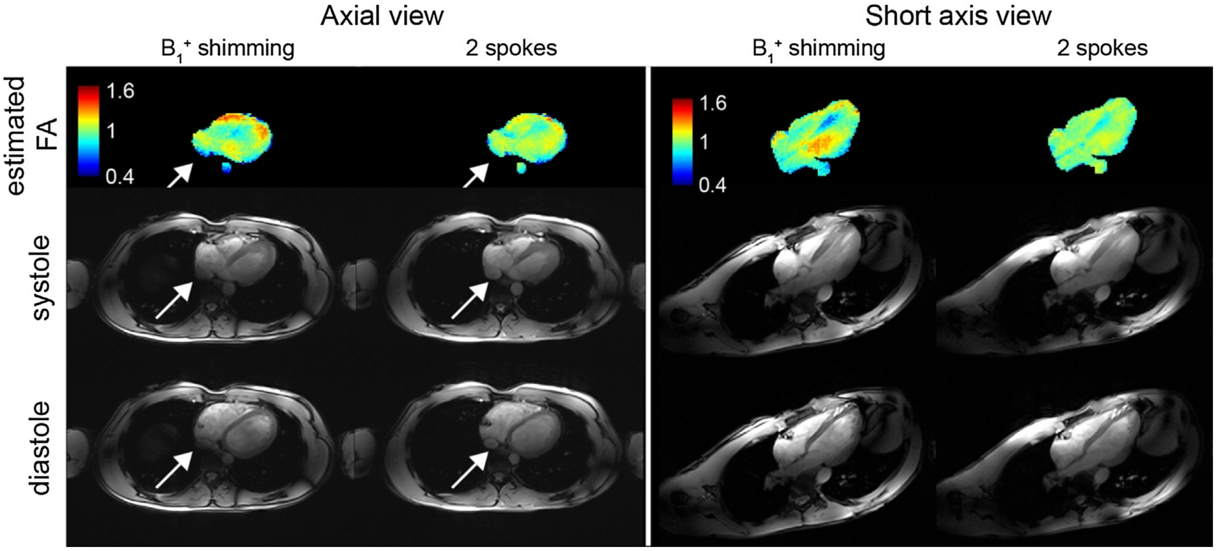

Fig. 4. Cardiac gradient-echo cine imaging using a 16-TX-channel pTx spokes excitation in axial and short-axis views. Particularly the posterior regions of the heart and the great vessels benefit from 2-spoke excitations as highlighted by the white arrows. Parameters: resolution 2.3 × 2.3 × 5 mm^3; TE/TR = 2.9 ms/5.6 ms (B_1^+ shimming), 3.2 ms/6.0 ms (spokes). Modified from [151].

so far have been applied infrequently at UHF compared to B_1^+ shimming. However, their potential has been investigated and demonstrated in vivo at 7 T in various forms and even at 9.4 T. Most applications target the human brain [83,103,147–150], but also body applications have been investigated, such as liver [133] and cardiac MRI [151] as illustrated in Fig. 4. Furthermore, nonselective

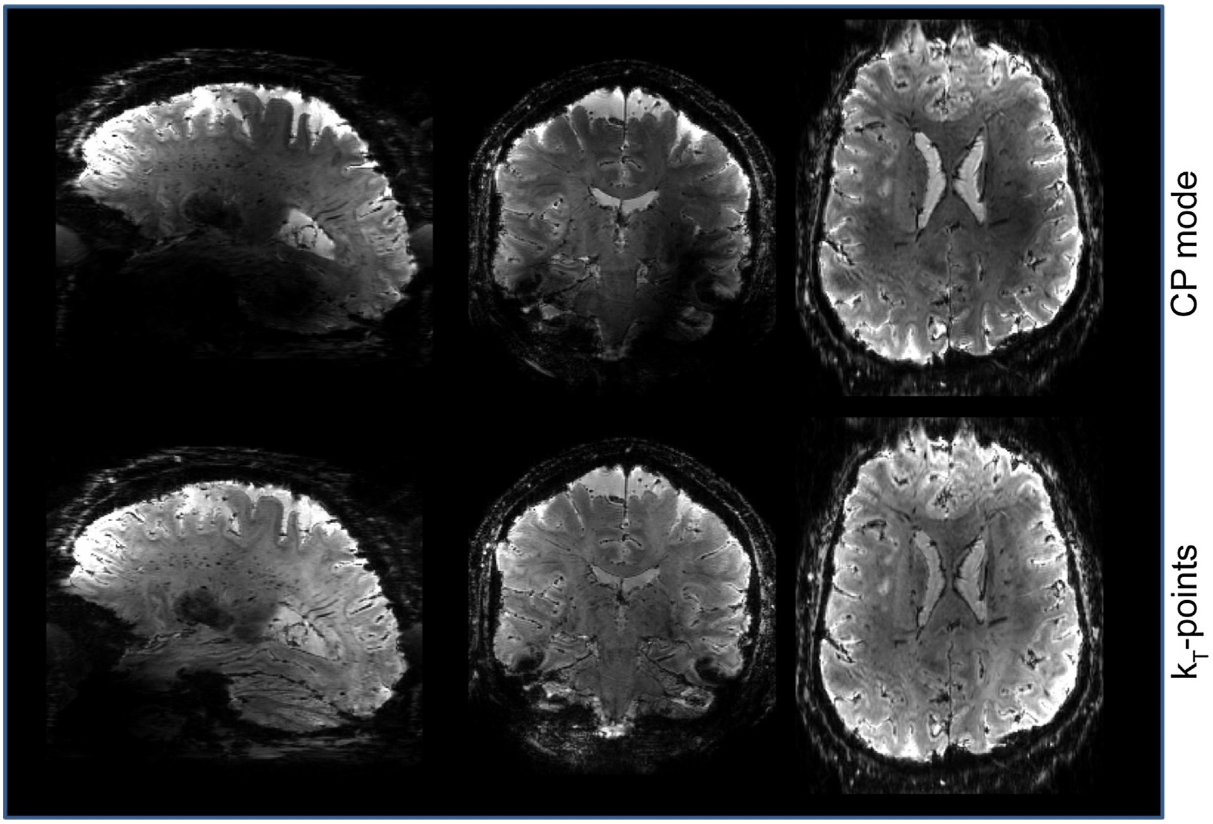

Fig. 5. Echo-planar images obtained at 9.4 T using a 16-Tx-channel pTx system and excitation with the circularly polarized (CP) mode (top row) and kT-points pTx (bottom row). Parameters: 0.75 mm isotropic resolution, in-plane acceleration GRAPPA 3, partial Fourier 6/8, head coil with 16 Tx channels and 31 Rx channels. Courtesy of Desmond Tse and Benedikt Poser, Maastricht University, The Netherlands.

excitations using kt-points [90,152] or spiral nonselective (SPINS) pulses [153] targeting the human brain have been investigated, also at 9.4 T [81,154]. An example is shown in Fig. 5 for homogeneous kt-points excitations at 9.4 T applied to echo-planar imaging.

Particularly in fast T1-weighted and T2-weighted imaging sequences, such as turbo spin echo (TSE), the interplay between different pulses (excitation, refocusing, inversion) becomes important, as this affects the final signal. Different strategies have been realized to optimize the signal for such sequences [155–158], for example by using the spatially resolved extended phase graph technique [159].

2D or 3D spatially-selective pTx RF pulses are of high interest for UHF applications, as they allow for a reduction in the acquisition time while obtaining high spatial resolution, and reductions in SNR are counteracted by the ultra-high field. Such RF pulses are the subject of current research in imaging [92,160,161] and spectroscopy [162,163].

The combination of efficient algorithms and the computational speed of current CPUs nowadays enables online calculation of patient-specific pTx RF pulses within seconds, even for advanced sequences. This capability allows for optimal signal and contrast for each individual patient, while reducing SAR, but it also requires the calibration and calculation framework to be fully embedded into the scanner's system architecture for optimal workflow and minimal calibration time. Therefore, from a clinical perspective, the use of universal pulses [91,164] is interesting, as patient-specific calibration scans are no longer needed, and thus scan and examination time are saved. An example of kt-points universal pulses in comparison to a CP mode excitation is shown in Fig. 6 for T2-weighted imaging of the human brain at 7 T [165]. Another recent approach at UHF, termed "plug-and-play MRF" [166], is based on the MR fingerprinting technique [167] that is used to simultaneously quantify multiple tissue-specific parameters such as MR relaxation times. In this case, the method does not require homogeneous B_1^+ or flip angles distributions. Instead, different heterogeneous B_1^+ distributions are generated and applied, which are then quantified alongside the tissue parameters of interest.

The preceding paragraphs demonstrate that a large range of techniques exists to address and overcome the challenges in UHF imaging and spectroscopy that are associated with the short RF wavelength. Independent of the technique used and the type of UHF application, some sort of manipulation of the spatial distribution of the B_1^+ field is required at UHF, especially for body imaging as well as for upcoming systems with field strengths beyond 10 T.

4. High-resolution imaging and motion correction

4.1. Technical aspects

For gradient-based image encoding, MRI raw data are acquired sequentially. Therefore, despite dramatic advances in RF-coil-based encoding (parallel imaging) [168], MRI remains a relatively slow modality, in particular for acquisitions with high spatial resolution. Imaging with higher spatial resolution is one of the driving forces for higher magnetic field MRI in the attempt to close the gap between in-vivo imaging and invasive microscopy. Even with increased SNR at UHF, imaging times for very high resolution are long, and thus motion sensitivity is high for two reasons: (i) motion is more likely to occur during long acquisitions and (ii) measurements become more motion sensitive for smaller imaging voxels.

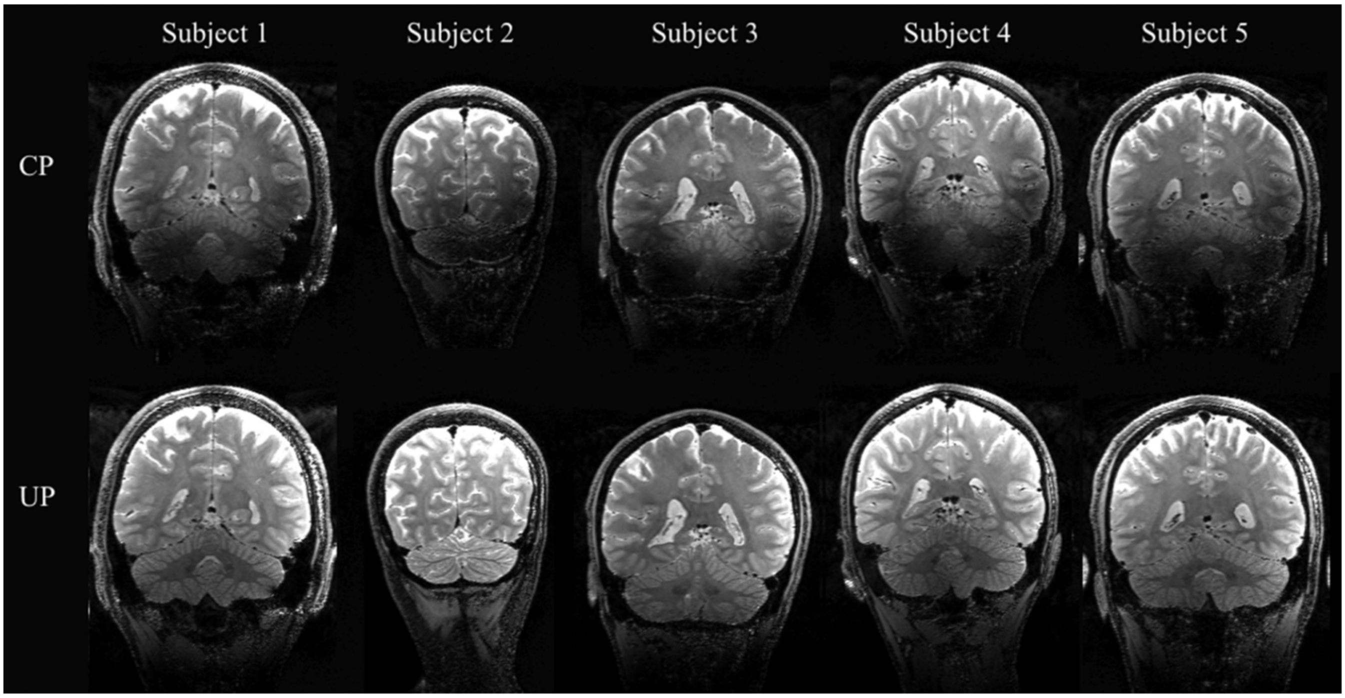

Fig. 6. Circularly polarized (top row) and universal kt-points (bottom row) excitation and refocusing pulses applied to 3D T2-weighted imaging of the human brain at 7 T. Reproduced from [165].

Even sub-voxel motion can lead to imaging artifacts due to inconsistency in the acquired k-space data.

Motion has been an archenemy of MRI since its invention, and attempts to avoid or correct for motion are as old as the technique itself. In clinical MRI, the consequences of motion-related imaging artifacts are dramatic, with frequent need for repeat examinations and potential for missed pathologies [169]. Many methods have been proposed to detect and correct patient motion and related imaging artifacts. They can be categorized by the motion detection modality and the correction approach. Detection can be based on MR itself using either additional navigator data (1D or 2D projections) [170–173], motion tracking images (either 2D images or 3D volumes) [174,175], or redundant k-space trajectories that allow self-navigation [176,177]. Alternatively, external motion tracking systems employing additional hardware can be used to detect motion independent of the MRI acquisition, e.g. through optical methods [178–182] or by attaching small RF coils to the object [183,184]. Such motion information can be used to discard and repeat acquisition steps, correct the MR raw data retrospectively during the reconstruction, or modify the MR sequence to prospectively adapt the imaging volume to the motion, thus requiring no further modification of the reconstruction.

A number of reviews have recently described these possibilities in more detail [185–188]. Of these many methods, only few have become commercially available and are used frequently in clinical diagnosis. Mainly self-navigated acquisitions (PROPELLER [periodically rotated overlapping parallel lines with enhanced reconstruction], BLADE), 1D navigator methods, and, more recently, volume navigators are applied clinically.

The above-mentioned methods are successful in removing or avoiding artifacts due to motion of non-compliant patients. For very high spatial resolution imaging at high field strength, however, involuntary motion even in very cooperative subjects can degrade the effective resolution even though major motion artifacts may not be obvious. It has been shown that the requirements to hold still and thus the accuracy of motion correction approaches has to be approximately 5-times smaller than the voxel dimensions [189]. In high-resolution imaging with a resolution of a few 100 μm, motion related to breathing or the cardiac cycle will thus become relevant and is not avoidable in vivo. In brain imaging, the main target of current UHF studies, breathing causes motion of up to 1 mm and the cardiac pulse wave impulse leads to more than 100 μm of head displacement [179]. Thus, even in perfectly cooperative subjects physiological motion will degrade very high resolution acquisitions. This has been termed the biological resolution limit that has to be overcome to fully exploit the imaging capabilities of high-field MRI and approach the nominal acquisition resolution.

Many of the above-mentioned motion correction approaches have not been applied to very high resolution imaging at 7 T and above, most likely due to insufficient accuracy and precision in motion detection or a lack of UHF availability. For very high resolution brain imaging at 7 T and above, optical detection methods and fat-based volume navigators have been successfully demonstrated. Gallichan et al. have developed so called 3D FatNavs and successfully applied them to high-resolution imaging at 7 T [190]. This extension of the volume navigator approach exploits the fat signal for navigator acquisition only. The acquisition of the sparse fat signal can be highly accelerated, yet still needs about 1 s acquisition time per update, thus limiting the temporal resolution of positional information and potentially increasing the scan time. The fat-only excitation has very little influence on the water magnetization, reducing the interaction between navigator and imaging module. The motion information is used during reconstruction to correct for motion-induced changes in the raw data based on a rigid body model (translation and rotation). This method does not require any additional hardware and is mainly targeted to correct for slow positional drifts.

A different approach is taken by Stucht et al. [26], who applied an optical pose tracking system to determine motion with a very high update rate (up to 86 Hz) and high precision (down to 10 μm). The Moiré phase tracking principle of the system can achieve this tracking performance with a single camera and a single structured target, which does, however, require additional hardware and fixation of a marker to the anatomy of interest. For brain imaging in a confined head coil, the authors mounted the target to an individually produced mouthpiece to ensure "rigid" connection to the brain. While this approach requires more effort and is less comfortable for the subject compared to FatNavs, the tracking data are of very high quality, and tracking does not interfere with any measurement sequence. The accuracy of the system is mainly limited by the rigidity of the marker mounting. The pose data are available during the scan and used to prospectively adjust the imaging volume to follow the subject motion. Therefore, the raw data are consistent despite subject motion, and no modification of the reconstruction software is required.

An alternative optical system for motion tracking at 7 T has been presented by Schulz et al. [181]. This system employed three cameras and three optical markers to detect rigid body motion. The development has been discontinued, however.

Due to image hardware imperfections of MRI systems, the motion of rigid objects leads not just to a shift and rotation of the images; geometric distortions due to gradient non-linearity, magnetic field variations, and RF coil sensitivity profiles all change relative to the object upon motion. Such effects violate the rigid motion assumption and cannot be corrected by prospective field of view adjustment. Further correction of residual effects has been proposed by Yarach et al. using an iterative solution of a forward signal model that includes these known motion-related image variations [191,192].

4.2. Applications

At lower field strength, many publications have presented motion correction methods and compared acquisitions with and without data correction in the presence of deliberate (large) motion. These tests demonstrate the methods' potential for uncooperative subjects (although with highly artificial motion patterns). In very high resolution brain imaging of cooperative subjects at high field, involuntary motion may result in minor image quality degradation that is largely unnoticed in the absence of an artifact-free reference.

For high-resolution imaging, 3D FatNavs with an acquisition time of a little over 1 s and imaging have been interleaved to result in positional data with an update rate between 2.7 and 7.6 s [193]. In MP2RAGE and TSE, the navigator module exploits the "unused" recovery time, while in 3D GRE the acquisition is prolonged by about 16%. The authors present high-resolution 3D data of a single subject with 350–380 μm resolution with acquisition times of 42–124 min (one or two sessions per contrast). The subject did not move intentionally and the RMS displacement was below 1 mm for all scans. Although the uncorrected images are already of high quality, the correction improved the sharpness of many small structures. This study proves that even in highly cooperative subjects with motion well below the "tolerable limit" (e.g. as used in fMRI studies), motion correction can visually improve the image quality.

Stucht et al. [26] have presented very high resolution human brain data using prospective optical motion correction. In the comparison of 3D MPRAGE with 440-μm resolution and 2D GRE with 250-μm in-plane resolution and 2-mm slice thickness, the results confirm the findings of Federau et al. that motion correction can increase the sharpness of structures and SNR even in highly cooperative subjects for high-resolution acquisitions. They also present some of the highest resolution in-vivo data acquired to date: 2D GRE with 120-μm in-plane resolution and 600-μm slice thickness and 3D time-of-flight angiography with 200-μm isotropic resolution. Due to the prospective nature of the correction, an uncorrected version of the acquisitions is not readily available and requires a second acquisition or creation of a virtual uncorrected image by means of undoing the correction retrospectively [194].

Mattern et al. applied prospective optical motion correction to high-resolution time-of-flight angiography and systematically determined the benefit over uncorrected scans [195] (Fig. 7). With 250-μm isotropic resolution, the correction showed clear improvement in 8 out of 11 subjects that were instructed to hold as still as possible. The corrected images of the remaining 3 subjects were equivalent to the uncorrected images and did not show any degradation that might potentially be introduced due to instability in the correction. In addition, this work presents the highest resolution time-of-flight angiography to date with an isotropic resolution of 150 μm, albeit with an excessively long scan time of 2 h 14 m. The further improved resolution increased the visibility of very small vessels, and with a voxel volume of only 3 nl represents perhaps the highest resolution in-vivo human brain angiogram from any imaging modality.

Perhaps the most extreme application of prospective motion correction at 7 T has been presented by Lüsebrink et al. [27], who acquired full brain MPRAGE data with an isotropic resolution of

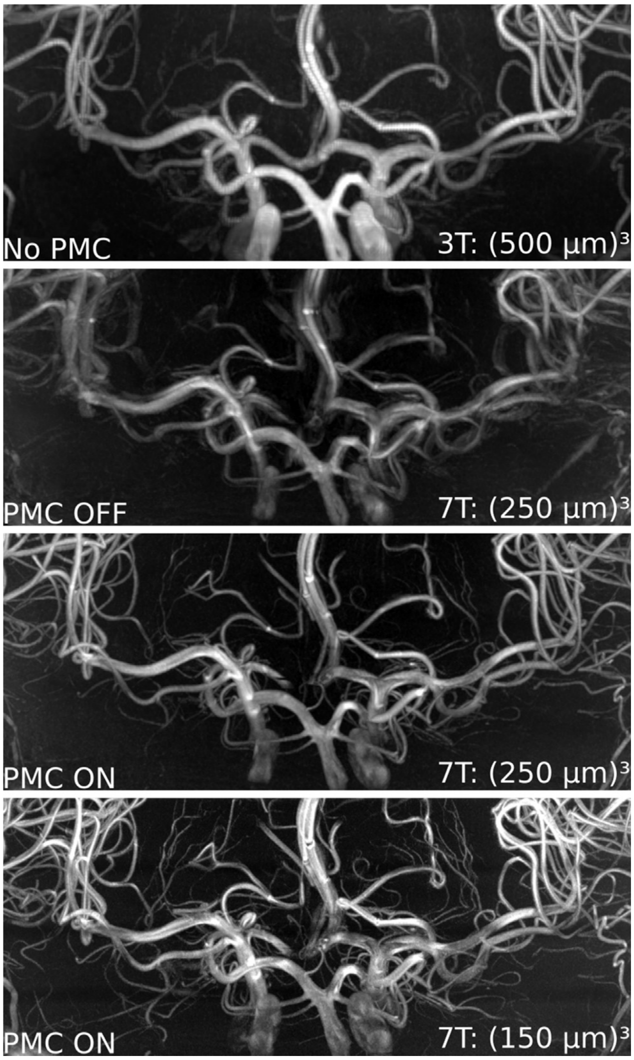

Fig. 7. Time-of-flight angiogram at 3 T (500 μm) and 7 T (250 μm) without prospective motion correction (PMC) (top) and co-registered 250-μm and 150-μm motion-corrected examples of the same subject. The higher sensitivity at high field is clearly visible, and the much clearer depiction with motion correction enables the highest resolution angiogram despite long scan times (48 min for 250 μm and 134 min for 150 μm).

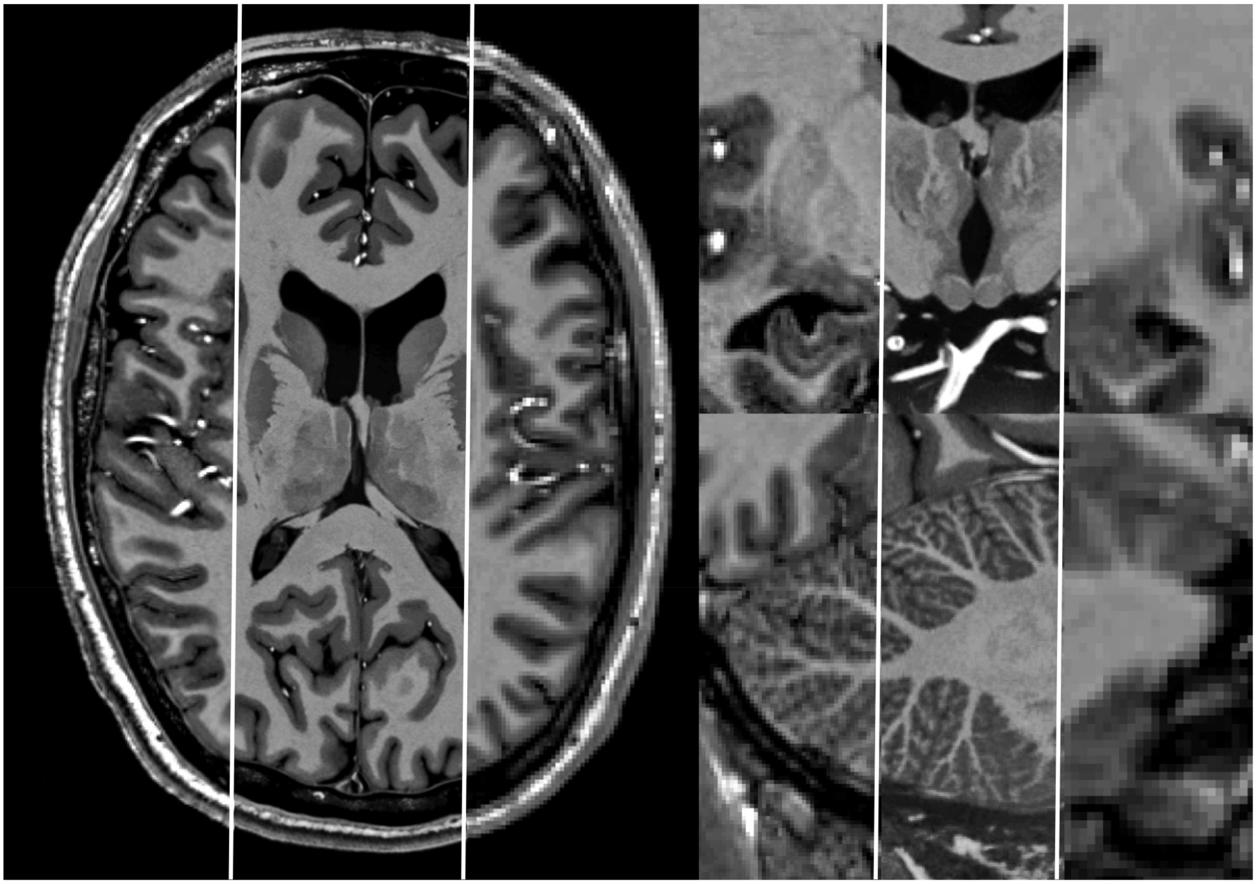

Fig. 8. The highest resolution in-vivo full brain dataset at 250-μm resolution, enabled by motion-corrected acquisition over multiple sessions. In each of the sub-images, the 250-μm data are merged with 500-μm and 1-mm-resolution acquisitions of the identical volume (left 500 μm, center 250 μm, right 1 mm). The 250-μm data are from Lüsebrink 2017 and have been further processed using the SPM Computational Anatomy Toolbox (CAT) for noise filtering.

250 μm and made the raw and image data fully available. This acquisition is limited by low SNR and thus multiple acquisitions were necessary to achieve sufficient SNR. Optical tracking and a marker reproducibly fixed to the teeth via a mouthpiece allowed for data acquisition over multiple sessions in a total imaging time of about 7 h. Similar to the previously mentioned work, this paper also shows the benefit of motion correction at a lower resolution of 450 μm in a subject without intentional motion. At the highest resolution of a full brain in-vivo scan to date, the data show exquisite detail of many structures such as the fine line of the dura mater, the intricate structure of the hippocampus and striate bodies, or the fine detail of the cerebellar folia. Fig. 8 is merged from data with different resolution. In each of the three sub-images, the right part shows 1 mm, the left part 0.5 mm, and the center part 0.25 mm resolution.

5. Susceptibility-weighted imaging, phase contrast, and quantitative susceptibility mapping

5.1. Technical aspects and contrast mechanisms

Both susceptibility-weighted imaging (SWI) [196] and quantitative susceptibility mapping (QSM) [197–199] use phase information. In SWI, magnitude images and information derived from phase images are combined, and the phase information is used to enhance magnitude contrast by multiplication with a mask derived from the filtered phase images. To generate susceptibility maps, on the other hand, filtered MR phase is deconvolved with a dipole kernel to obtain local information on tissue susceptibility from non-local field perturbations observed in phase images. In QSM, the magnitude data are only needed as additional information to generate a brain mask or for regularization purposes. Moreover, MR phase itself has been shown to provide additional and somewhat complementary information to the magnitude of the MR signal [200,201]. Therefore, the benefits and challenges of ultra-high field strengths for imaging MR signal phase are most relevant in this section.

5.1.1. Contrast mechanisms, microstructure, and orientation dependence

As phase changes that originate from susceptibility changes are directly proportional to the applied field strength and echo time, $\Delta\phi = -\gamma\chi B_0 TE$, phase imaging at UHF benefits from larger phase effects (Fig. 9) and the achievable contrast-to-noise ratio increases with field strength [201]. Moreover, spin dephasing at UHF is faster compared to lower field [202], leading to large signal dropouts in SWI in the vicinity of structures with largely different susceptibilities compared to their surrounding tissues, such as deoxygenated blood in veins, hemosiderin and methemoglobin in hemorrhage, or iron-rich brain nuclei. Such structures and tissues are shown as hypointense in GRE magnitude data as well as in SWI regardless of whether they are diamagnetic or paramagnetic, which is in contrast to phase imaging and QSM, where diamagnetic and paramagnetic substances can be differentiated and quantified. Large signal drop-outs can be more problematic at UHF compared to lower field strengths, and can be a source of artifacts as in the case of air-tissue interfaces, for example in the region of the paranasal sinuses. Moreover, it should also be considered that non-local phase effects

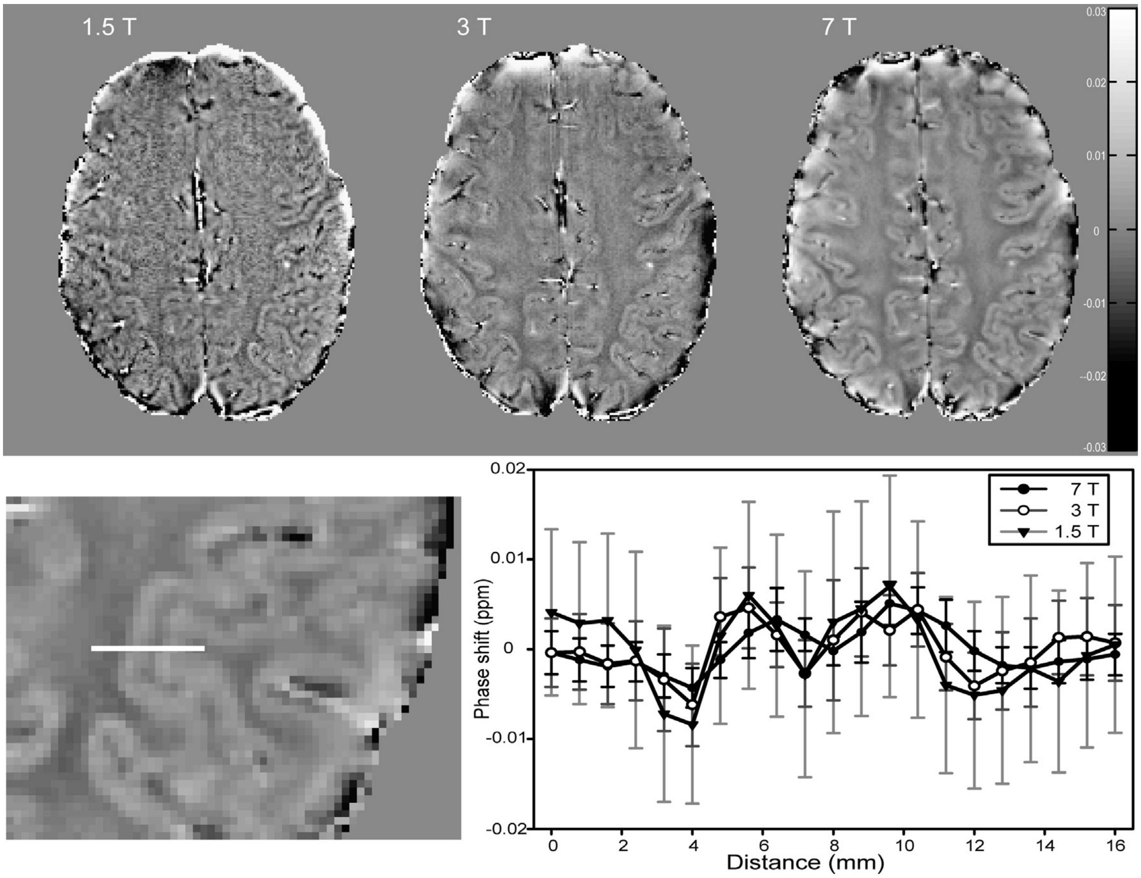

Fig. 9. Phase images at 1.5 T, 3 T, and 7 T normalized by field strength and echo time with an isotropic resolution of 0.8 mm. GM/WM contrast is best at 7 T, whereas the noise is highest at 1.5 T. A cortical profile in the parietal lobe shows similar behavior for all field strength, and phase offsets between gray and white matter are visible. Reproduced from [211].

in SWI and phase images depend on the geometry of the susceptibility source; the information mapped in QSM is more tissue specific and provides information on the actual tissue susceptibility rather than on the magnetic field perturbation it causes.

In the brain, iron and myelin are fundamental to the susceptibility contrast mechanisms. Phase contrast in white matter (WM) has been attributed to myelinated fiber bundles, whereas in gray matter (GM) the layer structure of the cortex [201] and iron content are presumed to influence MR phase [203]. Only a very weak correlation was shown between iron concentration in WM and susceptibility, in contrast to deep GM structures where this correlation was strong [204]. Exploiting the high CNR and the high spatial resolution achievable when using UHF MRI, additional underlying principles of phase contrast and its consequences for SWI and QSM have been explored. These ongoing investigations include the effects of microstructure [205], anisotropic susceptibility [206–210], and chemical exchange [211]. Zhong et al. [211] reported a phase difference between GM and WM of 0.01 ppm (Fig. 9), which was attributed to chemical exchange between water and macromolecule protons. Comparing measurements of ex-vivo optic nerve at different orientations with respect to B_0 and simulations, WM frequency variations were found that could not be explained by bulk susceptibility effects or anisotropic susceptibility, but were postulated to be a microstructure-related effect [205]. The echo-time-dependent susceptibility contrast of some GM structures studied using a three-compartment model suggests that the echo-time-dependent susceptibility evolution could provide information on cytoarchitecture [212]. Marques et al. [213] showed maps of cortical layers using quantitative susceptibility mapping, R_2^*, and R_1, and could visualize different Brodmann areas that are related to the cytoarchitectural organization of the cortex.

5.1.2. Data acquisition

The standard acquisition technique for both SWI and QSM is a Cartesian 3D spoiled single- or multi-echo gradient-echo (GRE) sequence, which allows for spatially highly resolved imaging, especially at UHF due to higher SNR [12,17]. QSM particularly benefits from UHF MRI, since noise in the MR phase is amplified when calculating susceptibility maps due to the ill-posedness of the dipole inversion [214]. At 7 T, in-plane resolution of near $0.2 \times 0.2\ \text{mm}^2$ has been achieved in in-vivo human brain measurements of MR signal phase [201,215]. For higher resolution, measurement time might be a limiting factor as well as motion if it is not compensated (cf. Section 4). GRE acquisitions for the generation of susceptibility maps preferably use isotropic resolution, whereas for SWI non-isotropic resolution is beneficial, especially to obtain good vessel contrast [216]. The use of an echo time between $T_2^*/2$ and T_2^* of the structure of interest is recommended for SWI and QSM [197]. Therefore, due to larger phase shifts and faster dephasing (shorter T_2^* relaxation times compared to lower field strengths), UHF allows for the use of shorter echo times and in turn shorter repetition times, resulting in shorter scan times. This saved time can be used to acquire images with higher spatial resolution.

Recently, 3D Wave-CAIPI [217] (controlled aliasing in parallel imaging) or non-Cartesian planes-on-a-paddlewheel EPI [218] have been proposed for highly accelerated QSM at UHF. Moreover, standard MR phase signal from GRE acquisitions with parameters optimized for SWI or QSM are relatively insensitive to B_1

inhomogeneities [200], and SAR depositions are low due to the small flip angles (5–20°) that are generally used, rendering phase imaging, SWI, and QSM ideally suited to UHF MRI.

5.1.3. Data processing

At UHF, phase processing is complicated by the fact that no volume coils are available to which coil sensitivities can be referenced and that receiver phase offset variation in the brain exceeds 2π due to the shorter RF wavelength, resulting in more severely wrapped phase compared to lower field strengths. Coil combination techniques for single-echo GRE data often require a reference scan at lower resolution. An overview of coil combination and phase unwrapping algorithms is given in [219]. Algorithms for background field removal [220] and dipole field inversion for QSM [221–225] can be applied to data acquired at both clinical and UHF strengths without modifications.

5.2. Applications

5.2.1. Brain anatomy

5.2.1.1. Normal brain. High spatial resolution and high contrast in SWI, MR phase, and QSM provided by UHF MRI enable the delineation of various brain structures that were previously difficult to define using conventional MRI. At 7 T, the subthalamic nucleus can clearly be differentiated from the substantia nigra in SWI [226] and QSM [227], substructures of the red nucleus are visible, and the globus pallidus internus and the globus pallidus externus [226] as well as the cerebellar nuclei and their substructures [228] can be clearly defined using SWI. QSM also provides excellent visualization of the basal ganglia and their substructures [229,230] (Fig. 10) as well as the brainstem [231] comparable with a histology stain.

5.2.1.2. Neurodegenerative diseases. Changes in brain anatomy visualized by QSM have been reported for the substantia nigra during the course of Parkinson's disease [233]. SWI and QSM at UHF may provide the contrast and precision required for MRI-guided treatment strategies such as deep brain stimulation [226,234].

5.2.2. Vessel imaging, oxygenation

When arterial blood travels through the capillary system of the brain, oxyhemoglobin becomes partially deoxygenated, its magnetic susceptibility changes from diamagnetic to paramagnetic [235], and its T_2^* relaxation time decreases [236]. Deistung et al. [216] simulated the MR signal magnitude and phase of a voxel containing a vein and gray or white matter, and calculated the contrast between vein and GM/WM in GRE magnitude and phase images as well as in SWI. Signal changes in magnitude and phase as well as contrast in magnitude and SWI at 7 T were superior to those at lower field strength, and the maximal contrast was achieved at much shorter echo times (Fig. 11). As a change in blood oxygenation is directly related to a change in the susceptibility of blood, QSM can be used to track changes in blood oxygenation [235,237]. The high spatial resolution available with UHF MRI enables an assessment of the susceptibility within vessels.

5.2.2.1. Normal brain. In [238], using an automated vessel segmentation algorithm based on SWI, QSM, and R_2^* measurements, vascular trees with total length of 28.5 m ± 5.6 m at 7 T compared to 21.3 m ± 3.0 m at 3 T and 14.8 m ± 1.5 m at 1.5 T were measured. Consequently, UHF MRI enabled the visualization and segmentation of much finer vessels (Fig. 12). The microvenous anatomy of the hippocampus has been imaged [239] as well as the venous network of the dentate nucleus using SWI [240].

5.2.2.2. Functional MRI. Investigating brain activation based on SWI [241] or QSM [242] at UHF could be an interesting extension of functional MRI (cf. Section 9), as the effect of susceptibility-related blood oxygenation changes can be mapped more directly using QSM compared to the BOLD effect observed in the magnitude

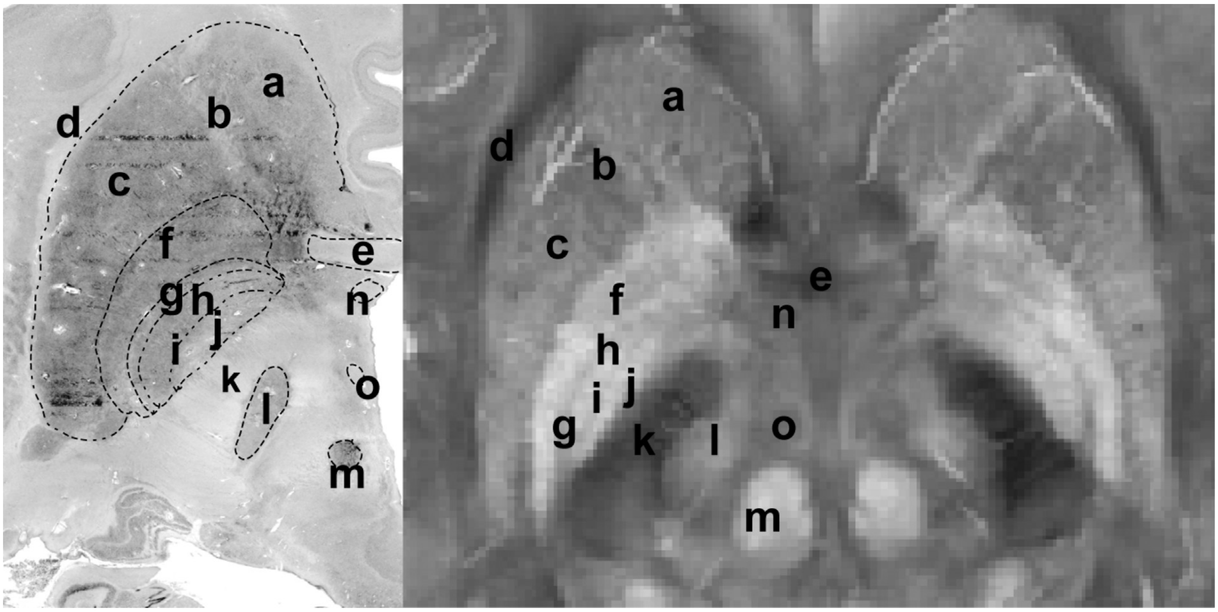

Fig. 10. The basal ganglia. (A) Digitized histologic cell body stain with brain structure contours showing globus pallidus next to a susceptibility map (B). In the susceptibility map, structures named on the myelin stain can clearly be delineated: (a) head of the caudate nucleus, (b) anterior limb of internal capsule, (c) putamen, (d) external capsule, (e) anterior commissure, (f) external globus pallidus, (g) lamina pallidi medialis, (h) pallidum mediale externum, (i) lamina pallidi incompleta, (j) pallidum mediale internum, (k) posterior limb of internal capsule, (l) subthalamic nucleus, (m) red nucleus, (n) fornix, and (o) mammillothalamic tract. The cell body stain is reproduced from BigBrain (https://bigbrain.loris.ca/) [232] under the license http://creativecommons.org/licenses/by-nc-sa/4.0/.

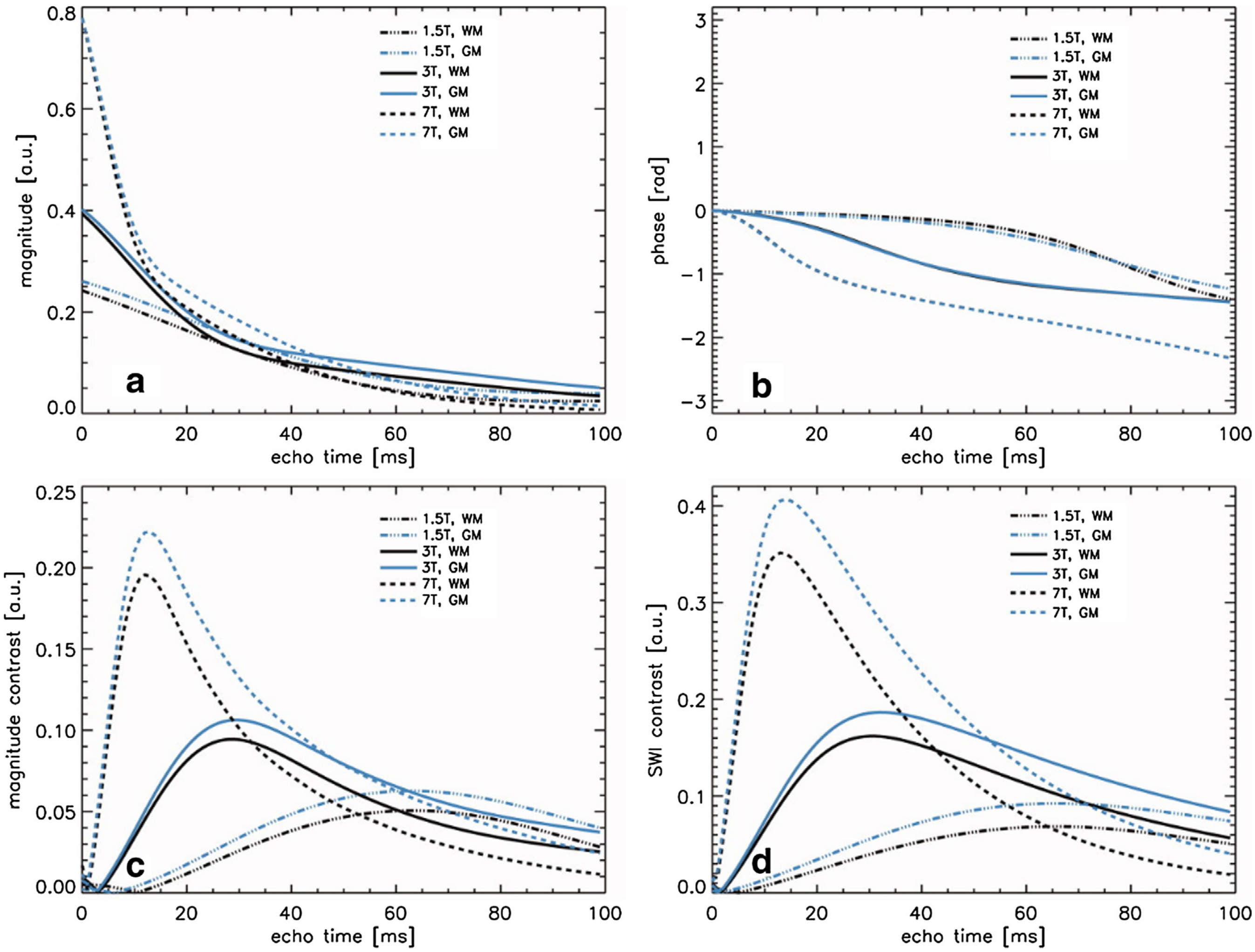

Fig. 11. Simulated MR signal magnitude (a) and phase (b) for a voxel containing a vein and gray or white matter for field strengths of 1.5 T, 3 T, and 7 T. The vein was oriented at an angle of 90° with respect to B_0. Magnitude contrast (c) and SWI contrast (d) were highest at 7 T for echo times of approximately 12–14 ms, and the contrast between vein and GM was higher than between vein and WM. Modified from [216].

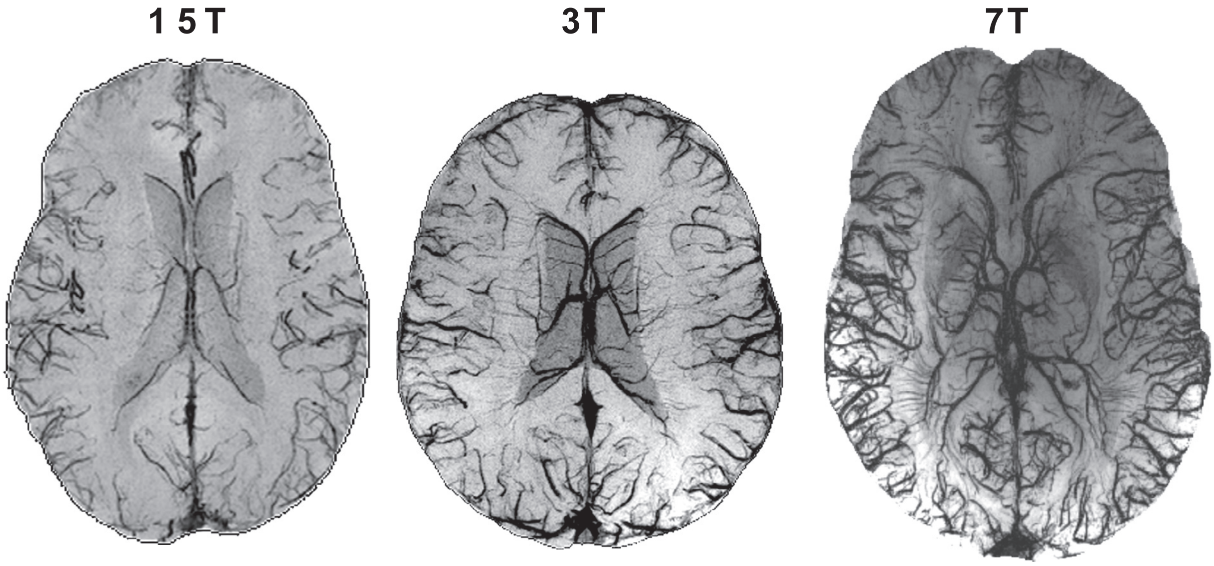

Fig. 12. Three SWI minimum intensity projections (mIPs) at 1.5 T, 3 T, and 7 T with resolutions of $0.7 \times 0.7 \times 1.0\ \text{mm}^3$, $0.5 \times 0.5 \times 1.0\ \text{mm}^3$ and $0.5 \times 0.5 \times 0.5\ \text{mm}^3$. Modified from [238].

images, though stronger orientation dependence could be a pitfall. For this purpose, UHF would be particularly useful due to its high CNR in the phase images.

5.2.2.3. Microbleeds, hemorrhage, and malformations. SWI and QSM are sensitive to hemorrhage due to the strongly paramagnetic susceptibility shown by deoxygenated blood and its byproducts (hemosiderin, methemoglobin). In a simulation study, MR magnitude and phase for a field strength of 7 T were shown to detect more voxels of cerebral microbleeds than magnitude and phase at 1.5 T or 3 T [243]. As higher SNR can be achieved at UHF than at lower field strengths, the authors assumed SNRs of 5–20 for 1.5 T and 3 T, and 23–47 for 7 T, but even when, for example, comparing the number of detected voxels at 3 T with an SNR of 20 and 7 T with an SNR of 23, the number of detected voxels at 7 T is approximately a factor of two higher. Although the higher possible resolution at UHF is highly beneficial for the detection of microbleeds, the use of longer echo times appeared to be as important as the use of higher field strength [244]. When imaging microbleeds occurring in vascular dementia, the authors of [244] found almost twice as many cerebral microbleeds at 7 T compared to 1.5 T using comparable sequence parameters (Fig. 13). UHF MRI using SWI is also an excellent modality to image brain tumor vessels and associated hemorrhage [245] as well as microbleeds observed as long-term effects of radiation therapy [246].

5.2.2.4. Multiple sclerosis. In [247], an increase in venous volume was observed using SWI when investigating intralesional veins in newly detected multiple sclerosis (MS) lesions compared to older lesions, which was attributed to more strongly deoxygenated venous blood and/or increased venous diameter due to increased metabolic activity. The reliable detection of small intralesional veins proved useful for the differentiation between MS and neuromyelitis optica, as intralesional veins were generally observed in MS but were absent in neuromyelitis optica in most lesions [248] (Fig. 14).

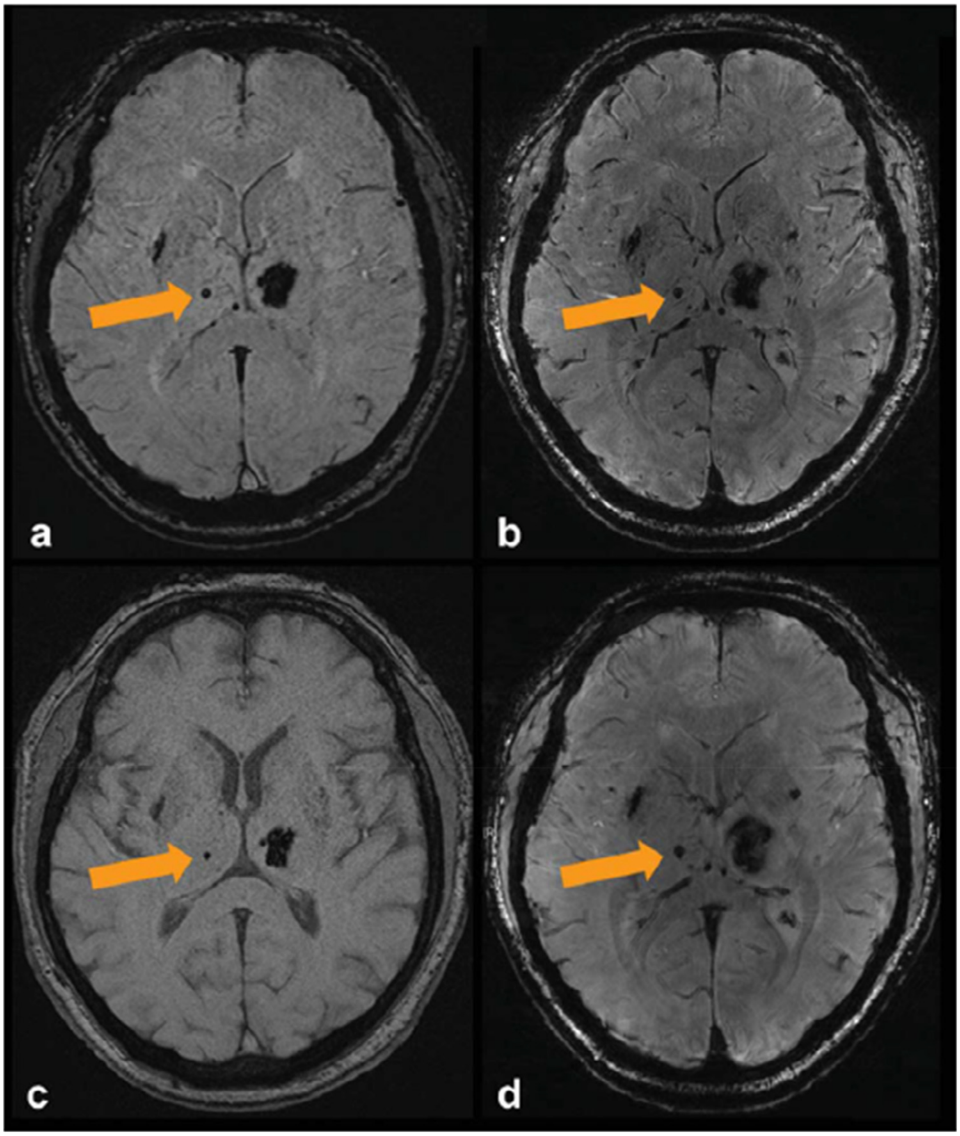

Fig. 13. SWI of cerebral microbleeds in patients with vascular dementia. Measurements at 1.5 T with resolution of 0.4 × 0.4 × 1.6 mm^3 and echo time of 40 ms (a) are compared with a highly resolved SWI at 7 T with resolution of 0.2 × 0.2 × 1.5 mm^3 and echo time of 15 ms (b). Furthermore, susceptibility-weighted images measured at 1.5 T (c) and 7 T (d) with identical parameters (resolution 0.3 × 0.3 × 3.0 mm^3, TE = 15 ms) are shown. The arrows mark the same cerebral microbleed in all images. Reproduced from [244].

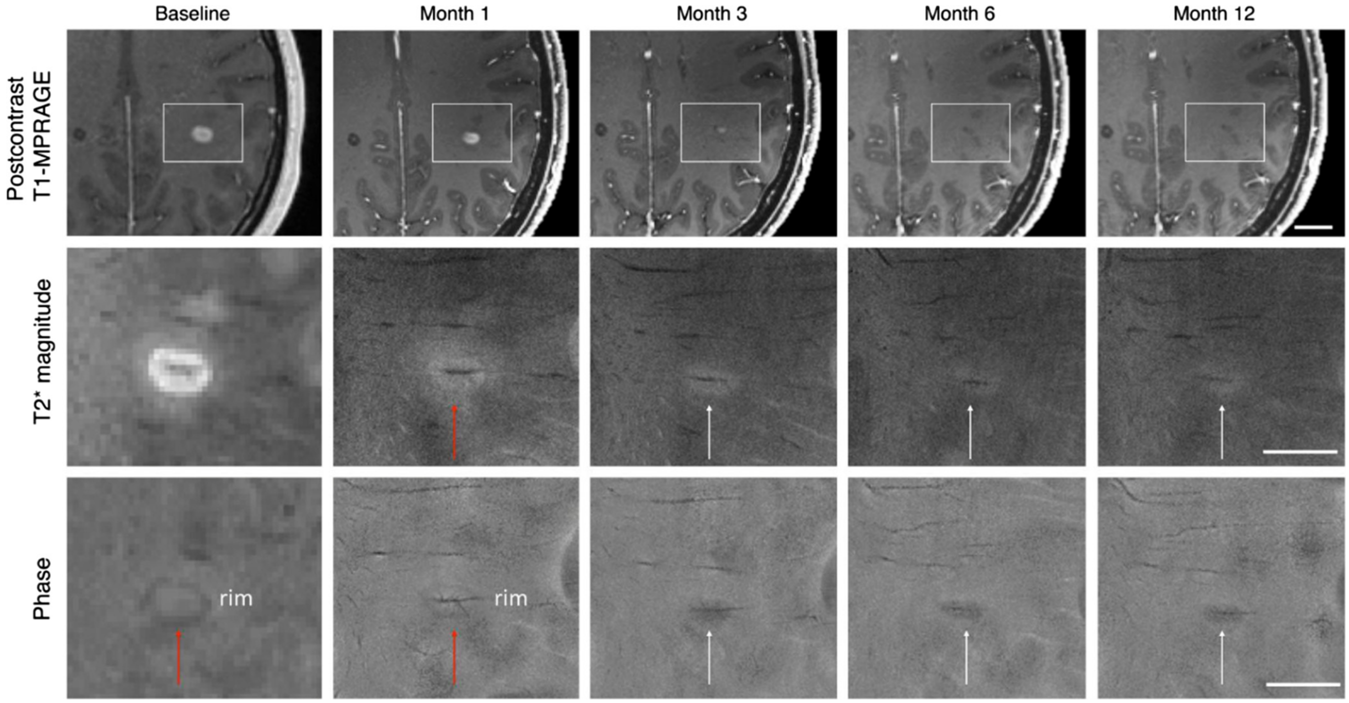

Fig. 14. Longitudinal measurements of contrast-enhanced T_1-weighted and T_2^*-weighted images as well as phase images of an MS lesion. In phase images measured at 3 T (column 1, baseline), the central vein in the MS lesion is only very vaguely visible (first column), whereas it can be clearly seen when using 7 T MRI (columns 2–5). The phase rim gradually resolves compared to the baseline and the measurement after one month. Scale bar = 10 mm. Modified from [249].

5.2.3. *Imaging and quantification of nonheme iron and mineralization*

Iron quantification at UHF also benefits from the high CNR and higher achievable resolution, since relevant structures for iron quantification can be better delineated from their surroundings and substructure becomes visible (cf. Section 5.2.1).

5.2.3.1. Tumors. QSM is able to visualize calcification in glioblastoma and enables a reliable differentiation between calcification and hemorrhage due to their different susceptibilities [222]. Detecting calcification in glioblastoma could enable a differentiation of glioblastoma with and without an oligodendroglial component, which could be relevant when providing a prognosis for patients.

5.2.3.2. Multiple sclerosis lesions. Using QSM, iron accumulation in the caudate and putamen showed a relation to the Flanker interference (a cognitive measure) [250]. The high spatial resolution available at UHF enabled a detailed classification of MS lesions, whose appearance is related to iron accumulation, using both phase and susceptibility maps [249,251]. Cortical lesions could not be detected as reliably with 3 T MRI as with 7 T MRI [252].

5.2.3.3. Neurodegenerative diseases. Iron accumulation or iron depletion in different brain nuclei and in the cortex has been reported in various neurodegenerative diseases. For example, in Alzheimer's disease a co-localization of amyloid plaques with iron [253] is in agreement with phase changes observed in the cortex [254]. Significant susceptibility changes related to iron accumulation in patients with pre-manifest Huntington's disease have been measured for caudate nucleus, putamen, and globus pallidus compared to healthy controls [255].

5.2.4. *Applications in the body*

Outside of the brain at UHF, myocardial microstructure has been assessed with SWI using a dedicated 16-channel transmit/receive coil array [256] and volume selective B_0 shimming [257]. QSM has been applied to the knee at 7 T [258], and it has been shown that QSM is sensitive to degenerative changes within articular cartilage. The inhomogeneous B_0 [257,259] and B_1 fields [16] as well as the scarce availability of dedicated RF coils make UHF MRI of the torso challenging. To cope with B_1 inhomogeneities, UHF imaging of the body trunk requires the use of parallel transmission techniques (cf. Section 3). Respiration and organ motion must also be accounted for. Besides the challenges generally encountered in UHF body imaging, susceptibility mapping outside the brain is complicated by various effects that are not present in brain imaging. When imaging organs or body regions where fat is present, a phase map that accounts for chemical shift has to be reconstructed [260]. For the reconstruction of a chemical-shift-encoded phase map, the acquisition of a multi-echo GRE is required. Subtle field variations near air-tissue interfaces impede background field removal, for example, when imaging the liver, and large field variations are caused by the air-filled lungs [261].

6. X-nuclei imaging

6.1. *Technical aspects*

In[1] order to characterize various cellular metabolic processes, a non-invasive measurement via MRI or MRS of nuclei other than ^{1}H is often desirable. These nuclei are usually denoted as X-nuclei. Only nuclei with an odd number of protons and/or an odd number of neutrons have a magnetic spin moment and, thus, are visible for MRI/MRS. Theoretically, these nuclei comprise approximately 2/3 of all isotopes. However, despite the large number of isotopes that possess a nuclear spin, only a few of them are applied in MRI/MRS. Over the past decade, the progress in ultra-high-field MRI ($B_0 \geq 7$ T) has led to an increase in technical X-nuclei MRI research. The achieved

---

[1] Parts of Section 6 are based on [262] and [263].

technical improvements have in turn resulted in emerging clinical research applications.

X-nuclei can be grouped into spin-½ nuclei (e.g. ^{13}C, ^{19}F, ^{31}P) and quadrupolar nuclei (i.e. spin >½; e.g. ^{17}O, ^{23}Na, ^{35}Cl, ^{39}K). The focus of this section will be on imaging of X-nuclei. Since spin-½ X-nuclei are often used for MR spectroscopy and, thus, are in part covered in Section 7, the main focus of this section will be on imaging of quadrupolar nuclei.

X-nuclei MRI is challenging for several reasons. The most limiting issue is the low SNR, which is more than two orders of magnitude lower than the SNR of conventional ^{1}H MRI. The main causes for this fact are the low MR sensitivities (γ^3 I (I + 1)) and low in-vivo concentrations c:

$$Signal \propto c \cdot I \cdot (I+1) \cdot \gamma^3 \tag{4}$$

Although the magnetic spin moment (I) of most X-nuclei is higher than for ^{1}H, this does not fully compensate for the loss caused by the lower gyromagnetic ratio (γ). Except for tritium (^{3}H), all X-nuclei exhibit much lower intrinsic MR sensitivities compared to protons (1H) [264]. The low in-vivo concentrations are either caused by a low in-vivo abundance of the element (e.g. phosphorus or sodium) or by a low natural abundance of the investigated isotope (e.g. ^{17}O, ^{13}C) (see Table 2).

The SNR – as potentially the most relevant quantity for image quality in X-nuclei MRI – is the ratio of the signal and the noise. The latter also depends on the system frequency and, thus, on the gyromagnetic ratio. Because of the markedly lower γ of most X-nuclei versus ^{1}H, the quasi-static approximation (cf. Section 1.1.1) is valid for these nuclei even at 7 T, and the classical calculation of SNR can be utilized. For volume RF coils and large samples, a linear relationship between frequency and image noise is usually assumed. This assumption is fulfilled if the main causes for image noise are inductive losses in the investigated sample (i.e. "sample-dominated losses") [274]. For small RF coils and/or small samples (e.g. small-animal imaging or high-density array coils in human MRI), electronic losses – caused by the skin effect – can also be a major source of image noise. In this case, the relationship between the frequency and noise is described by noise $\propto \omega^{1/4}$ [17]. Thus, it can be reliably assumed that SNR increases at least proportional to γ^2 but lower than $\gamma^{2.75}$:

$$SNR \propto c \cdot I \cdot (I+1) \cdot \gamma^{2to2.75} \tag{5}$$

This translates into an SNR increase with B_0 as described in Eq. (6), since the frequency also scales linearly with the main magnetic field (B_0):

$$SNR \propto B_0^{1to1.75} \tag{6}$$

This relationship is often the motivation for the establishment UHF MRI systems, including potential future systems operating at 14 or 20 T [275,276].

However, many other parameters that influence SNR and overall image quality change with increasing magnetic field strength (see Table 1). For example, the ratio of T_2^* to T_1 also influences the SNR that can be achieved within a given measurement time:

$$SNR \propto \sqrt{T_2^*/T_1} \tag{7}$$

This can be a disadvantage for UHF MRI, since water relaxation times show an increase in T_1 and a decrease in T_2 with field strength [277]. However, various mechanisms such as the dipole-dipole interaction, chemical shift anisotropy relaxation, and electric quadrupolar relaxation can contribute to the relaxivity [278]. For example, for ^{31}P an increasing contribution from chemical shift anisotropy relaxation to the T_1 relaxation is expected to be responsible for shorter cardiac T_1 relaxation times at 7 T than at 3 T ($T_1 \propto B_0^{-2}$) [279]. In MRS, the shorter T_2 (and hence T_2^*) can also result in an increase in spectral linewidth, which counteracts the higher spectral resolution that can be achieved at UHF (cf. Section 7.1). In the case of spin >½ nuclei, the relaxation is usually dominated by the electrical quadrupolar interaction. For ^{23}Na and ^{39}K it was shown that outside of the extreme narrowing regime ($\omega_0\tau_C \ll 1$, e.g. in fluids, where τ_C denotes the rotational correlation time), both the T_1 and T_2 relaxation times increase with field strength [280]. Thus, T_1 of tissue increases with field strength and T_1 of fluids (extreme narrowing regime) remains constant. This can be an advantage for quantitative ^{23}Na and ^{39}K MRI, since the differences between the T_1 relaxation times of tissue and fluids decrease with increasing field strength. Thus, spin-density weighting can be achieved within shorter repetition times. On the other hand, this leads to a decrease in efficiency for relaxation-weighted techniques such as inversion recovery imaging [281,282]. In addition, $T2^*$ weighting that is caused by the short transverse relaxation times might be reduced at the higher field strength.

Table 2

Selected isotopes that can be used for MRI and MRS. Values for the gyromagnetic ratio and natural abundances are adapted from Harris et al. [264]. To calculate the relative SNR, Eq. (5) was applied using a linear noise model (i.e. SNR $\propto \gamma^2$). Potential influences from differences in relaxation times were neglected.

Nucleus (Spin I)	Gyromagnetic ratio γ [MHz/T]	Natural abundance [%]	Typical in-vivo concentrations c [mol/L] of the isotope	Relative in-vivo SNR [%]
^{1}H (1/2)	42.58	99.99	79[a]	100
^{13}C (1/2)	10.71	1.07	≈0.005[b]	$4.0 \cdot 10^{-4}$
^{19}F (1/2)	40.08	100	≈0.001[c]	$1.1 \cdot 10^{-3}$
^{31}P (1/2)	17.25	100	0.003[d]	$6.2 \cdot 10^{-4}$
			0.025[d]	$5.2 \cdot 10^{-3}$
^{23}Na (3/2)	11.27	100	0.041[e]	$1.8 \cdot 10^{-2}$
			0.3[e]	$1.3 \cdot 10^{-1}$
^{35}Cl (3/2)	4.18	75.78	0.027[f]	$2.2 \cdot 10^{-3}$
^{39}K (3/2)	1.99	93.26	0.108[g]	$1.6 \cdot 10^{-3}$
^{17}O (5/2)	−5.77	0.038	0.015[h]	$4.1 \cdot 10^{-3}$

[a] ^{1}H concentration was derived from measured water content (71%) of brain white matter [265].

[b] Measured peak 1-^{13}C glucose concentration after intravenous infusion of ^{13}C-labeled glucose [266].

[c] Physiological concentrations of detectable mobile fluorine are below the detection limit (usually less than 10^{-3} μmol/g wet tissue). Concentrations of fluorine-containing pharmaceuticals are often in the range of 1 mmol/L [267].

[d] ^{31}P concentrations are given for PCr in brain and skeletal muscle tissue. Concentrations of other ^{31}P-containing metabolites are often much lower (e.g. ATP or inorganic phosphate in skeletal muscle tissue) or in the same range (e.g. ATP in brain tissue) [268].

[e] Measured sodium concentration of healthy brain white matter [269]. Healthy articular cartilage exhibits the highest sodium content among all tissues [270].

[f] Measured chloride concentration of healthy brain white matter [271].

[g] Measured potassium concentration of skeletal muscle tissue [272].

[h] ^{17}O concentration of healthy brain white matter (natural abundance). During an inhalation study with enriched $^{17}O_2$, a typical increase in the ^{17}O concentration is 30% [273].

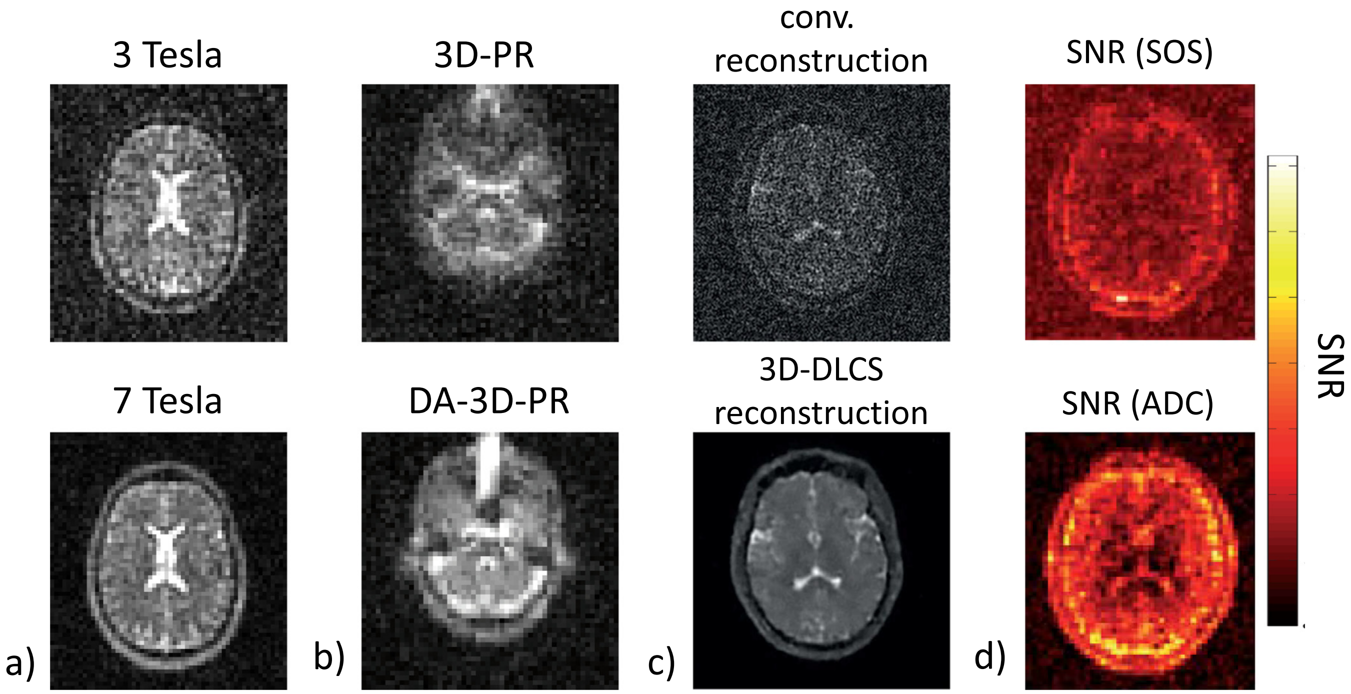

Fig. 15. There are several possibilities to improve X-nuclei image quality. This is demonstrated for the example of ^{23}Na MRI. (a) Increasing the field strength leads to an approximately linear increase in SNR [283]. (b) Optimized acquisition techniques such as density-adapted sampling further increase SNR and reduce image artifacts [284]. (c) Iterative image reconstruction techniques such as 3D dictionary learning compressed sensing enable precise reconstruction with markedly reduced noise and artifact levels [285]. (d) Phased-array RF receive coils can further improve SNR. The adaptive combination (ADC) algorithm leads to a distinct increase in SNR compared to a sum-of-squares (SOS) reconstruction [286]. Parts of the figure were taken from [287,284], and [286] with permission of John Wiley and Sons. Part (c): Courtesy of Nicolas G.R. Behl, Medical Physics in Radiology, German Cancer Research Center (DKFZ), Heidelberg, Germany.

To achieve optimal image quality and also high quantitative accuracy in X-nuclei MRI, it is important to optimize the data acquisition, image reconstruction, and post-processing (Fig. 15). Since SNR increases linearly or even more than linearly with magnetic field strength (cf. Eq. (6), X-nuclei MRI strongly benefits from UHF (Fig. 15a). For nuclei that are imaged beyond the quasi-static regime (e.g. ^{1}H and ^{19}F at 7 T), the SNR benefit of UHF can be even higher [25] (cf. Section 1.1.1). In addition, image acquisition (Fig. 15b), image reconstruction (Fig. 15c and d), and image post-processing have to be optimized. All of these steps benefit from the technical developments and improvements that have emerged with the increasing availability of UHF systems.

6.1.1. Hardware-based advances

Since all isotopes exhibit different Larmor frequencies, X-nuclei MRI requires dedicated hardware, such as a broad-band RF amplifier and appropriate transmit and receive RF coils. Although single-resonant coils are available that are tuned to the desired X-nucleus frequency, double-tuned coils that are tuned to both the desired non-proton frequency and the ^{1}H frequency are usually preferred. The latter enable co-registered acquisition of morphological images and non-proton data. Additionally, phase maps based on ^{1}H MRI facilitate B_0 shimming. At clinical field strengths (e.g. 3 T), the integrated ^{1}H body coil is often used for basic ^{1}H MRI in combination with local, single-tuned X-nuclei coils (e.g. [288,289]). At clinical field strength, the integrated ^{1}H body coil impedes the design of an X-nuclei body resonator, since shielding is required [290]. At UHF there is usually no integrated body coil for ^{1}H MRI, which may improve the performance of X-nuclei body coils. The concept of a large body resonator that is tuned to the desired X-nuclei frequency has been pursued for both ^{23}Na and ^{31}P MRI to achieve homogenous excitation over a large body region [290–292]. However, the limited power of available broad-band amplifiers often restricts the performance of X-nuclei body coils. To enable abdominal X-nuclei MRI, phased-array coils have also been employed (e.g. [293,294]).

Phased-array receiver coils can exploit the increased sensitivity of small surface coil elements [295]. Phased-array technology is well established in ^{1}H MRI; however, most X-nuclei MRI studies have been performed using single-channel RF receive coils. As outlined above, dual-tuned or dual-frequency designs are desirable. Inclusion of a ^{1}H channel, however, makes the design of efficient X-nuclei multi-channel RF coils more challenging. For ^{23}Na MRI of the human brain at 9.4 T, Shajan et al. presented a 27-channel ^{23}Na receive helmet that is surrounded by a four-channel Tx/Rx ^{23}Na array and a four-channel Tx/Rx ^{1}H dipole array [296]. At 7 T, designs for a 15-channel [297] and a 30-channel ^{23}Na head array coil have been presented [298]. Up-to-date overviews about high-performance RF coils for ^{23}Na MRI can be found in Wiggins et al. [299] and Bangerter et al. [300]. For other nuclei such as ^{31}P, sophisticated array coils are also available, e.g. [301].

To further increase the efficiency of X-nuclei MRI, several setups for time-efficient interleaved or simultaneous imaging of two nuclei have been presented [302–304]. Additionally, a decisive advantage for X-nuclei MRI is that the RF wavelength for most X-nuclei (except for ^{19}F) is more than a factor of two longer than the RF wavelength of ^{1}H. Thus, at currently used field strengths ($B_0 \leq 9.4$ T), whole-body X-nuclei MRI does not require parallel transmission capability (cf. Section 3). Nevertheless, B_1 inhomogeneities resulting from local X-nuclei coils can lead to a bias in quantitative X-nuclei MRI, although there are techniques available to correct this bias [305,306].

6.1.2. Image acquisition, image reconstruction, and post-processing

To enable efficient imaging of quadrupolar nuclei, acquisition techniques that enable ultra-short echo times (UTE) are a prerequisite [307]. In addition, X-nuclei MRI benefits from advanced UTE techniques such as density-adapted projection reconstruction (DA-3D-PR, Fig. 15b) [284,308,309], twisted projection imaging (TPI) [310,311], 3D CONES [312], or Fermat-looped orthogonally-encoded trajectories (FLORET) [313]. As discussed in Section 6.1.1, phased-array receiver coils can be used to further increase SNR. However, the low SNR of X-nuclei MRI poses a different situation than in ^{1}H MRI for the combination of signals from different coil elements. A simple sum-of-squares (SOS) reconstruction to combine the signals from each individual coil element leads to severe noise amplification (see Fig. 15d). Therefore, methods that exploit the knowledge of the sensitivity profiles of all coil elements in each voxel, such as the adaptive combination (ADC) algorithm [286,314] or the SENSitivity Encoding (SENSE) method [315] have to be applied.

However, low spatial resolution and fast transverse relaxation can still result in substantial partial volume effects that lead to a bias in quantitative X-nuclei MRI. It has been shown that the application of the geometric transfer matrix method, which was developed for positron emission tomography, can markedly reduce this bias [269]. In addition, it has been shown that iterative partial volume correction enables improved determination of $T2^*$ relaxation times in ^{23}Na, ^{35}Cl, and ^{17}O MRI [316]. Also, high-resolution anatomical information from ^{1}H MRI can be used to reduce partial volume effects and to increase the image quality in X-nuclei MRI. Even the most basic anatomical information, i.e. the shape of the object, can be incorporated into the iterative image reconstruction process to improve image quality [317]. Information about tissue boundaries can further reduce image blurring and partial volume effects [318].

Nevertheless, compressed sensing (CS) [319,320] and related iterative reconstruction algorithms are still rarely used in X-nuclei MRI [317,321,322], although they yield significant improvements in image quality. For example, 3D dictionary learning compressed sensing (3D-DLCS) enables precise reconstruction of undersampled ^{23}Na MRI data with markedly reduced noise and artifact levels compared to conventional reconstruction [285] (Fig. 15c). The applicability of CS to ^{23}Na MRI also benefits from the use of ultra-high fields, since increased spatial resolution leads to increased matrix sizes and, thus, to increased compressibility of the ^{23}Na MRI datasets.

A disadvantage of UHF MRI is that SAR constraints often restrict optimal pulse sequence parameters [323]. In the future, new acquisition strategies such as sweep imaging with Fourier transformation (SWIFT) might be applied to overcome this limitation [324].

6.2. Applications

6.2.1. Imaging of ions (Na^+, K^+, Cl^-)

Sodium ions (Na^+), potassium ions (K^+), and chloride (Cl^-) play an important role in many cellular physiological processes. The high concentration gradients across the cell membranes for these ions are the physiological basis for the excitation and inhibition of cells. In healthy tissue, the extracellular concentration of Na^+ is approximately ten-fold higher than the intracellular concentration ($[Na^+]_i = 10–15$ mmol/L, $[Na^+]_e = 145$ mmol/L). The gradient of the K^+ concentration is reversed compared to the Na^+ gradient and even more pronounced. The enzyme Na^+-K^+-ATPase helps to maintain this gradient by pumping Na^+ out and K^+ into the cell with a ratio of 3:2. This process is essential for the cells' resting membrane potential and, thus, also influences cell excitability. A breakdown of this concentration gradient or an increase in the intracellular Na^+ content is an early marker in many disease processes. Cl^- is the most abundant anion in the human body. It is involved in various cellular processes such as the inhibition of muscular [325] and neuronal cells [326], cell volume regulation [327], and cell migration in cancer [328,329].

Whereas ^{23}Na MRI of the normal and diseased human brain had already been performed more than 30 years ago at low field strength (1.5 T) [330], the feasibility of ^{35}Cl and ^{39}K MRI for in-vivo human brain and muscle tissue was only demonstrated recently using 7 T [271,272] and 9.4 T [331] systems. Compared to ^{23}Na MRI, ^{35}Cl and ^{39}K MRI have approximately 8- and 11-fold lower SNR, respectively (see Table 2). Thus, in-vivo ^{35}Cl and ^{39}K MRI were considered to be impractical for many years. In 2009, Augath et al. presented the first in-vivo ^{39}K images of the rat brain using a 9.4 T small-animal MRI system [332]. One year later, the first in-vivo ^{35}Cl images of rat brain were published [333]. At 9.4 T, low spatial resolution still impedes broader application in preclinical research. However, imaging of these nuclei greatly benefits from ultra-high magnetic field strengths, e.g. 21.1 T [280,334].

^{23}Na MRI has been applied in a large variety of biomedical research applications [335]. This topic is covered by several review articles (e.g. [270,336–341]). Whereas ^{23}Na MR studies are frequently performed as part of clinical research, ^{35}Cl MRI has only been rarely investigated [271,342] (cf. Fig. 16), and ^{39}K MRI has only been applied to a few healthy subjects. In general, non-invasive quantification of these ions is highly desirable to investigate in-vivo ion homeostasis.

6.2.2. ^{23}Na MRI of human brain

Most of the ^{23}Na MRI studies performed so far were focused on the brain. ^{23}Na MRI has been applied to study brain tumors [282,337,343–346], ischemic stroke [347,348], Alzheimer's disease [349], Huntington's disease [350], epilepsy [351], ageing [352], traumatic brain injury [353], and multiple sclerosis [354]. Sodium ion channels and sodium accumulation are expected to play a role in the pathogenesis of multiple sclerosis [355,356]. In brain tumors, Na^+ concentrations are typically increased. This increase can be caused by edema, i.e. increased extracellular volume fraction, or by an increase in the intracellular concentration, e.g. due to cell depolarization. Sodium inversion recovery imaging might help to differentiate between these two underlying possibilities [282] (cf. Fig. 16). In ischemic stroke, ^{23}Na MRI might be used to identify regions with preservation of ionic homeostasis [357]. Tissue sodium concentrations above approximately 70 mmol/L indicate irreversible tissue damage [348]. However, long acquisition times and the experimental character of ^{23}Na MRI (e.g. the requirement for a change of the RF coil between ^{1}H and ^{23}Na) have so far prevented application of ^{23}Na MRI in larger clinical studies that involve stroke patients. ^{23}Na MRI can also be used to study the cell volume fraction during normal ageing [352], where it was shown that the in-vivo tissue cell volume fraction remains constant with advancing age in all brain regions in normal individuals. ^{23}Na MRI of the human brain largely benefits from the application of UHF systems, since the increased spatial resolution reduces partial volume effects and, thus, facilitates the analysis of small structures and lesions.

6.2.3. ^{23}Na MRI of the musculoskeletal system

There are also several ^{23}Na MRI studies that have focused on muscle tissue. Elevated muscular tissue Na^+ content that is either a consequence of the disease process or a major driver in the progression of the disease is observed in many pathologies such as myotonic dystrophy [358,359], Duchenne muscular dystrophy [360,361], hypertension [362], severe kidney disease [363], heart failure [364], and muscular channelopathies [365–367]. Compared to other organs such as the brain, skin, and cartilage tissue, high spatial resolution is less crucial for ^{23}Na MRI of skeletal muscle. Although ^{23}Na MRI of muscle tissue also benefits from UHF MRI

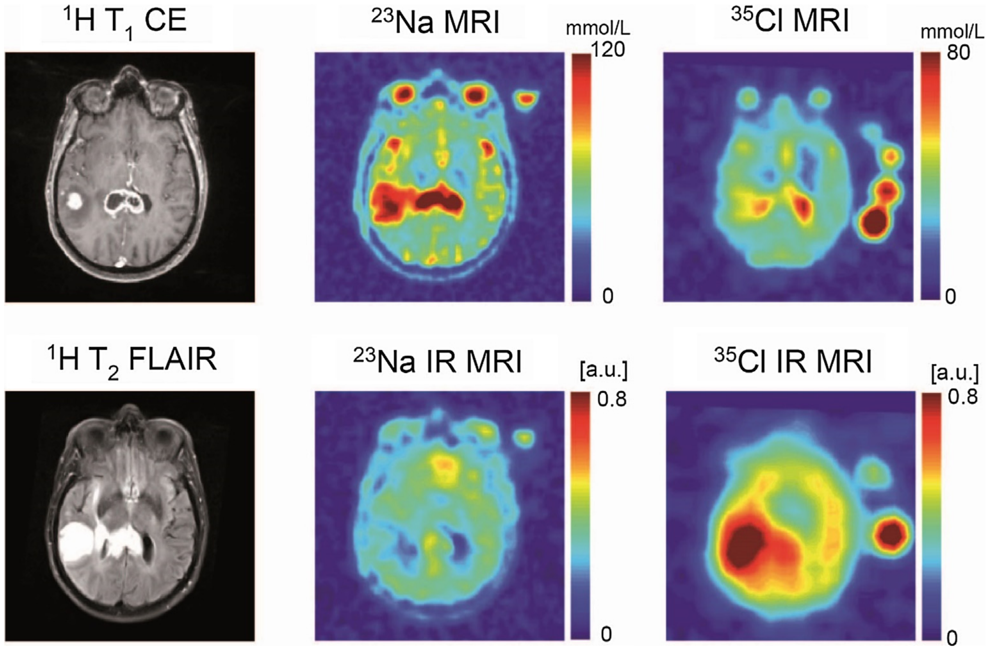

Fig. 16. Glioblastoma multiforme of the right temporal lobe and the corpus callosum. 1st column: Contrast-enhanced ^{1}H T1-weighted (^{1}H T1 CE) and ^{1}H T2-weighted fluid-attenuated inversion recovery (IR) (^{1}H T2 FLAIR) show visualization of contrast-enhancing parts and perifocal edema. 2nd column: Concentration-weighted ^{23}Na MR imaging (^{23}Na MRI) reveals elevated signal intensity in all parts of the tumor, whereas ^{23}Na IR MRI showed parts with reduced and others with increased signal intensities. 3rd column: Slightly increased signal intensities are also visible in concentration-weighted ^{35}Cl MR imaging. In contrast to ^{23}Na IR MR imaging, ^{35}Cl IR MR imaging reveals a strong signal increase in the affected brain region. ^{1}H images were acquired at 3 T, ^{23}Na and ^{35}Cl images at 7 T. Each ^{23}Na and ^{35}Cl examination required approximately 10 min measurement time. Figure and figure caption adapted from [271]. With permission of the Radiological Society of North America (RSNA).

[368], reliable ^{23}Na MRI examinations of muscle tissue can also be performed at lower field strengths, e.g. 3 T.

Among all tissues of the human body, healthy cartilage tissue contains the highest Na$^+$ content (≈300 mmol/L). Cartilage contains proteoglycans that have at least one glycosaminoglycan (GAG) side chain. These GAGs are negatively charged and attract positively charged ions, mainly Na$^+$. Cartilage degeneration is associated with a decrease in GAG content and a corresponding decrease in Na$^+$ content. Thus, the Na$^+$ content of cartilage is considered to be an important biomarker for cartilage degeneration, e.g. in osteoarthritis [369,370]. Among other applications, ^{23}Na MRI of cartilage tissue has been applied to measure the fixed charged density in articular cartilage [371], to quantify Na$^+$ in the human wrist [372], to analyze the Na$^+$ content after knee matrix-associated autologous chondrocyte transplantation [373] (Fig. 17), and to investigate Na$^+$ in lumbar intervertebral disks [374] and the ankle joint [375]. Promising results have already been achieved at lower field strength, e.g. 4 T [376,377]. However, even at $B_0 \geq 7$ T, ^{23}Na MRI suffers from low spatial resolution and corresponding partial volume effects. For example, Na$^+$ signal from the surrounding synovial fluid can bias the measured Na$^+$ content. ^{23}Na inversion recovery MRI can be applied to reduce this bias [378]. Given the small thickness of cartilage tissue and the inherently low spatial resolution of ^{23}Na MRI, UHF systems seem to be a prerequisite for establishing ^{23}Na MRI as a clinical tool for the investigation of cartilage degeneration.

6.2.4. ^{23}Na MRI in other body parts

^{23}Na MRI has only rarely been applied beyond the human brain and musculoskeletal system. This is most likely due to the limited

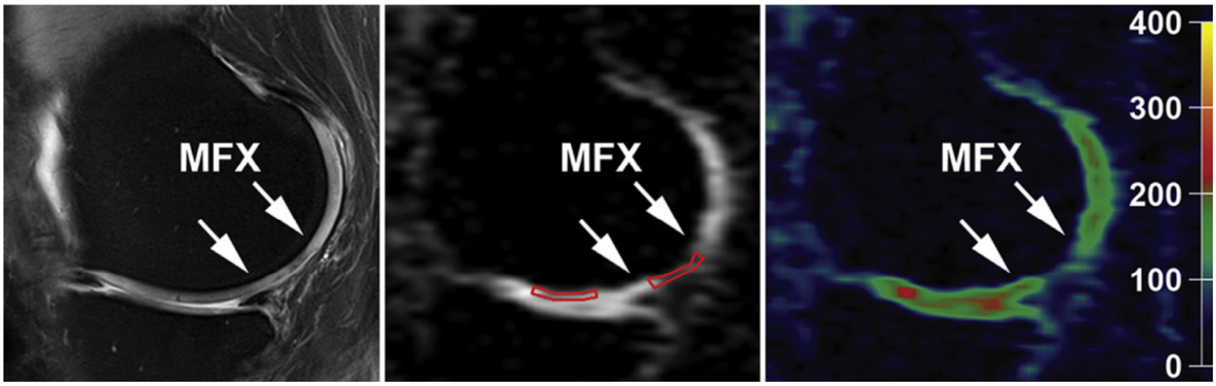

Fig. 17. Sagittal proton-density-weighted 2D TSE MR image with fat suppression (left), sagittal sodium 3D GRE image (middle), and color-coded sagittal sodium 3D GRE image (right) in a 43-year-old woman obtained 42 months after a microfracture (MFX) procedure. Cartilage repair tissue is situated between the two arrows. Red contours in the middle image represent the ROI analysis of repair tissue (right contour) and reference cartilage (left contour). Color scale represents the sodium signal intensity values. Reproduced from [388]. With permission of Elsevier.

availability of dedicated RF coils. However, a large variety of interesting research applications benefit from the increased SNR available at ultra-high field strengths. For example, ^{23}Na MRI studies have been performed in breast cancer patients [379,380] and for therapy monitoring of breast cancer [381], to investigate lung tumors [382], to investigate kidney function [383], and to analyze Na^+ storage in skin tissue, which seems to play an important role in salt-sensitive hypertension [384]. However, ^{23}Na MRI of skin is challenging due to the small thickness of the skin. It could be shown that UHF ^{23}Na MRI combined with dedicated RF coils enables reliable quantification of the skin Na^+ content [385]. At ultra-high magnetic field strengths, cardiac sodium MRI might also evolve into a clinical research tool to investigate tissue viability [386]. However, even at a magnetic field strength of 7 T, cardiac sodium MRI remains challenging due to breathing and cardiac motion [387]. In addition, the large difference in sodium concentration between blood and muscular tissue increases partial volume effects that hamper quantitative cardiac sodium MRI.

6.2.5. ^{17}O MRI

The low natural abundance of ^{17}O (see Table 2) enables MRI studies with enriched $^{17}O_2$ as a tracer. ^{17}O MRI can non-invasively determine the cerebral metabolic rate of oxygen consumption ($CMRO_2$) [389–393]. The latter can be regarded as an indicator for cell viability. Reduced $CMRO_2$ was reported in cancer ("Warburg effect") [394], Parkinson's, and Alzheimer's disease [395,396] and, thus, might evolve into a valuable diagnostic marker.

Although indirect ^{1}H-MRI-based methods are available to determine $CMRO_2$, they rely on several assumptions that might hamper quantitative accuracy. ^{15}O positron emission tomography (PET) is still considered to be the gold standard for localized quantification of $CMRO_2$. However, ^{15}O PET has never been established in the clinical routine since it requires an on-site cyclotron (due to the short half-life of ^{15}O) and complicated modeling of the oxygen metabolism. The latter is caused by the fact that the tracer ^{15}O is visible in PET irrespective of its molecular environment. In contrast, ^{17}O remains invisible in MRI until it is metabolized to $H_2{}^{17}O$. Thus, $CMRO_2$ can be calculated based on the production of $H_2{}^{17}O$ and by employing a three-phase metabolic model [392].

A limitation of ^{17}O MRI is the high cost of enriched $^{17}O_2$ gas, in the range of 2500 $/L, which hinders application in broader clinical studies. Thus, dedicated inhalation systems [273,397,398] are mandatory to ensure efficient use of the $^{17}O_2$ gas. The largest study in humans that has been published so far comprises three healthy subjects. To demonstrate that $CMRO_2$ can be reproducibly measured, the healthy subjects in this study were examined twice [273]. Although the feasibility of ^{17}O MRI has also been demonstrated at 3 T [399], ^{17}O greatly benefits from ultra-high magnetic field strengths [400,401]. Hoffmann et al. performed the first ^{17}O inhalation experiment in a brain tumor patient using a 7 T system [402]. Reduced $CMRO_2$ values were found in all tumor compartments (Fig. 18).

In summary, UHF MRI enables clinical research applications of ^{23}Na MRI and imaging of nuclei with even lower in-vivo sensitivity such as ^{17}O, ^{35}Cl, and ^{39}K with sufficient spatial resolution and within clinically feasible measurement times. Technological advances such as new RF coil designs, efficient image acquisition techniques, and sophisticated image reconstruction and post-processing techniques further improve the capabilities of X-nuclei imaging at UHF. Due to the increasing availability of UHF systems, technical advances, and the large variety of clinical research applications, X-nuclei MRI has the potential to evolve from a clinical research tool into a diagnostic tool in the near future.

7. MR spectroscopy and spectroscopic imaging

7.1. Technical aspects

Both ^{31}P NMR spectroscopy and ^{1}H MRI were developed in the 1970s, and, initially, phosphorus spectroscopy was thought to be the more specific technique, providing direct access to clinical biochemistry and energy metabolism in vivo. Early in-vivo data were collected during rest as well as after metabolic challenges in animals and humans (e.g., [403–407]). Consequently, early high-field systems (1.5–2 T) for humans were designed to provide both imaging and spectroscopy options [408–410]. However, the sensitivity at 1.5–2 T resulted in limited spatial resolution for localized MRS and MR spectroscopic imaging (MRSI), even with long scanning durations, which may have limited the insights provided by either ^{1}H or ^{31}P MRS.

Thus, proton imaging succeeded clinically, as gray scale images were much faster to scan and easier to interpret by radiologists based on their anatomical expertise (although the specificity was also rather limited at this early stage and sometimes still is, particularly without use of exogenous contrast agents). Nevertheless, single-voxel ^{1}H MRS was approved for clinical use, and it has been employed successfully for a number of disorders at 1.5 T or 3 T, including brain tumors in adults [411–414] and children [415]. MRS employing nuclei other than hydrogen can provide complementary, potentially more specific information than ^{1}H, but is

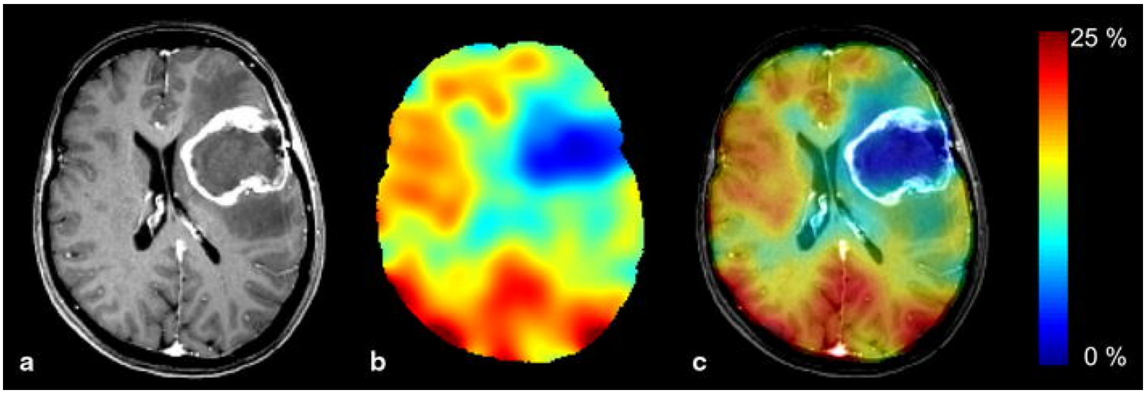

Fig. 18. (a) Anatomical ^{1}H image (T1-weighted MPRAGE) of a glioblastoma after contrast media administration with typical ring enhancement. (b) Parameter map of the relative ^{17}O signal increase in the corresponding slice after $^{17}O_2$ inhalation. (c) Colored overlay of the signal increase and the registered ^{1}H data for anatomical reference. The central necrotic region of the tumor coincides well with the area of lowest ^{17}O signal increase of <2%. The highest gain in intensity was found in regions with a high gray matter fraction. Reproduced from [402]. With permission of Springer.

generally hampered by its low sensitivity and the technical challenges that arise in the context of solving this issue, even at ultra-high field strength [416].

As described in Section 1.1.1, the SNR of small molecule resonances increases with field strength similar to water (protons), and this increase thus benefits most existing applications and may even render new applications feasible. However, SNR in ^{1}H MRS may be compromised by increasing linewidth in heterogeneous tissue voxels performed with commonly used sizes (1 cc or higher). As linewidth not only depends on field strength or resonance frequency but, strongly, also on spatial resolution and tissue heterogeneity (e.g., [417,418] for ^{1}H MRSI; 3 T vs. 1.5 T), improvements are to be expected at 7 T, e.g., in ^{1}H MRSI, if voxel size can be reduced to avoid line broadening. For ^{31}P MRS at 7 T, chemical-shift anisotropy helps to curb T_1 lengthening, and, thus, SNR increases more strongly than for dipole-dipole relaxation. Of course, T_2^* also gets shorter, but not so much as to blur spectral lines and in this way limit SNR. As always, various factors have to be optimized and balanced to obtain significant improvements at higher fields in vivo, and sequence parameters cannot just be linearly adapted.

At higher frequencies the spectral fingerprint of *J*-coupled metabolites may simplify because the splitting of lines into multiplets (governed by the scalar coupling constant, which is independent of B_0) becomes smaller compared to the frequency differences associated with the chemical shifts, which increase with field strength. This has typically two potential advantages: (1) SNR, defined as peak height vs. noise, may increase (if it is not reduced by increased linewidth/poor shim), and (2) spectra are easier to interpret and quantify (e.g., [419–421]). Both Tkáč et al. and Yang et al. showed that "In spite of the increased linewidth of singlet resonances at 7 T, the ability to resolve overlapping multiplets of *J*-coupled spin systems, such as glutamine and glutamate, was substantially increased" and "Characteristic spectral patterns of metabolites, e.g., myo-inositol and taurine, were discernible in the in-vivo spectra, which facilitated an unambiguous signal assignment", indicating a clear advantage driven by very high fields.

7.1.1. Non-^{1}H MRS

The challenges of non-proton ("heteronuclear" or "X-nucleus") nuclear magnetic resonance spectroscopy are illustrated here using the example of ^{13}C MRS. Carbon is a nucleus that is particularly useful because it is a constituent of almost every biochemically relevant molecule. The reason for the low sensitivity of MRS with ^{13}C is its low gyromagnetic ratio, which is approximately ¼ of that of ^{1}H, leading to an intrinsic NMR sensitivity of only 1.6% of ^{1}H; its low natural abundance, i.e., only 1.1% of all carbon atoms in human tissue are the NMR-sensitive isotope ^{13}C; and finally the low concentration of metabolites compared to tissue water.

To increase the signal in MRS, several strategies have been applied that are particularly effective in ^{13}C MRS, such as heteronuclear decoupling, whereby resonances that would otherwise be split up into several lines due to *J*-coupling are collapsed into a singlet resonance, which is advantageous due to an increase in SNR and a simplification of the spectrum [422]. Further techniques include polarization transfer for enhancing the ^{13}C magnetization, indirect ^{1}H-[^{13}C] detection, ^{13}C labeling, and hyperpolarization of administered substances [422]. Some of the techniques, like nuclear Overhauser effect (NOE), decoupling, and polarization transfer are also applicable to other X-nuclei like ^{31}P or ^{19}F, and their use may be advantageous depending on the field of application.

With direct detection of ^{13}C MRS, it is possible to obtain highly specific information on metabolite concentrations and their reaction rates [423]. ^{13}C enrichment of metabolic precursors [424–426] not only enhances the signal, it also offers the possibility to trace metabolic pathways [427,428]. The large dispersion of the ^{13}C NMR spectrum helps to identify the various resonances but poses challenges for the detection of such broad spectra, and the high field also poses challenges for heteronuclear broadband decoupling of multiplet resonances [429].

Heteronuclear decoupling in MRS is extremely challenging in terms of RF hardware requirements, particularly because of the electromagnetic interaction between the coil elements. While one channel is used to transmit RF power, the other is used to detect the NMR signal which is several magnitudes smaller than the transmitted RF. This separation of channels (also termed coil decoupling) therefore has to be on the order of 100 dB, and it has to be effective across the entire length of the RF transmit and receive chain. This requirement becomes a severe challenge for in-vivo applications in humans at very high field, where the high power required to excite B_1 fields for decoupling in large regions is counterweighted by SAR restrictions and by artifacts (typically spikes in the received signal) that can be caused by such high-power decoupling RF. Where geometrical separation is impossible, efficient filters with appropriate pass-band and stop-band characteristics and blocking circuits in the coil elements have to be employed. It has been shown recently that heteronuclear ^{1}H decoupling of ^{13}C spectra is possible in humans in vivo at 7 T [430] with a coil that has been optimized for high SNR by implementing a double-quadrature loop design and employing efficient blocking circuits within the coil [431].

A valid approach to reduce SAR by avoiding adiabatic RF pulses for localization with surface coils is to use whole-body transmit coils for X-nucleus MRS, envisaging applications in the torso,

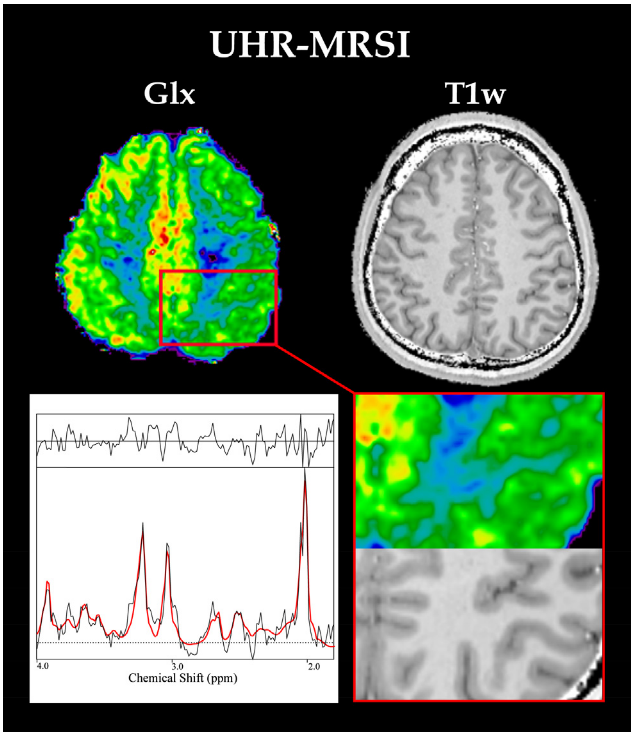

Fig. 19. Combined glutamate + glutamine (Glx) map along with a T_1-weighted (T1w) MR image and sample spectrum from white matter in the occipital lobe acquired with an ultra-high-resolution (UHR) 7 T MRSI sequence (42 min FID MRSI, 128 × 128 matrix, TR = 200 ms, acquisition delay 1.3 ms, and resolution 1.7 × 1.7 × 10 mm^3). A zoom-in of the Glx map highlights the visibility of the GM/WM contrast. The colors from cold to warm indicate higher relative concentrations. Regarding the sample spectrum, black is the measured spectrum and red the spectral LCModel fit. The spectrum was first-order phased for display purposes only. Adapted from [444].

particularly for the liver and heart [291]. In the case of ^{31}P, the advantage is that its resonance frequency at 7 T nearly coincides with the ^{1}H resonance frequency at 3 T, and existing coil concepts and transmit hardware can be easily adapted, necessitating only minor retuning.

7.2. Applications

The advent of high-field and, particularly, UHF MR magnets [24,416] has provided an impetus to develop and optimize novel techniques to enable fast and, specifically, localized MRS and MRSI of the human brain, liver, and skeletal muscle [432]. In the following, advances in fast ^{1}H MRSI in the brain, ^{1}H, ^{13}C or ^{31}P MRS in liver and heart, and dynamic ^{31}P MRS in skeletal muscle are discussed (e.g., [279,407,433–439]). Except for skeletal muscle, which can be stimulated mechanically in the magnet, important challenges to be met are stimulation of the target organ pharmaceutically or else study of dynamic aspects of organ metabolism in well-designed (longitudinal) clinical studies. Disadvantages in a routine clinical setting may include the complexity of the MRS investigation, requiring a dedicated, non-commercial setup, expertise in cross-checking the data quality during the experiment, and establishment of the data processing pipeline and interpretation of the results.

7.2.1. Brain metabolism

Due to the higher sensitivity of protons, and combined with UHF magnets and multi-channel phased-array coils, the sensitivity of ^{1}H spectroscopic imaging has been recently improved [410]. Still limited by low B_0 and B_1^+ homogeneity, low resolution, long measurement times, and SAR restrictions, ultra-high-resolution MRSI sequences have been developed to overcome these limitations [262,410,440–442]. Within a clinically feasible examination time of approximately 15 min, a spatial resolution of $1.7 \times 1.7 \times 8\ \text{mm}^3$ can be achieved with the use of a short TR (200 ms), sampling an optimized FID with shortened water suppression, and parallel imaging acquisition (CAIPIRINHA).

Transversal pulse-cascaded Hadamard encoding [443] has been employed to extend the brain coverage to 4 slices (acquisition matrix = $100 \times 100 \times 4$), which is also not limited to rectangular ROIs in the center of the brain [444]. Metabolic maps obtained (tNAA, tCR, tCho, Glx, Ins) show high spatial resolution fitting to the brain's cortical folding on T1-weighted images, i.e., GM vs. WM contrast (Fig. 19), while quantification accuracy has been significantly improved by the ability of UHF MRS to identify macromolecule resonances [445,446]. Similar work based on phase-encoded MRSI and echo-planar spectroscopic imaging (EPSI) has been presented [447,448]. Higher-order B_0 shimming [259], dynamic shims [104,449], or B_1^+ shimming with pTx systems [105,449] can further improve data quality and reliability. Data reliability may also improve with the use of real-time motion correction (cf. Section 4). Clinical areas of interest include Alzheimer's disease, Parkinson's disease, multiple sclerosis [450,451], epilepsy, brain injury, and brain tumor staging and follow-up.

For ^{13}C MRS with labeled precursors, quantification of the resolved carbon resonances of glutamate and glutamine has been

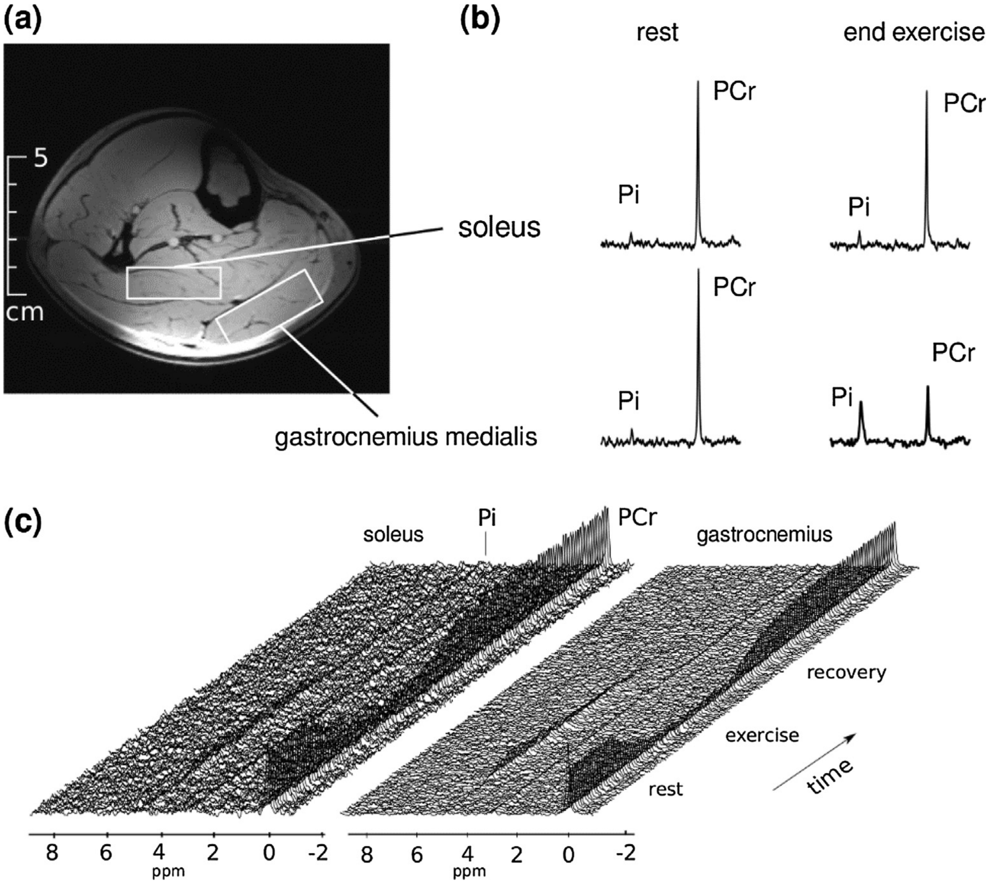

Fig. 20. Transversal gradient-echo image of the calf muscles of a healthy subject, shown with the voxels selected for localized ^{31}P MRS (a). Time-resolved MR spectra were acquired continuously with 6 s temporal resolution at rest, during voluntary plantar flexion exercise, and during recovery. Spectra acquired before and after muscle exercise show that phosphocreatine (PCr) depletion and accumulation of inorganic phosphate (Pi) is predominantly observed in the gastrocnemius muscle; full time series are shown in (c). (a) and (b) adapted from [435].

achieved in the brain [452,453]. Furthermore, tissue glycogen [51,423,454–456] and glucose content [457] have been measured.

7.2.2. Liver metabolism

When applied to the liver, MRS can serve as a valuable tool to study metabolism in healthy subjects and patients with various diseases. Even at lower field strength, ^{1}H MRS enables estimation of lipid content in healthy livers, non-alcoholic fatty liver (NAFL), and hepatitis C [458]. Hepatocellular lipid concentration is linked to liver glycogen storage, endogenous glucose production, and finally to insulin resistance [459].

^{13}C MRS gives access to the measurement of glucose production and glycogen storage, allowing studies of hepatic glycogenolysis and gluconeogenesis [455] and, using labeled precursors, the quantification of hepatic mitochondrial fluxes [460].

With ^{31}P MRS, reduced ATP and inorganic phosphate content were found in the liver of type 2 diabetic individuals [461], associated with reduced phosphorylation fluxes as shown by ^{31}P saturation transfer methods [462]. At ultra-high field strength, higher resolution and increased reliability were shown to be achievable with ^{31}P chemical shift imaging (CSI), and resonances that were previously not detectable could be quantified: uridine diphosphate glucose and phosphatidylcholine (PtdC), a component of the bile [463]. Due to its position, the liver can be examined using surface coils, yet localization of the signal is important to avoid contamination of the signal from muscle and other tissue. Localization schemes that have been successfully used to study liver tissue with ^{31}P MRS are imaging-selected in-vivo spectroscopy (ISIS) in 1 and 3 dimensions [462,464] and 2- and 3-dimensional CSI [465] and combinations thereof [466].

7.2.3. Skeletal muscle metabolism

Ultra-high field ^{31}P MRS is particularly useful for studying muscle metabolism [439,467], as the increasing field strength does not introduce any significant adverse effects related to SAR or due to obligatory fat/water suppression, typical challenges in proton MRI at 7 T [24,468]. The ^{31}P resonance frequency at 7 T is only about 120 MHz. Even better, due to increasing contributions from chemical shift anisotropy, ^{31}P T1 relaxation times decrease above about 3 T [469,470], allowing higher scanning efficiency at shorter TRs. Thus, as suggested previously [468,471], ^{31}P MRS is the perfect candidate for UHF MRS at 7 T and higher, as the decreasing relaxation times help increase sensitivity without the adverse effects mentioned above, enabling both improved specificity and sufficient sensitivity.

Therefore, there has been a focus on localized, dynamic ^{31}P MRS in skeletal muscle for several years, with development of methods and applications to profit from the availability of the increasing field strength [435,439,470,472–477] (Fig. 20). Advances in technology have permitted moving from non-localized dynamic acquisitions using simple planar loop coils, or spatially-resolved static

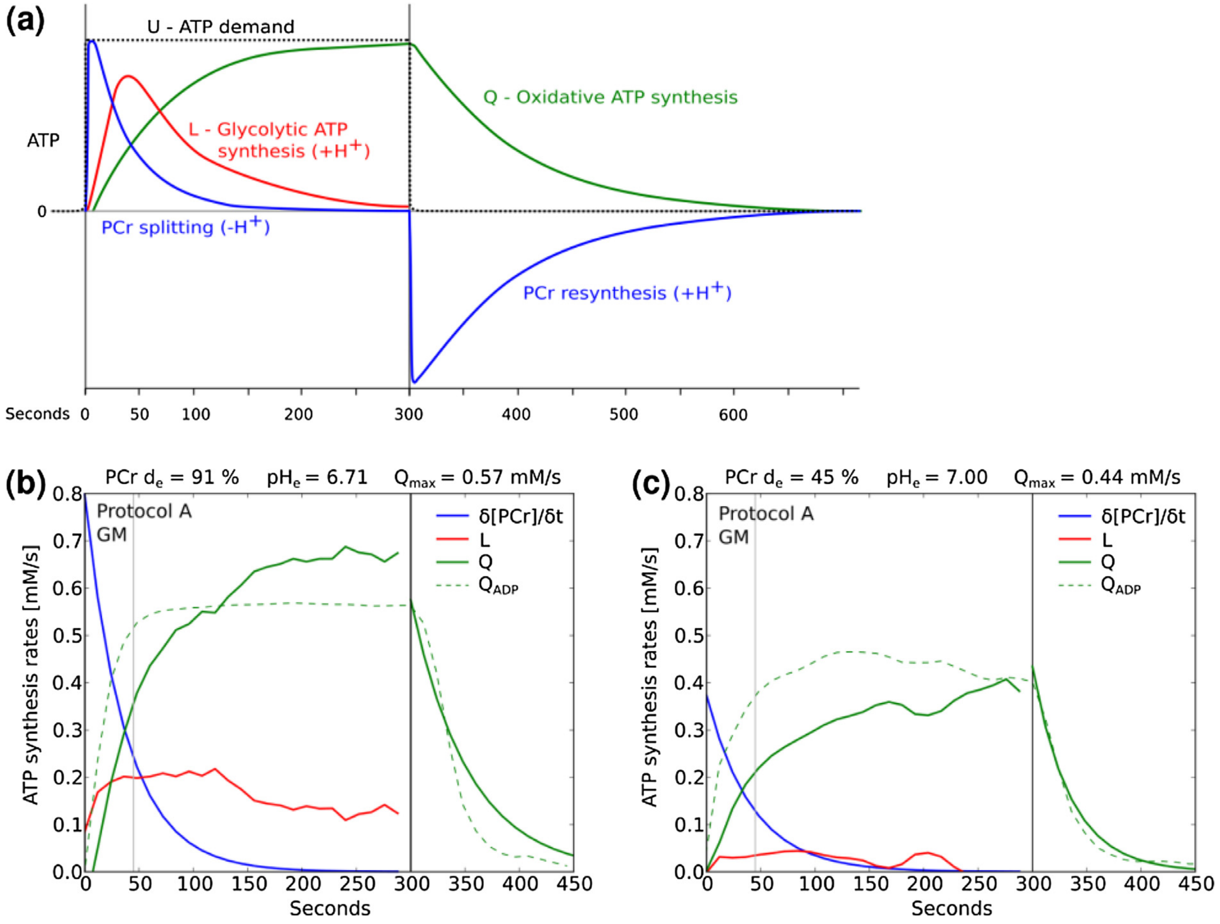

Fig. 21. Contributions to ATP synthesis in skeletal muscle during exercise and recovery, illustrated schematically (a): ATP demand (U), assumed to be constant during exercise with constant intensity, is matched by ATP generation via breakdown of phosphocreatine (PCr, blue) which is associated with proton comsumption, glycolysis (L, red) and oxidative phosphorylation (Q, green). During recovery, replenishment of ATP stores is achieved by purely oxidative phosphorylation and is reflected by PCr resynthesis. Modeling of L and Q from metabolite concentrations obtained directly from in-vivo ^{31}P MRS measurements (b, c) involves the temporal derivative of input data and hence requires high temporal resolution and measurement stability. Data shown were acquired from the medial gastrocnemius muscle of a single human subject exercising at high (b) and medium (c) intensity. Figure adapted from [435].

measurements, to a combination of high temporal resolution with excellent spatial localization.

Interleaved and simultaneous acquisition of ^{31}P with ^{1}H MRS and (functional) MRI data has become possible on clinical MRI scanners [303]. Here we provide an overview of essential requirements in terms of hardware and MR sequences for investigating skeletal muscle, as ^{31}P MRS yields information about tissue metabolism in vivo that is hard to obtain otherwise [467]:

a) To provide sufficient sensitivity, a 7 T magnet or higher is beneficial. This results in a SNR gain of about 2.5 (7 T vs. 3 T).
b) To further increase sensitivity, dedicated RF coils, anatomically fitted to the body part of interest, are also required (e.g., [475]). For example, in the gastrocnemius muscle another SNR increase of about 2.5 is possible; however, gains are achievable across the entire calf muscle.
c) To increase specificity, localized single or multi-voxel MRS with high temporal resolution (<10 s) [435,473,478,479] or MRSI [480] may be carried out. Due to the increased number of data points, it is possible to detect small and fast PCr and pH changes during the initial exercise period (ca. 30 s) [435], separating the aerobic and anaerobic regimes (Fig. 21).
d) To increase information content while keeping the overall measurement time constant, interleaved data acquisition [303,472] combining metabolic information with functional information, e.g., ASL or T2* mapping, may be used [481]. This feature renders the complex physiological experiment more robust and enables a more comprehensive description of various aspects of muscle physiology.

Depending on the data collected, however, dedicated data processing pipelines and (complex) models need to be used [435,467].

Time-resolved imaging has also been shown to be feasible with ^{31}P in skeletal muscle at 7 T, and has been used to quantify metabolite concentrations [482] and fluxes [482] or pH [477]. Furthermore, spiral spectroscopic imaging has been shown to be feasible with sufficient temporal resolution [480].

Glycogen and glucose have previously been quantified by ^{13}C MRS in skeletal muscle at lower field strengths [457,483–486], and the technique has been successfully transferred to 7 T scanners [430].

7.2.4. Cardiac metabolism

The primary sources of chemical energy for the heart are free fatty acids (FFA) and glucose, and oxidative phosphorylation is the basis for providing energy via the mitochondrial respiratory chain. Energy is buffered via the creatine kinase system to hold ATP concentrations constant [487]. Hence, ^{1}H and non-proton MRS approaches are well suited to study cardiac metabolism and have great potential for a large range of clinical applications. Creatine and triglyceride content are accessible with ^{1}H MRS [488], high-energy metabolites can be measured with ^{31}P MRS [279,489], and ^{13}C MRS can be used to target labeled or hyperpolarized pyruvate and bicarbonate [426,490].

The challenges in cardiac applications are breathing and heartbeat-related motion, spatial resolution and localization, and sensitivity. Mitigation strategies for motion comprise triggering and (MRI-based) motion compensation approaches (cf. Section 4). The sensitivity challenge can be addressed with the increased SNR at 7 T [279,489], but heterogeneity of B_1 and limited penetration depth in the torso become major problems, which are currently being investigated using parallel transmission RF coil technology (cf. Section 3), offering static or dynamic B_1 shimming capability, and by employing whole-body coils for X-nucleus MRS [291].

8. CEST imaging

8.1. Technical aspects

Chemical exchange saturation transfer (CEST) allows for indirect detection of diluted molecules that contain exchangeable protons via transfer of their saturated proton magnetization to the abundant water pool [491–493]. The typical CEST sequence consists of a selective RF pre-saturation block and a subsequent fast readout of the modulated bulk water signal via MR imaging. Due to accumulation of saturation in the water pool, CEST effects are more sensitive compared to direct signal detection of the molecules themselves, by a factor on the order of the exchange rate of the process. Fig. 22 shows a typical single-shot CEST sequence (a) together with a scheme of the magnetization time course (b) during saturation either at an offset $\Delta\omega = \delta\omega_s$ (s for solute) that corresponds to a CEST resonance (red dashed line) or alternatively at a reference frequency offset $\Delta\omega = \delta\omega_{ref}$ where there is no CEST resonance (black solid line). During saturation at $\Delta\omega = \delta\omega_{ref}$ (black solid line), there is no CEST pool present and the magnetization decays to the value $M_{sat}(\delta\omega_{ref})$, which is then measured using a fast imaging readout. In contrast, if a CEST pool is present during saturation at $\Delta\omega = \delta\omega_s$ and is in exchange with the water pool, as depicted by the pool model in Fig. 22c, the magnetization decays more strongly during the saturation pulse phase (red dashed line) to a lower value $M_{sat}(\delta\omega_s)$. With these two offsets and an additional scan to measure the thermal equilibrium water magnetization M_0, the CEST signal can be defined by

$$CEST = \frac{M_{sat}(\delta\omega_{ref}) - M_{sat}(\delta\omega_s)}{M_0} \tag{8}$$

The ideal CEST effect is given by [494]

$$CEST = \frac{k_{ws} \cdot \alpha}{k_{ws} \cdot \alpha + R_{1w}} \cdot \left(1 - e^{-(R_{1w} + k_{ws} \cdot \alpha) \cdot t_{sat}}\right) \tag{9}$$

which reveals an exponential buildup during the saturation time. The size of the CEST effect is governed by the water-to-solute exchange rate k_{ws}, by the water relaxation rate R_{1w}, but also by the so-called labeling efficiency α given by

$$\alpha(\Delta\omega, \omega_1) = \frac{\omega_1^2}{\omega_1^2 + k_{ws}^2 + (\Delta\omega - \delta\omega_s)^2} \tag{10}$$

$\alpha(\Delta\omega, \omega_1)$ is a measure of how strongly a CEST pool is saturated. It has a Lorentzian offset dependence and, for a specific exchange rate, its amplitude depends on the saturation pulse amplitude $\omega_1 = \gamma \cdot B_1$, and its width decreases with increasing frequency shift $\delta\omega_s \propto B_0$ and therefore depends on the static field B_0. Thus, theoretically it can be seen that high B_0 and B_1 homogeneity as well as high B_0 field strengths can help selective CEST experiments. It should also be pointed out that with typical RF amplifiers in human MRI systems, only pulsed saturation can be realized, lowering the effective labeling by approximately the RF duty cycle.

While Eq. (8) in principle allows calculation of a CEST effect, typically more than two offsets are measured to allow for B_0 inhomogeneity artifacts and also the possibility that there may be several apparent CEST pools. The sequence block in Fig. 22a is repeated for a whole set of offsets between −5 ppm and 5 ppm to generate a so called Z-spectrum $Z(\Delta\omega) = \frac{M_{sat}(\Delta\omega)}{M_0}$ for each voxel. The spectrum reveals several CEST effects in brain matter as depicted in Fig. 22d. CEST effects are rather small and in the range of a few percent of the water signal; thus, higher static fields strengths that provide a sizeable SNR gain [25] are especially beneficial when detecting small CEST effects. Based on the peak separation given by the individual chemical shifts, several different

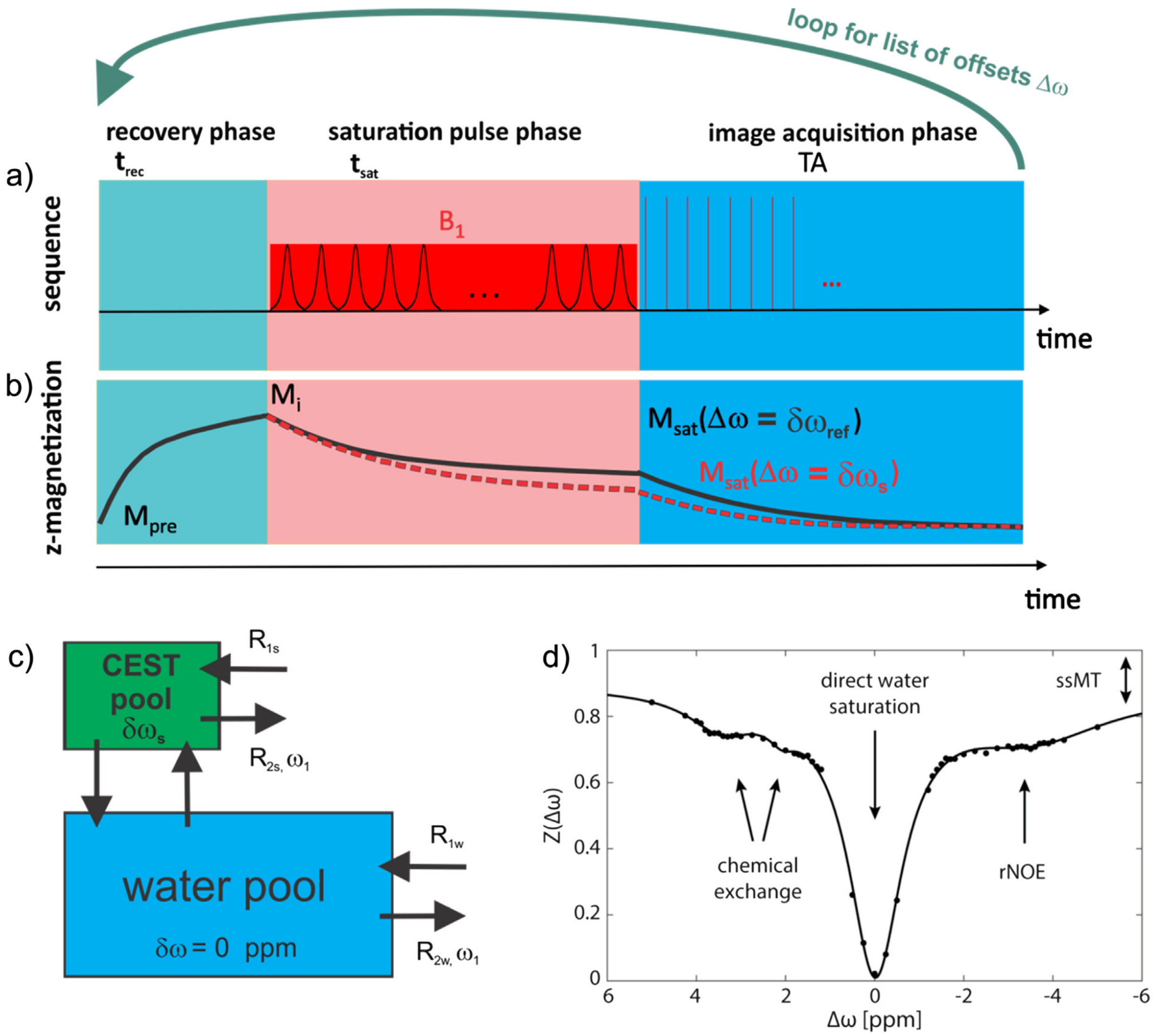

Fig. 22. (a) RF pulse sequence scheme of a typical CEST sequence: t_{rec} = recovery time, t_{sat} = saturation time, TA = acquisition time. (b) z-magnetization behavior for reference scan (black solid line) and CEST scan (red dashed line). (c) pool model of solute CEST pool s in exchange with the abundant water pool w. (d) example of an in-vivo Z-spectrum of human brain tissue at 7 T; rNOE = relayed nuclear Overhauser effect, ssMT = semi-solid magnetization transfer.

diluted solutes have been reported to be detectable using CEST, including peptides and proteins [493,495–498] exchanging via amides (3.5 ppm) and NOEs (−3.5 ppm), creatine [499,500] via its guanidyl-group (2 ppm), glutamate [501,502] (3 ppm), as well as injected solutes such as iopamidol [503–505], glucose [506–509], and glucose derivatives [510,511]. As the chemical shift separation (in Hz) increases with the static field strength, not only is the separation of CEST peaks easier at UHF, but also the strength of the effect can be increased, as demonstrated for amide, amine, and NOE CEST effects [512], for hydroxyl protons close to the water peak, e.g. in glycosaminoglycans in cartilage [513], as well as for the exogenous agent iopamidol [514].

Fig. 23 shows a comparison of CEST effects in the human brain at 3 T [515], 7 T [498], and 9.4 T [516]. While CEST effects are detectable at 3 T and show hyperintensities in the tumor regions (Fig. 23a–c), the CEST spectra show relatively broad peaks around +3.5 ppm and −3.5 ppm. At 7 T the effects are more clearly separated as seen in Fig. 23d, where now the 3.5 ppm and 2 ppm resonances become distinguishable (see also [495,517,518]). Also, the amide and NOE signals outline the tumor region (Fig. 23e and f) and in addition a 2 ppm CEST map can be created (Fig. 23g). Going to the higher field strength of 9.4 T, this differentiation is further improved; the effects become stronger and peak separation improves (Fig. 23h), which directly translates to smoother CEST maps compared to 7 T in Fig. 23i–k. This increase in CEST effect strengths with B_0 is not generally valid; if selectivity is not the primary issue, the same saturation pulse can actually saturate adjacent species within the pulse bandwidth simultaneously, leading to a stronger net CEST effect at lower fields (see, for example, van Zijl et al. [519] and Zaiss et al. [497]).

An application where UHF strongly increases the contrast is glycosaminoglycan CEST (gagCEST) in cartilage: as the hydroxyls protons resonate close to water, a pronounced direct saturation effect at 3 T is induced and thus CEST effects are diluted (Fig. 24a–c). Experimentally, only a small gagCEST effect could be measured at 3 T (Fig. 24c): with optimized parameters about 1.3% has since been reported at 3 T [520]. At 7 T an effect of more than 5% was reported (Fig. 24d). Fig. 24 depicts another important challenge at UHF: the influence of the B_0 inhomogeneity on the Z-spectra and especially on quantification based on asymmetry analysis. A very small change in B_0 (>0.1 ppm) due to inhomogeneity can lead to severe over- or underestimations of CEST effects

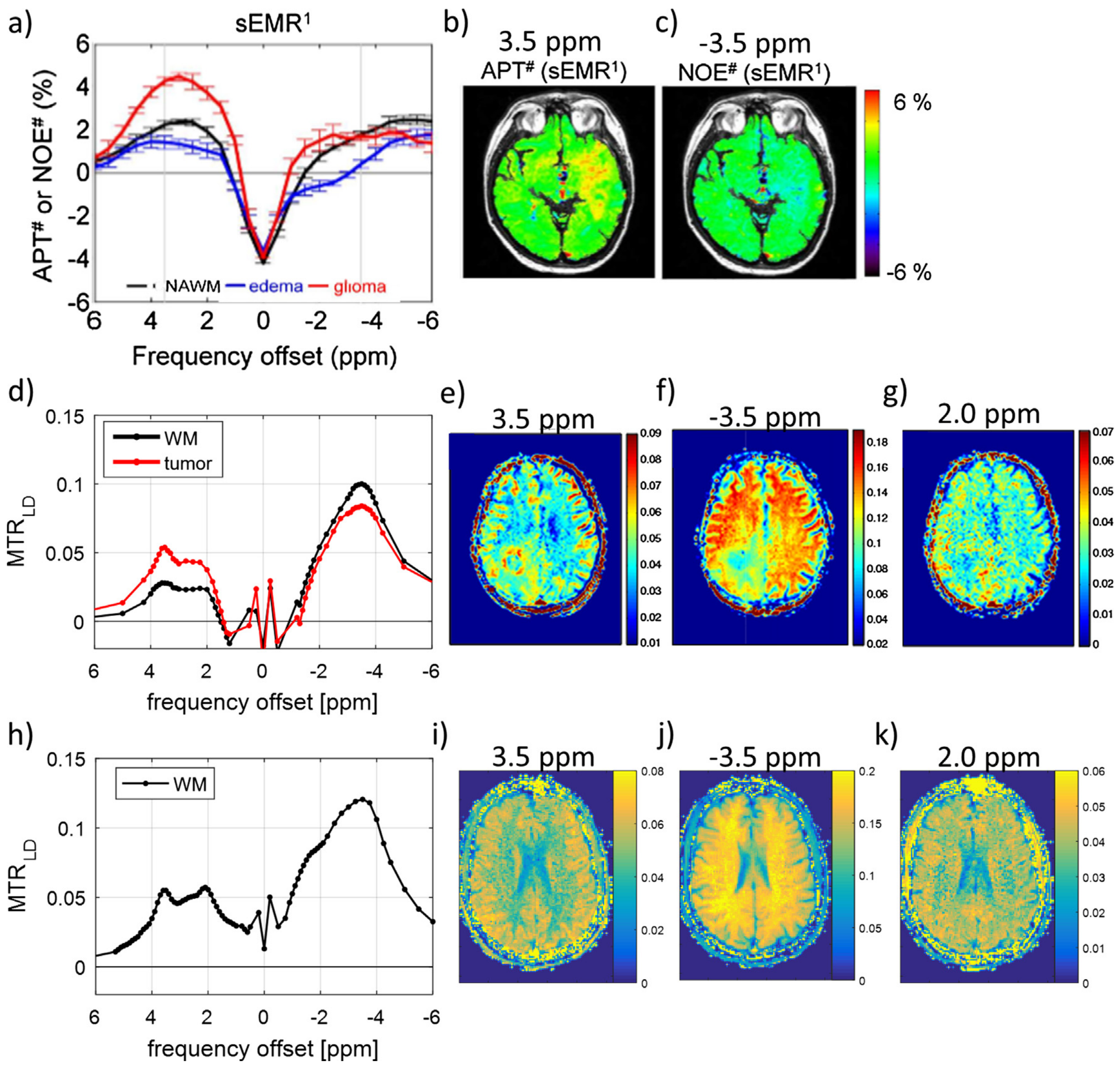

Fig. 23. CEST effects at B_0 = 3 T (a-c) from Heo et al. [515], CEST at B_0 = 7 T (d-g) from Zaiss et al. [498], and CEST at B_0 = 9.4 T (h-k) from Zaiss et al. [516]. All CEST effects were isolated by removal of water saturation and semi-solid MT background. (d) and (h) show the CEST signals in the MTR_{LD} metric, where MTR_{LD} stands for magnetization transfer ratio using the Lorentzian difference method. This is equivalent to Eq. (8) but uses a Lorentzian background fit for the reference signal. (a) uses the similar $NOE^{\#}$ and $APT^{\#}$ metrics, where $NOE^{\#}$ and $APT^{\#}$ are the CEST effects evaluated using the sEMR (symmetric Extrapolated Semisolid Magnetization Transfer Reference) as reference scan in Eq. (8) instead of a Lorentzian as in MTR_{LD}. (b-c and e-g) show CEST maps of glioma patients, whereas (i-k) show CEST maps of a healthy volunteer.

in vivo (https://onlinelibrary.wiley.com/doi/abs/10.1002/mrm.27367). With the stronger B_0 inhomogeneities at UHF, this is even more important to correct for.

8.1.1. B_1 dependency and B_1 correction

CEST effects strongly depend on the B_1 saturation amplitude and the saturation duration t_{sat} in close relation with the exchange rate (Eq. (10). This has the benefit that different exchange regimes can be addressed with different saturation schemes: low power and long saturation selects slow exchange such as protein signals of amide protons via exchange and aliphatic protons via exchange-relayed NOEs; higher power but short saturation selects faster exchanging pools such as amine protons of creatine and glutamate, or even hydroxyl protons of glucose and derivatives. At UHF however, the strong B_1 dependence is a major drawback for CEST, as B_1 inhomogeneities directly compromise the CEST effect. Fig. 25a shows results for CEST effects at 7 T with strong correlation to the acquired B_1 map [521]. Especially for imaging of pathologies, this B_1 artifact is a severe disadvantage, as hypointensities can be misinterpreted (Fig. 25a and b). This is an ongoing challenge for UHF CEST, but several solutions have been proposed: Singh et al. showed that using roughly sampled calibration values, CEST maps can be corrected in post-processing [522]. Windschuh et al. showed more generally that with two or more CEST scans at different B_1 powers, B_1 artifacts in the brain can be corrected to a large extent [521] (Fig. 25c and d).

While the latter approach is very general, the scan time is at least doubled. Also, correcting for the B_1 inhomogeneity during post-processing is straightforward, but not very elegant. Mitigating B_1 inhomogeneities during saturation using parallel transmission techniques is one of the latest important developments for increasing robustness in UHF CEST imaging. In recent work by Tse et al., it could be shown that convoluting spokes RF pulses with Gaussian CEST saturation pulses [523] significantly reduces the saturation inhomogeneity across the brain. Parallel transmission is therefore feasible for generating CEST contrast at UHF that is largely independent of B_1 inhomogeneities and is currently the most promising and elegant approach for robust and fast application of CEST at UHF, especially in body imaging.

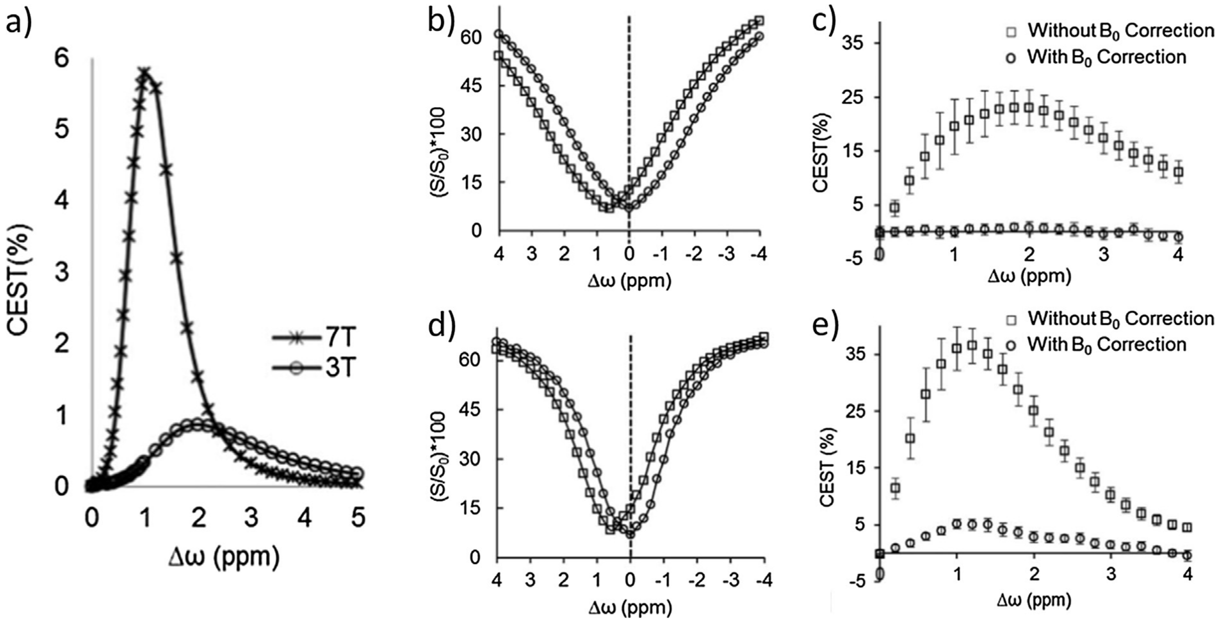

Fig. 24. (a) gagCEST asymmetry plot simulations at 3 T and 7 T. Z-spectra (b and c) and plots of CEST asymmetry (d and e) of human knee cartilage without (squares) and with (circles) B_0 correction obtained at 3 T (b and c) and 7 T (d and e). Saturation pulse parameters were B_{1rms} of 2.2 μT and duration of 0.5 s. Adapted from [513].

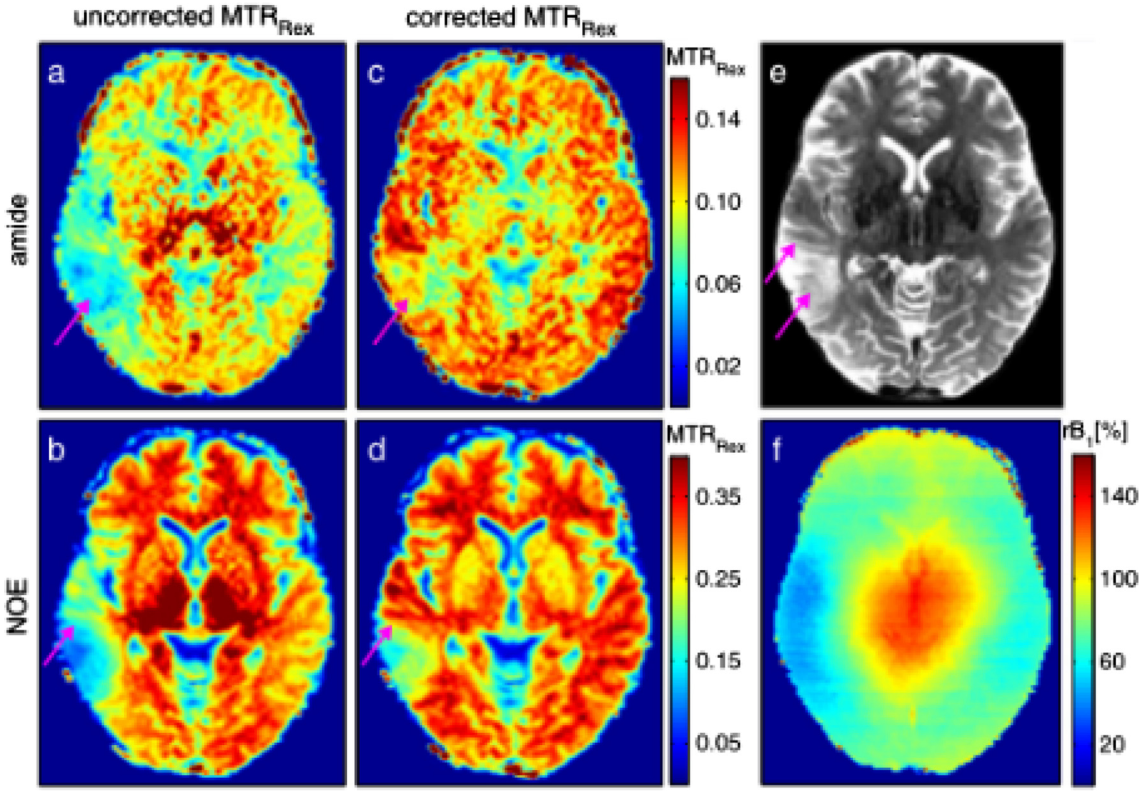

Fig. 25. Application of an optimized B_1 correction method to CEST images of a patient with oligodendroglioma WHO grade 2. Uncorrected CEST images based on MTR_{Rex} with nominal B_1 = 0.9 μT (a, b) and 2-point B_1-corrected CEST images based on MTR_{Rex} at B_1 = 0.8 μT (c, d) for amides (δ_{amide} = 3.5 ppm) (a, c) and aliphatic NOE (δ_{NOE} = −3.5 ppm) (b, d). T_2-weighted image (e) and B_1 field map (f) of the same patient. The pink arrows indicate regions of altered contrast due to B_1 correction. Reproduced with permission from [521]. MTR_{Rex} is the T2- and MT-corrected magnetization transfer ratio defined by $MTR_{Rex} = \frac{M_0}{M_{sat}(\delta\omega_s)} - \frac{M_0}{M_{sat}(\delta\omega_{ref})}$, which is the inverse difference when compared to Eq. (8).

8.2. Applications

While the preceding examples have shown that CEST at UHF has its benefits, many CEST applications are already employed successfully at 3 T. For example, amide proton transfer-weighted imaging utilizing protons resonating 3.5 ppm downfield from water, i.e. relatively far away from water, has been shown to yield insights into brain tumors at 3 T, such as differentiation of radiation necrosis and progression of brain metastases [524], histopathological grading of gliomas [525], prediction of isocitrate dehydrogenase (IDH) mutation status [526], and assessment of O^6-methylguanine-DNA methyltransferase (MGMT) status [527]. In addition, amine CEST effects (~3 ppm) were shown to yield strong contrast between healthy tissue and tumor in vivo [528] and were claimed to also provide in-vivo pH mapping. The principal pH dependency of amide [493] and amine CEST effects also makes it interesting for application in stroke where first findings were reported at 3 T [529–531]. Thus, CEST at 3 T is feasible and already provides many interesting insights; moreover, several of the problems mentioned for CEST at UHF such as B_0 or B_1 inhomogeneities are less severe at 3 T, including RF amplifier and SAR restrictions that often limit the power range at UHF.

Nevertheless, UHF protein CEST effects can enable deeper insights into brain tumors (Fig. 23). Jones et al. showed that NOE CEST effects at 7 T are decreased in the tumor area and correlate with the macromolecular background [495]. Isolated amide CEST effects at 7 T nicely reflect regions of contrast agent uptake [497]. In principle, selective protein CEST effect strengths also correlate with protein conformation such as folding or aggregation processes, which might be potentially interesting for neurodegenerative diseases with protein alterations [532–534]. Closer to water, the resonance at 2 ppm, first resolved at 7 T, shows promising correlations with creatine and thus energy metabolism [499,535–537], but also potentially access to pH with enhanced sensitivity by taking ratios of different isolated CEST peaks [532–534]. Going even closer to the water resonance, e.g. as in the case of hydroxyl CEST, is very difficult at 3 T. At 7 T, gagCEST allowed detection of similar contrast compared to ^{23}Na MRI between healthy and repair tissue in knee cartilage [538]. As a further example, the glucose CEST (glucoCEST) experiment and dynamic glucose-enhanced (DGE) imaging, where administered glucose is detected via CEST, have until now been demonstrated in humans only at 7 T [507,509,539]. Fig. 26 shows results of DGE imaging of a brain tumor: the hydroxyl-exchange-weighted signal is acquired before, during, and after injection, and the relative signal change can be made visible as a DGE image that displays glucose uptake in the tumor area [540] (Fig. 26c).

In summary, the expected selectivity and signal gain for CEST at UHF has been experimentally verified and provides a deeper understanding of CEST effects. The larger frequency separation from the water proton resonance is especially beneficial for CEST resonances closer to water like amine, guanidyl, or hydroxyl groups, which often cannot be resolved at 3 T with sufficient SNR. The insights gained at UHF can be used to further understand observable CEST effects at 3 T, which have already showed potential clinical relevance.

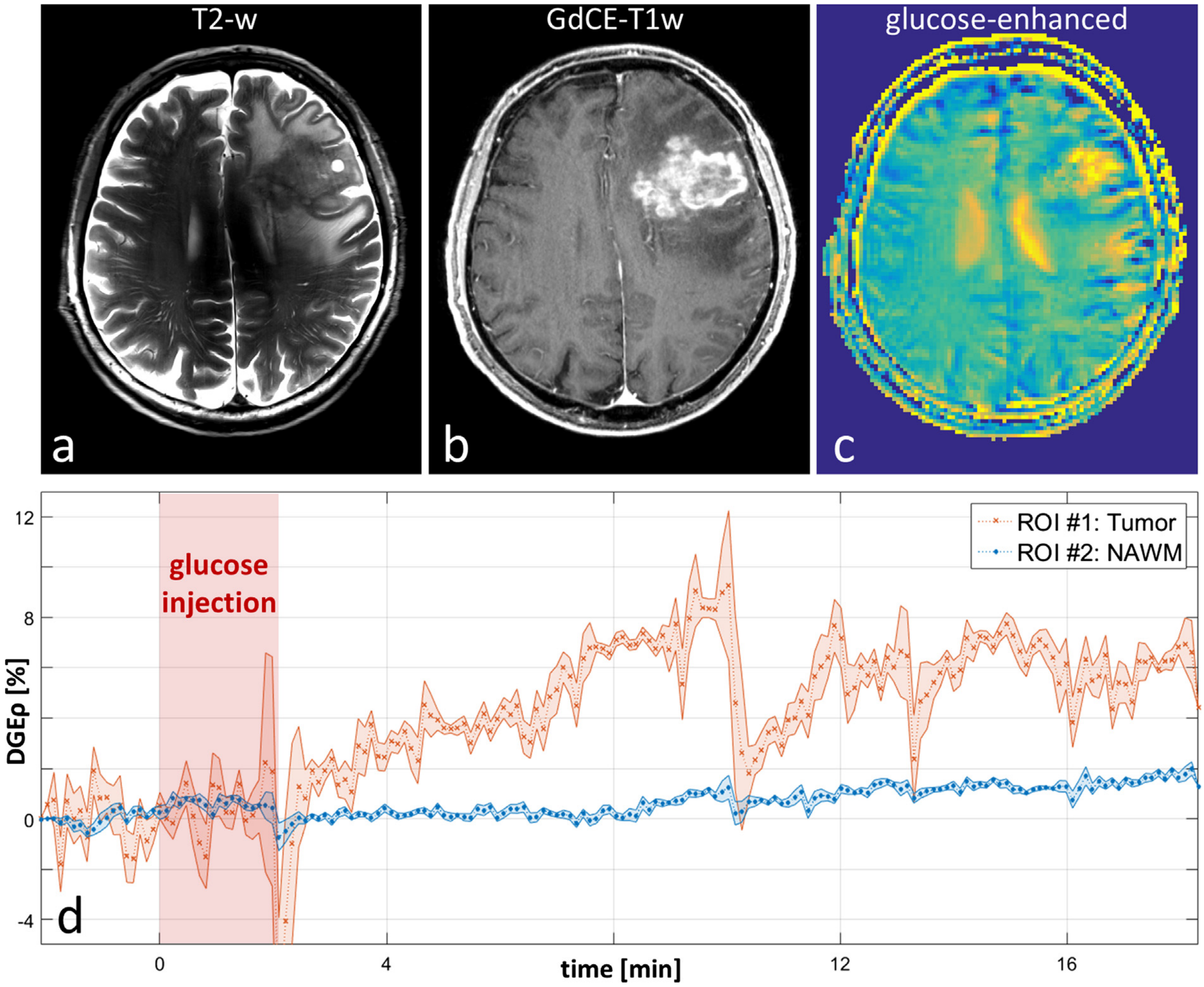

Fig. 26. (a) T2-weighted image acquired at 7 T, (b) gadolinium-enhanced T1-weighted (GdCE-T1w) image acquired at 3 T, and (c) T1ρ-weighted dynamic glucose enhancement (DGEρ) obtained at t = 588 s at 7 T. (d) Unsmoothed DGEρ time curves with a temporal resolution of better than 7 s in a tumor ROI (ROI #1) and a ROI in normal appearing white matter (ROI #2). The signal drop at t ~ 10 min is attributed to subject motion. Reproduced from [540] under the license https://creativecommons.org/licenses/by/4.0/.

9. fMRI

9.1. Technical aspects

Functional MRI (fMRI) using blood-oxygenation-level-depen dent (BOLD) measurement of brain activation was probably the single most important application in the initial drive to develop UHF systems of 7 T and above [541]. The motivation for this was the expectation of both a supralinear increase in BOLD sensitivity with static magnetic field strength [31] and an improved intrinsic spatial localization [542]. This section will hence first deal with the underlying biophysics of BOLD contrast, followed by a discussion on measurement methods, and conclude with an overview of some applications of fMRI that are specific to ultra-high field.

BOLD biophysics as developed during the 1990s showed that there are four main BOLD contrast mechanisms, *viz:* extravascular static dephasing, extravascular dynamic dephasing, intravascular changes in T2, and the dephasing of intravascular signal from multiple vessels within a voxel caused by variations in deoxyhemoglobin concentration and/or differences in vessel orientation with respect to that of the static magnetic field (reviewed in [543]). As a rough generalization, the importance of the intravascular contrast mechanisms is expected to diminish with increasing static magnetic field strength because of the dramatic reduction in venous T2. Extravascular dynamic dephasing (also known as dynamic averaging) arises from diffusive motion about small vessels and is predicted to increase quadratically with field strength, whereas static dephasing should have a linear dependence. As the smaller vessels lie in the capillary bed, they should be closer to the underlying neuronal activity. Hence, spatial resolution in general is expected to improve, and that of spin-echo fMRI in particular [542,544], as this technique will not record static dephasing mechanisms, and at longer TEs, matched to the expected T2 of gray matter, the intravenous contribution can be expected to have decayed away.

Another important consideration when considering this spatial resolution is the contribution of so-called physiological noise to the BOLD signal [545]. As the name implies, physiological noise arises from the person being measured, and may be further subdivided into non-BOLD physiological noise, primarily arising from cardiac activity and respiration, and BOLD noise that is made up of the same random fluctuations in the BOLD signal that are utilized in resting-state fMRI. Of course the non-BOLD physiological noise is not really true noise but varies systematically due to the underlying physiological fluctuation. Furthermore, the amplitude of this noise will be directly proportional to the signal intensity, with the unfortunate consequence that if this is the dominant noise source, then increasing the signal intensity will not increase the BOLD sensitivity as both signal and noise will scale in the same way [545]. It is hence recommended that for fMRI acquisitions at 7 T and above, the voxel volume be sufficiently small such that thermal rather than physiological noise should dominate [546–548].

As discussed elsewhere in this article (cf. Sections 1 and 3) the move to UHF brings with it a number of challenges. The most germane of these with regard to fMRI are: the poorer static magnetic field homogeneity reduces the quality of EPI images, the poorer B_1 homogeneity leads to flip angle variation, and the increased power deposition can constrain some acquisitions. The current standard coil configuration is a 32-channel head coil that works well for the neocortex. Without pTx (cf. Section 3) there is considerable variation in the B_1 homogeneity throughout the brain, with spin-echo sequences being particularly badly affected. These inhomogeneities become more pronounced in the brain stem and cerebellum.

Parallel imaging techniques may now be considered standard for all fMRI acquisition at 7 T. This includes both in-plane acceleration [315,549,550] and simultaneous multi-slice (SMS) techniques [86,87,551,552]. The consequences of using these two forms of acceleration on fMRI differ. Given the near ubiquitous nature of the EPI readout, only the effect on this is considered. In-plane acceleration will reduce the readout duration, and hence any image distortion is reduced by the same factor. As fMRI is an acquisition mode in which the TE is fixed, in-plane acceleration does not lead to a significant reduction in acquisition times. If data are to be acquired in the thermal noise regime, then in-plane acceleration will also lead to a loss in sensitivity as data are acquired for less time. SMS, however, will increase the acquisition speed by a factor equal to the acceleration factor, and provided that g-noise can be neglected, then there is no loss of sensitivity. Since the invention of the CAIPIRINHA (controlled aliasing in parallel imaging results in higher acceleration) technique [553] and its EPI-specific variant, blipped CAIPI [554], acceleration in the slice and phase-encoding directions can be regarded as interchangeable in the sense that coil sensitivity profiles along the phase-encoding direction can be used for slice acceleration and vice versa. Hence, the g-noise level is mainly determined by the total acceleration factor and not by its distribution along specific imaging axes. For 7 T and the current generation of 32-channel receiver coils, the rule of thumb for keeping g-noise at an acceptable level is to use an acceleration factor of below about 10.

In light of the considerations given above, a range of viable techniques is available for performing fMRI at 7 T. Here a short summary is given of the salient features of each of these techniques with regard to their implementation at 7 T; for more details regarding the characteristics of these sequences at UHF see [555].

9.1.1. 2D gradient-echo EPI

Despite all considerations of superior intrinsic resolution for spin echo, gradient-echo EPI remains the standard workhorse for fMRI at 7 T. The BOLD contrast is maximum when TE is matched to the $T2^*$ of gray matter. This gives a value of about 25 ms at 7 T. As ever, the duration of the EPI readout is limited by $T2^*$, which makes it necessary to limit the duration of the EPI readout using in-plane acceleration, possibly combined with partial Fourier acquisition. A prime example of a state-of-the-art acquisition protocol for 2D EPI would be that used for the Human Connectome Project [556]: TR 1 s, TE 22.5 ms, in-plane acceleration factor 2, SMS acceleration factor 5, readout train duration 36 ms (7/8 partial Fourier acquisition), spatial resolution 1.6 mm isotropic. In general, this sequence shows a high efficiency and sensitivity, and it is difficult to beat as the method of choice for most fMRI applications.

9.1.2. 3D gradient-echo EPI

This technique [557] has attracted considerable attention in recent years as, like CAIPI-accelerated 2D EPI, it offers the potential benefit of acceleration along two spatial axes. Typically, a plane in k-space is acquired with each successive excitation of the 3D volume. Hence, data are acquired from the entire volume with each excitation, giving a potential advantage over 2D EPI for acquisitions with a high spatial resolution. This is because if the volume TR for 2D EPI exceeds T1, then the efficiency of the acquisition is reduced. 3D EPI offers the further advantage that spin history effects are considerably lower than for 2D acquisitions because of the acquisition of a large contiguous volume without slice gaps. The volume TR in 3D EPI is typically of the order of several seconds for high-resolution whole-brain acquisitions, which makes it potentially more vulnerable to physiological fluctuations, and the correction of these has been shown to be important for maintaining the sensitivity in fMRI [558,559].

9.1.3. Spin-echo EPI

As outlined above, spin-echo EPI offers the hope of potentially improved spatial resolution for fMRI [542] and was successfully demonstrated for fMRI relatively early in the development of 7 T [560]. Parallel transmission technology is required to achieve uniform signal intensity throughout the brain, as otherwise there is typically a lower signal at the center (cf. Fig. 1 in [561]). For whole-brain acquisitions power deposition can also be limiting. The use of radiofrequency pulses where the power deposition is independent of the number of slices (PINS [562], MULTI-PINS [563]) can ameliorate the latter problem. The greatest power reduction with such pulses is of course obtained when all the acceleration is in the slice direction, and conversely none in the phase-encoding direction, leading to a dependency between image distortion and SAR. Similarly, the longer the readout train, the greater the degree of T2′ weighting and the less pure T2 contrast [564], where $1/T2^* = 1/T2 + 1/T2'$. For a more extensive review of the application of spin echoes in fMRI see [565].

9.1.4. Comparison between gradient and spin-echo fMRI

Comparisons between pulse sequences for fMRI present considerable difficulties given the variation in signal changes recorded between repeated scans in the same subject, between repeated sessions in the same subject, and of course across subjects. Any such study that uses activation strength as a metric thus needs to have sufficient statistical power to detect differences in sensitivity between the sequences. Hence, surrogate measures such as time-course SNR (tSNR) are often used, although even the value of this metric has recently been questioned [566]. There is a general agreement in the community that spin echo offers a better intrinsic spatial resolution than gradient echo, an assertion that is supported by measurements of the point spread function (PSF) [567,568] and high-resolution studies in humans at both 7 T [544,560] and 9.4 T [569]. Nevertheless, a direct comparison between the two sequences at 7 T at an intermediate spatial resolution of 1.5 mm showed that in general gradient echo had a higher sensitivity in almost all regions of the brain [561].

9.1.5. Gradient and spin echo (GRASE)

This sequence delivers a functional contrast that is mainly driven by T2 changes. As its name implies, GRASE is a hybrid acquisition scheme comprising repeated gradient-echo acquisition in a string of spin echoes [570]. The most common acquisition scheme for fMRI utilizes 3D GRASE [571] as T2 and $T2^*$ broadening can then be arranged on orthogonal axes by acquiring a k_xk_y-plane of data at each spin echo. Although the spatial resolution is limited for whole-brain coverage, 3D GRASE can also be used for zoomed acquisitions [572] at substantially higher spatial resolution. The functional contrast obtained is essentially similar to that of spin-echo EPI. Performance can be improved by using variable refocusing pulse angles along the echo train [573].

9.1.6. Steady-state free precession (SSFP)

fMRI based on SSFP is attractive for UHF applications as it can offer a range of different contrasts, some of them similar to T2, but without the high power deposition associated with spin-echo sequences. The contrast may be generated in a balanced SSFP (bSSFP) sequence, in which case there is a distinction in the fMRI contrast between transition [574,575] and pass-band bSSFP sequences [576–578], or in non-balanced SSFP [579,580] where the main contrast of interest is that of contrast-enhanced Fourier-acquired steady state (CE-FAST) [581], which is T2-like. A full discussion of SSFP contrast in fMRI is beyond the scope of this article, but the topic has been reviewed in [582]. Succinctly, the transition-band approach is sensitive to frequency changes induced by activation and may well be driven mainly by mechanisms associated with T2′. The pass-band approach is more robust to frequency offsets, but both bSSFP approaches remain sensitive to inhomogeneities in B_0 and usually require two acquisitions to compensate for these effects. Non-balanced SSFP is robust against B_0 inhomogeneities, but the imbalanced gradients make it more sensitive to motion.

9.2. Applications

There is a broad range of applications of fMRI at ultra-high field, and to attempt to cover them all would be beyond the scope of this article. Instead, specific applications are presented to which fMRI at ultra-high field would appear particularly well-suited. These include high spatial resolution acquisitions in the neocortex and sub-cortical gray matter, with extension to the cortical layers and cortical columns.

9.2.1. High-resolution fMRI

An immediate attraction of performing fMRI at ultra-high field strength is the potential for improved intrinsic spatial resolution. Most studies have concentrated on imaging primary cortices, where some underlying fine structure was already known or hypothesized from animal experiments. One of the most impressive early demonstrations of the potential power of UHF fMRI was the discovery of tonotopic maps in primary auditory cortex [583]. This was followed roughly a decade later by the discovery of similar tonotopic maps in the human inferior colliculus [584].

The somatosensory cortex could also be mapped at 1 mm isotropic spatial resolution, whereby it was possible to find a somatosensory representation for each digit [585] in the primary somatosensory cortex (S1) as shown in Fig. 27A. S1 is known to consist cytoarchitectonically of four Brodmann areas (1, 2, 3a, and 3b). It could subsequently be shown how to further subdivide S1 into four distinct regions corresponding to these areas on the basis of phase reversal in the response between adjacent regions of the representation of the index finger [586], as illustrated in the phase map of Fig. 27B. Somatotopic representations of human digits could later be found in the anterior and posterior lobes of the cerebellum [587] and in the dentate nucleus [588].

The visual cortex has of course proven to be a rich area of examination for fMRI, providing some of the most striking results that have been achieved from the perspective of cortical layers and columns, which are discussed below. A recent study [589] has been able to detect and distinguish color and binocular disparity stripes in both V2 and V3 using 1-mm-resolution fMRI at 7 T, which is about the same dimension as that expected for the stripes.

9.2.2. Layers and columns

The work described in the previous subsection was mainly carried out with a spatial resolution in the range of 1–1.5 mm. The human neocortex is roughly 3 mm thick and contains up to 6 histological layers, while cortical columns vary in diameter but will often be smaller than 1 mm. To image these structures it is hence necessary to increase the spatial resolution to better than 1 mm, and in many situations a necessary corollary of this is that whole-brain coverage is no longer achievable.

In terms of hemodynamics, it may seem surprising that imaging at sufficient spatial resolution to resolve the laminae is even feasible, given that the spatial point spread function for BOLD at 7 T is about 2 mm. The standard measurement of spatial PSF, however, involves retinotopic mapping techniques [590] that set up a wave of activation along V1, which includes contributions from both parenchymal and pial vasculature. Hence, retinotopic mapping experiments in humans are designed to elucidate the spatial point spread function of the BOLD response along the cortical surface. Laminar fMRI considers the activation pattern orthogonal to this

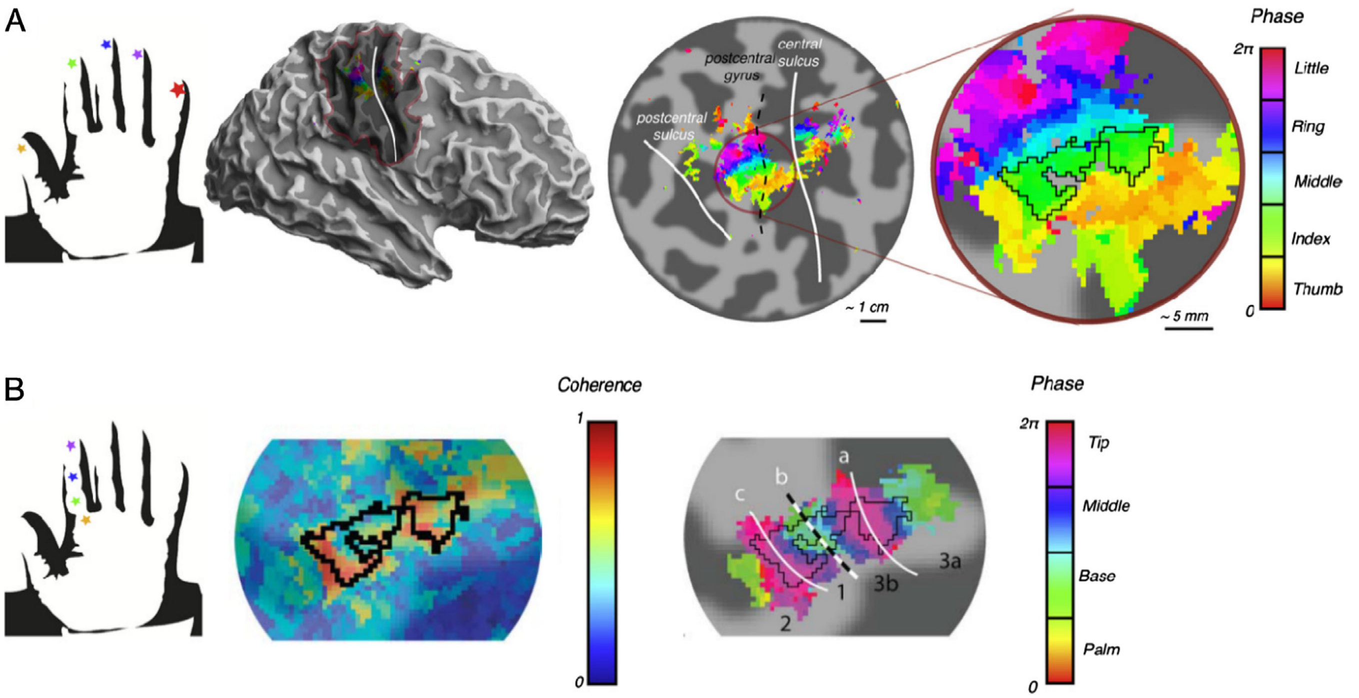

Fig. 27. (A) Results from a traveling-wave experiment in which all fingertips of the left hand were stimulated. Phase maps, thresholded at a coherence value of 0.25, are displayed on an inflated 3D model of the right hemisphere cortical surface (left) and flattened cortical patch (right). Dark gray = areas of negative curvature (sulci); light gray = areas of positive curvature (gyri); shaded area on the 3D model = location of the cortical flat patch. The orderly representation of the fingers is found in the posterior bank of the central sulcus (white line) and the postcentral gyrus (dashed black line), corresponding to S1. The black line of the inset image represents the delineation of the index finger ROI, which consists of phase values encoded by the green color. (B) Results of the traveling-wave paradigm across sites of the index finger for one subject. Coherence (left) shown with index fingertip ROI overlaid in black, and phase map (right) for the expanded ROI, thresholded at a coherence value of 0.25, displayed over the same patch as inset in (A). In the phase map, white segments (a, c) and the black and white dashed segment (b) emphasize phase reversals at the tip and base of the index finger, respectively, thus showing the putative delineation into the Brodmann areas 1, 2, 3a, 3b. Figure and caption adapted from Figs. 2 and 3 of [586].

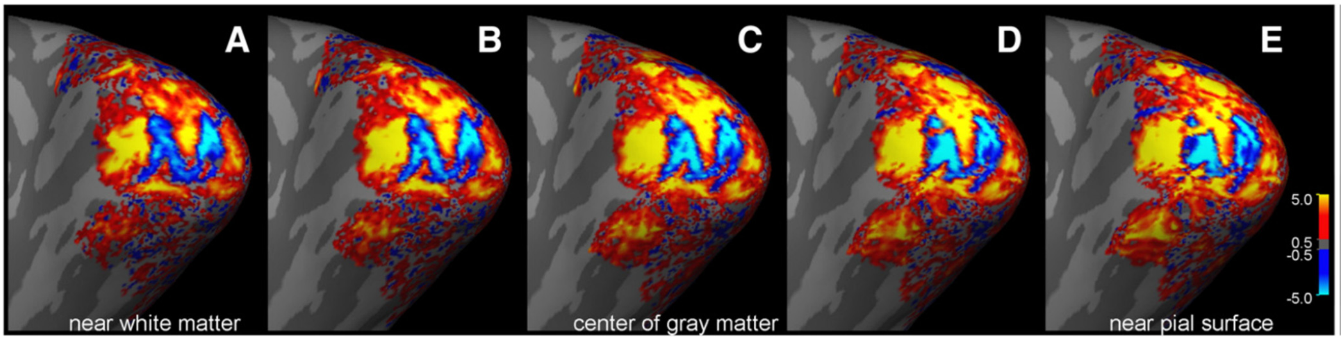

Fig. 28. The activity pattern of the "M" stimulus calculated from two 2.5-min acquisitions (i.e., 5 min total acquisition time) resulting from differential imaging of the two stimulus conditions and displayed on the inflated cortical surface. (A) Activity at the lowest depth (near white matter). (B–D) Activity at intermediate depths. (E) Activity at shallow depth (near pial surface). Color scale provided on the bottom right for z-statistic values. Activity becomes stronger from the white matter surface to the central surfaces, then deteriorates near the pial surface—consistent with a dominance of the macrovasculature at the pial surface. Figure and caption adapted from [591].

axis, which is also the axis along which blood drains from the white matter boundary to the pial surface. Given this vascular architecture, it is to be expected that the spatial specificity of the fMRI signal decreases going from the white matter boundary to the pial surface, while its sensitivity increases. This has been beautifully illustrated by activating the pattern of the letter "M" on primary visual cortex [591] as shown in Fig. 28. Detailed investigation using multi-echo RF-spoiled gradient echo has shown how the activation profile in primary visual cortex varies with the TE, because at short TE the intravascular signal (with short T2) tends to dominate, whereas at longer TE the parenchymal signal is more important [592].

Two very recent studies have shown signal changes that have been interpreted as being the result of feedback from higher-order regions to primary visual cortex [593,594]. The main result of [594] is shown in Fig. 29, where the effect of rotating three Pac-Man figures to form an illusory triangle is illustrated. The laminar profile is obtained from a patch of V1 in which only the illusory figure is represented, not the Pac-Man figures. Hence, the visual input to this region is identical irrespective of whether the illusion is present (green) or not (red). The laminar profile is, however, markedly different as the signal from lower layers is higher when the illusion is present, in line with a feedback loop to layers V/VI.

The use of gradient-echo contrast for laminar fMRI brings with it a certain degree of signal contamination caused by the flow of blood from deeper to more superficial layers. This signal from larger vessels will be visible in gradient echo but not spin echo,

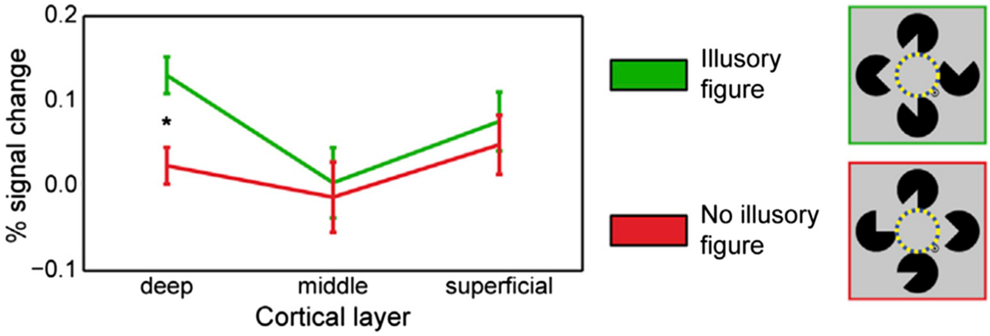

Fig. 29. BOLD response to illusory figures (green) and control stimuli (red) in the region of V1 with receptive fields on the illusory figure but not on the Pac-Man inducers. * p = 0.0070. Figure and caption adapted from [594].

and hence a pure spin-echo signal should be localized in the layer from which it originates [595]. Thus, spin-echo-based contrasts such as spin-echo EPI or 3D GRASE have also been used for laminar fMRI [596] and have been argued to have superior characteristics compared to gradient-echo acquisitions [573,597].

Also in the study of cortical columns, spin-echo acquisition has generally been preferred. In the examination of ocular dominance columns, a segmented spin-echo EPI (4 segments) was used [598]. This same technique was also employed to detect for the first time orientation-dependent columns in humans using fMRI [599]. More recently, columnar structures have been found in auditory cortex [600] using 3D GRASE.

In summary, despite almost two decades of intensive research applications and measurement, methods for fMRI at UHF are still being developed. High spatial resolution studies are the main area of application, and the greater sensitivity available at UHF offers hope of ultimately being able to image at a mesoscopic level corresponding to the brain's intrinsic functional units of layers and columns.

10. Conclusions

MRI[2] has established itself as one of the premier diagnostic methods in modern clinical medicine. It has also gained an essential role in state-of-the-art neurocognitive research by providing important information on both the structure and function of the human brain (cf. Section 9). The main weakness of the technique remains its limited sensitivity, leading to a persistent trade-off between spatial and temporal resolution that prevents it from fulfilling its full potential to provide important biological and metabolic information.

The progress to higher magnetic fields to address this deficit and improve MR sensitivity has been led by analytical NMR as well as preclinical MRI, as these applications require smaller magnet bore sizes [416]. A clear difference between human-sized systems and these small-bore systems is the size of the object. In human-sized objects at UHF, one leaves the quasi-static regime and enters the electromagnetic regime, and wave propagation has to be considered. Both theoretical [23] as well as experimental studies have shown a supralinear increase in SNR that is additionally spatially non-uniform, with deeper-lying structures profiting disproportionately. A recent well-designed experimental study revealed an increase in SNR proportional to $B_0^{1.65}$ in the range 3 T to 9.4 T in the human brain [25].

The increase in SNR and CNR at UHF (cf. Section 1.1) is a universal benefit that can not only improve existing applications including high-resolution structural imaging (cf. Section 4) and susceptibility-weighted imaging (cf. Section 5), but can also facilitate completely new application domains for MR, particularly in spectroscopy and CEST imaging with ^{1}H as well as imaging and spectroscopy with X-nuclei (cf. Sections 6–8). With the availability of UHF, these new applications may even be able to make the leap from research to clinical diagnostic use.

Superconducting MRI magnets for human use with a magnetic field strength of 1.5 T were introduced into clinical routine in the mid-1980s and continue to be the mainstay of diagnostic imaging [416]. Since then, 3 T has become a further standard of clinical care, in particular for high-end neuro imaging. A major system supplier recently announced the approval of a 7 T system for use in medical diagnostics with both FDA clearance [15] and CE labeling as a medical device. However, the system is currently only approved for imaging of the head, legs, and arms. The reason for these anatomical restrictions lies in unsolved challenges to high-quality imaging at high magnetic fields. The difficulties for MR when moving to higher magnetic fields have been summarized in several review articles [24,287,602–604]. Although many of these difficulties have been successfully addressed, a notable remaining challenge still being actively researched is related to the RF magnetic and electric fields necessary for spin excitation (cf. Section 3). A significant difference encountered at ultra-high fields is that the wavelength of the RF fields inside the tissue is on the order of or shorter than the cross-sectional dimension of the human body, which implies that phase effects and wave propagation have to be accounted for. In large cross sections of the anatomy like the torso, signal dropouts due to destructive interferences can make imaging with conventional excitation approaches unfeasible. Therefore, new multi-channel excitation coils [146] are being introduced to provide precise control over the RF field distribution to enable high-quality imaging even over large volumes [605].

The highest magnetic field currently available for human use is 10.5 T/450 MHz (Center for Magnetic Resonance Research, University of Minnesota, USA) [606]. Projects currently being realized or planned for the near future are targeting 11.7 T/500 MHz (e.g. Neurospin CEA, Saclay, France [607]; National Institute of Health, Bethesda, MD, USA; Gachon Medical University, Incheon, Korea). In the USA, there is a concerted effort being made to achieve first 14 T/600 MHz and ultimately 20 T/850 MHz for studying the human brain [275,276]. Germany has also formed a consortium to establish a 14 T MRI system as part of a national imaging facility (not yet funded) [608]. Although the field strength (14 T) is identical to the initiative in the USA, a major difference of the German initiative is that it is targeting a whole-body system so as to also enable study of the heart, kidneys, liver, lungs, and other organs of the torso.

The step beyond 11.7 T implies a significant technology leap for human-sized magnets. The superconductor used for almost all superconducting magnets up to 11.7 T is niobium-titanium, but higher field strengths require at least partial use of a superconductor

---

[2] Parts of Section 10 are based on [601].

with higher critical field, most likely niobium-tin (Nb_3Sn) [609]. Due to the manufacturing difficulties of niobium-tin, its price is approximately an order of magnitude higher than that of niobium-titanium. Despite these technological and economic challenges, it is likely that the upper limit of magnetic field strength will ultimately be determined by the physiological effects of strong magnetic fields (cf. Section 2). Although no long-term health effects of static magnetic field exposure are currently known, transient sensory side effects such as nausea, dizziness, metallic taste, and light flashes may be become so severe at some point that subjects are unwilling to be exposed. Nevertheless, the experience at 7 T and 9.4 T has demonstrated that these side effects are not yet a major concern [52].

It should be noted that at the current time, none of the projects above 7 T is targeted at introducing a new magnetic field strength into routine clinical use. Rather, they are being pursued with the goal of obtaining new insights into healthy brain function or disease pathophysiology in groups of patients. It will likely be a long road until such high field strengths become practical from a technical and economic point of view for examining individual patients. Nevertheless, the versatility and power of the MR technique will continue to drive the quest for ever higher magnetic fields to help unravel important unanswered questions about healthy physiology, pathological processes, brain function, and ageing.

Acknowledgements

MEL has received funding for the research leading to these results from the European Research Council under the European Union's Seventh Framework Programme (FP/2007-2013)/ERC Grant Agreement n. 291903 MRexcite. EM acknowledges funding through an unrestricted 7 T grant by Siemens Medical Systems (Austria) and the Research Studio Austria program of the FFG. MM acknowledges financial support via the ANR/FWF program (Project Nr. I 1743-B13). OS received support from NIH grant number 1R01-DA021146. In no case did the funding source have any influence on the research outcome or interpretation.

References

[1] R. Damadian, Tumor detection by nuclear magnetic resonance, Science 171 (1971) 1151–1153.

[2] P.C. Lauterbur, Image formation by induced local interactions: examples employing nuclear magnetic resonance, Nature 242 (1973) 190–191.

[3] P. Mansfield, P.K. Grannell, NMR diffraction in solids, J. Phys. C-Solid State Phys. 6 (1973) L422–L426.

[4] V.R. Fuchs, H.C. Sox, Physicians' views of the relative importance of thirty medical innovations, Health Aff. 20 (2001) 30–42.

[5] IMV, MR Market Outlook Report, 2016. <http://www.imvinfo.com/index.aspx?sec=mri&sub=dis&itemid=200085> (accessed 22 August 2017).

[6] R. Smith-Bindman, D.L. Miglioretti, E.B. Larson, Rising use of diagnostic medical imaging in a large integrated health system, Health Aff. (Millwood) 27 (2008) 1491–1502.

[7] B.D. Ross, P. Bhattacharya, S. Wagner, T. Tran, N. Sailasuta, Hyperpolarized MR imaging: neurologic applications of hyperpolarized metabolism, AJNR Am. J. Neuroradiol. 31 (2010) 24–33.

[8] A. Viale, F. Reineri, D. Santelia, E. Cerutti, S. Ellena, R. Gobetto, S. Aime, Hyperpolarized agents for advanced MRI investigations, Q. J. Nucl. Med. Mol. Imaging 53 (2009) 604–617.

[9] P. Bachert, L.R. Schad, M. Bock, M.V. Knopp, M. Ebert, T. Grossmann, W. Heil, D. Hofmann, R. Surkau, E.W. Otten, Nuclear magnetic resonance imaging of airways in humans with use of hyperpolarized 3He, Magn. Reson. Med. 36 (1996) 192–196.

[10] D.G. Norris, High field human imaging, J. Magn. Reson. Imaging 18 (2003) 519–529.

[11] P.M. Robitaille, A.M. Abduljalil, A. Kangarlu, Ultra high resolution imaging of the human head at 8 tesla: 2K × 2K for Y2K, J. Comput. Assist. Tomogr. 24 (2000) 2–8.

[12] J.T. Vaughan, M. Garwood, C.M. Collins, W. Liu, L. DelaBarre, G. Adriany, P. Andersen, H. Merkle, R. Goebel, M.B. Smith, K. Ugurbil, 7T vs. 4T: RF power, homogeneity, and signal-to-noise comparison in head images, Magn. Reson. Med. 46 (2001) 24–30.

[13] P.M. Robitaille, R. Warner, J. Jagadeesh, A.M. Abduljalil, A. Kangarlu, R.E. Burgess, Y. Yu, L. Yang, H. Zhu, Z. Jiang, R.E. Bailey, W. Chung, Y. Somawiharja, P. Feynan, D.L. Rayner, Design and assembly of an 8 tesla whole-body MR scanner, J. Comput. Assist. Tomogr. 23 (1999) 808–820.

[14] E. Yacoub, A. Shmuel, J. Pfeuffer, P.F. Van De Moortele, G. Adriany, P. Andersen, J.T. Vaughan, H. Merkle, K. Ugurbil, X. Hu, Imaging brain function in humans at 7 Tesla, Magn. Reson. Med. 45 (2001) 588–594.

[15] United States Food and Drug Administration, FDA clears first 7T magnetic resonance imaging device, 2017. <www.fda.gov/NewsEvents/Newsroom/PressAnnouncements/ucm580154.htm> (accessed 11 November 2017).

[16] D.I. Hoult, Sensitivity and power deposition in a high-field imaging experiment, J. Magn. Reson. Imaging 12 (2000) 46–67.

[17] D.I. Hoult, R.E. Richards, The signal-to-noise ratio of the nuclear magnetic resonance experiment, J. Magn. Reson. 24 (1976) 71–85.

[18] W.A. Edelstein, G.H. Glover, C.J. Hardy, R.W. Redington, The intrinsic signal-to-noise ratio in NMR imaging, Magn. Reson. Med. 3 (1986) 604–618.

[19] T.M. Fiedler, M.E. Ladd, A.K. Bitz, SAR simulations & safety, Neuroimage 168 (2018) 33–58.

[20] O. Ocali, E. Atalar, Ultimate intrinsic signal-to-noise ratio in MRI, Magn. Reson. Med. 39 (1998) 462–473.

[21] R. Lattanzi, D.K. Sodickson, Ideal current patterns yielding optimal signal-to-noise ratio and specific absorption rate in magnetic resonance imaging: computational methods and physical insights, Magn. Reson. Med. 68 (2012) 286–304.

[22] W. Schnell, W. Renz, M. Vester, H. Ermert, Ultimate signal-to-noise-ratio of surface and body antennas for magnetic resonance imaging, IEEE Trans. Antennas Propag. 48 (2000) 418–428.

[23] B. Guerin, J.F. Villena, A.G. Polimeridis, E. Adalsteinsson, L. Daniel, J.K. White, L.L. Wald, The ultimate signal-to-noise ratio in realistic body models, Magn. Reson. Med. 78 (2017) 1969–1980.

[24] E. Moser, F. Stahlberg, M.E. Ladd, S. Trattnig, 7-T MR-from research to clinical applications?, NMR Biomed 25 (2012) 695–716.

[25] R. Pohmann, O. Speck, K. Scheffler, Signal-to-noise ratio and MR tissue parameters in human brain imaging at 3, 7, and 9.4 tesla using current receive coil arrays, Magn. Reson. Med. 75 (2016) 801–809.

[26] D. Stucht, K.A. Danishad, P. Schulze, F. Godenschweger, M. Zaitsev, O. Speck, Highest resolution in vivo human brain MRI using prospective motion correction, PLoS One 10 (2015) e0133921.

[27] F. Lusebrink, A. Sciarra, H. Mattern, R. Yakupov, O. Speck, T1-weighted in vivo human whole brain MRI dataset with an ultrahigh isotropic resolution of 250 mum, Sci. Data 4 (2017) 170032.

[28] A. Christ, W. Kainz, E.G. Hahn, K. Honegger, M. Zefferer, E. Neufeld, W. Rascher, R. Janka, W. Bautz, J. Chen, B. Kiefer, P. Schmitt, H.P. Hollenbach, J. Shen, M. Oberle, D. Szczerba, A. Kam, J.W. Guag, N. Kuster, The Virtual Family – development of surface-based anatomical models of two adults and two children for dosimetric simulations, Phys. Med. Biol. 55 (2010) N23–38.

[29] M.A. Bernstein, K.F. King, X.J. Zhou, Handbook of MRI Pulse Sequences, Elsevier Academic Press, Burlington, MA, 2004.

[30] R.W. Brown, Y.-C.N. Cheng, E.M. Haacke, M.R. Thompson, R. Venkatesan, Magnetic Resonance Imaging: Physical Principles and Sequence Design, John Wiley & Sons Inc, New Jersey, 2014.

[31] S. Ogawa, R.S. Menon, D.W. Tank, S.-G. Kim, H. Merkle, J.M. Ellermann, K. Ugurbil, Functional brain mapping by blood oxygenation level-dependent contrast magnetic resonance imaging: a comparison of signal characteristics with a biophysical model, Biophys. J. 64 (1993) 803–812.

[32] E. Yacoub, A. Shmuel, J. Pfeuffer, P.F. Van De Moortele, G. Adriany, K. Ugurbil, X. Hu, Investigation of the initial dip in fMRI at 7 Tesla, NMR Biomed. 14 (2001) 408–412.

[33] International Electrotechnical Commission, Medical electrical equipment Part 2-33: Particular requirements for the safety of magnetic resonance diagnostic devices, in: IEC (Ed.), 60601-2-33, Edition 3.2, 2015.

[34] United States Food and Drug Administration, Criteria for significant risk investigations of magnetic resonance diagnostic devices, in: FDA (Ed.), Guidance for Industry and Food and Drug Administration Staff, 2014.

[35] M. Davids, B. Guerin, M. Malzacher, L.R. Schad, L.L. Wald, Predicting magnetostimulation thresholds in the peripheral nervous system using realistic body models, Sci. Rep. 7 (2017) 5316.

[36] C.L. Ham, J.M. Engels, G.T. van de Wiel, A. Machielsen, Peripheral nerve stimulation during MRI: effects of high gradient amplitudes and switching rates, J. Magn. Reson. Imaging 7 (1997) 933–937.

[37] C. Heilmaier, J.M. Theysohn, S. Maderwald, O. Kraff, M.E. Ladd, S.C. Ladd, A large-scale study on subjective perception of discomfort during 7 and 1.5 T MRI examinations, Bioelectromagnetics 32 (2011) 610–619.

[38] J.R. Keltner, M.S. Roos, P.R. Brakeman, T.F. Budinger, Magnetohydrodynamics of blood flow, Magn. Reson. Med. 16 (1990) 139–149.

[39] J.W. Krug, G. Rose, G.D. Clifford, J. Oster, ECG-based gating in ultra high field cardiovascular magnetic resonance using an independent component analysis approach, J. Cardiovasc. Magn. Reson. 15 (2013) 104.

[40] I.I.H. Chen, S. Saha, Analysis of an intensive magnetic field on blood flow, J. Bioelectr. 3 (1984) 293–298.

[41] I.C. Atkinson, L. Renteria, H. Burd, N.H. Pliskin, K.R. Thulborn, Safety of human MRI at static fields above the FDA 8 T guideline: sodium imaging at 9.4 T does not affect vital signs or cognitive ability, J. Magn. Reson. Imaging 26 (2007) 1222–1227.

[42] Y. Eryaman, P. Zhang, L. Utecht, K. Kose, R.L. Lagore, L. DelaBarre, J. Kulesa, L.E. Eberly, G. Adriany, T.L. Iles, P.A. Iaizzo, J.T. Vaughan, K. Ugurbil, Investigating

the physiological effects of 10.5 Tesla static field exposure on anesthetized swine, Magn. Reson. Med. 79 (2018) 511–514.

[43] F. de Vocht, T. Stevens, P. Glover, A. Sunderland, P. Gowland, H. Kromhout, Cognitive effects of head-movements in stray fields generated by a 7 Tesla whole-body MRI magnet, Bioelectromagnetics 28 (2007) 247–255.

[44] L.E. van Nierop, P. Slottje, M.J. van Zandvoort, F. de Vocht, H. Kromhout, Effects of magnetic stray fields from a 7 tesla MRI scanner on neurocognition: a double-blind randomised crossover study, Occup. Environ. Med. 69 (2012) 759–766.

[45] L.E. van Nierop, P. Slottje, M. van Zandvoort, H. Kromhout, Simultaneous exposure to MRI-related static and low-frequency movement-induced time-varying magnetic fields affects neurocognitive performance: a double-blind randomized crossover study, Magn. Reson. Med. 74 (2015) 840–849.

[46] A. Heinrich, A. Szostek, P. Meyer, F. Nees, J. Rauschenberg, J. Grobner, M. Gilles, G. Paslakis, M. Deuschle, W. Semmler, H. Flor, Cognition and sensation in very high static magnetic fields: a randomized case-crossover study with different field strengths, Radiology 266 (2013) 236–245.

[47] M. Schlamann, M.A. Voigt, S. Maderwald, A.K. Bitz, O. Kraff, S.C. Ladd, M.E. Ladd, M. Forsting, H. Wilhelm, Exposure to high-field MRI does not affect cognitive function, J. Magn. Reson. Imaging 31 (2010) 1061–1066.

[48] J. Lepsien, K. Muller, D.Y. von Cramon, H.E. Moller, Investigation of higher-order cognitive functions during exposure to a high static magnetic field, J. Magn. Reson. Imaging 36 (2012) 835–840.

[49] O.S. Mian, Y. Li, A. Antunes, P.M. Glover, B.L. Day, Effect of head pitch and roll orientations on magnetically induced vertigo, J. Physiol. 594 (2016) 1051–1067.

[50] M. Thormann, H. Amthauer, D. Adolf, A. Wollrab, J. Ricke, O. Speck, Efficacy of diphenhydramine in the prevention of vertigo and nausea at 7 T MRI, Eur. J. Radiol. 82 (2013) 768–772.

[51] D.A. Hanes, G. McCollum, Cognitive-vestibular interactions: a review of patient difficulties and possible mechanisms, J. Vestib. Res. 16 (2006) 75–91.

[52] J. Rauschenberg, A.M. Nagel, S.C. Ladd, J.M. Theysohn, M.E. Ladd, H.E. Moller, R. Trampel, R. Turner, R. Pohmann, K. Scheffler, A. Brechmann, J. Stadler, J. Felder, N.J. Shah, W. Semmler, Multicenter study of subjective acceptance during magnetic resonance imaging at 7 and 9.4 T, Invest. Radiol. 49 (2014) 249–259.

[53] D. Heylmann, B. Kaina, The gammaH2AX DNA damage assay from a drop of blood, Sci. Rep. 6 (2016) 22682.

[54] C.E. Redon, A.J. Nakamura, O. Sordet, J.S. Dickey, K. Gouliaeva, B. Tabb, S. Lawrence, R.J. Kinders, W.M. Bonner, O.A. Sedelnikova, Gamma-H2AX detection in peripheral blood lymphocytes, splenocytes, bone marrow, xenografts, and skin, Methods Mol. Biol. 682 (2011) 249–270.

[55] D.K. Woolf, N.R. Williams, R. Bakshi, S.Y. Madani, D.J. Eaton, S. Fawcitt, K. Pigott, S. Short, M. Keshtgar, Biological dosimetry for breast cancer radiotherapy: a comparison of external beam and intraoperative radiotherapy, Springerplus 3 (2014) 329.

[56] M. Fenech, S. Bonassi, The effect of age, gender, diet and lifestyle on DNA damage measured using micronucleus frequency in human peripheral blood lymphocytes, Mutagenesis 26 (2011) 43–49.

[57] J.W. Lee, M.S. Kim, Y.J. Kim, Y.J. Choi, Y. Lee, H.W. Chung, Genotoxic effects of 3 T magnetic resonance imaging in cultured human lymphocytes, Bioelectromagnetics 32 (2011) 535–542.

[58] S. Simi, M. Ballardin, M. Casella, D. De Marchi, V. Hartwig, G. Giovannetti, N. Vanello, S. Gabbriellini, L. Landini, M. Lombardi, Is the genotoxic effect of magnetic resonance negligible? Low persistence of micronucleus frequency in lymphocytes of individuals after cardiac scan, Mutat. Res. 645 (2008) 39–43.

[59] A. Szerencsi, G. Kubinyi, E. Valiczko, P. Juhasz, G. Rudas, A. Mester, G. Janossy, J. Bakos, G. Thuroczy, DNA integrity of human leukocytes after magnetic resonance imaging, Int. J. Radiat. Biol. 89 (2013) 870–876.

[60] S. Yildiz, H. Cece, I. Kaya, H. Celik, A. Taskin, N. Aksoy, A. Kocyigit, M.A. Eren, Impact of contrast enhanced MRI on lymphocyte DNA damage and serum visfatin level, Clin. Biochem. 44 (2011) 975–979.

[61] M. Brand, S. Ellmann, M. Sommer, M.S. May, A. Eller, W. Wuest, C. Engert, S. Achenbach, M.A. Kuefner, T. Baeuerle, M. Lell, M. Uder, Influence of cardiac MR imaging on DNA double-strand breaks in human blood lymphocytes, Radiology 277 (2015) 406–412.

[62] M. Fatahi, A. Reddig, B. Vijayalaxmi, R. Friebe, T.J. Hartig, J. Prihoda, D. Ricke, D. Roggenbuck, O. Speck Reinhold, DNA double-strand breaks and micronuclei in human blood lymphocytes after repeated whole body exposures to 7T Magnetic Resonance Imaging, Neuroimage 133 (2016) 288–293.

[63] M. Fiechter, J. Stehli, T.A. Fuchs, S. Dougoud, O. Gaemperli, P.A. Kaufmann, Impact of cardiac magnetic resonance imaging on human lymphocyte DNA integrity, Eur. Heart J. 34 (2013) 2340–2345.

[64] P. Lancellotti, A. Nchimi, C. Delierneux, A. Hego, C. Gosset, A. Gothot, L. Jean-Flory Tshibanda, C. Oury, Biological effects of cardiac magnetic resonance on human blood cells, Circ. Cardiovasc. Imaging 8 (2015) e003697.

[65] A. Reddig, M. Fatahi, B. Friebe, K. Guttek, R. Hartig, F. Godenschweger, D. Roggenbuck, J. Ricke, D. Reinhold, O. Speck, Analysis of DNA double-strand breaks and cytotoxicity after 7 Tesla magnetic resonance imaging of isolated human lymphocytes, PLoS One 10 (2015) e0132702.

[66] A. Reddig, M. Fatahi, D. Roggenbuck, J. Ricke, D. Reinhold, O. Speck, B. Friebe, Impact of in vivo high-field-strength and ultra-high-field-strength MR imaging on DNA double-strand-break formation in human lymphocytes, Radiology 282 (2017) 782–789.

[67] N.F. Schwenzer, R. Bantleon, B. Maurer, R. Kehlbach, C. Schraml, C.D. Claussen, E. Rodegerdts, Detection of DNA double-strand breaks using gammaH2AX after MRI exposure at 3 Tesla: an in vitro study, J. Magn. Reson. Imaging 26 (2007) 1308–1314.

[68] K.R. Foster, J.E. Moulder, T.F. Budinger, Will an MRI examination damage your genes?, Radiat Res. 187 (2017) 1–6.

[69] M.A. Hill, P. O'Neill, W.G. McKenna, Comments on potential health effects of MRI-induced DNA lesions: quality is more important to consider than quantity, Eur. Heart J. Cardiovasc. Imaging 17 (2016) 1230–1238.

[70] M. Vijayalaxmi, O. Fatahi Speck, Magnetic resonance imaging (MRI): a review of genetic damage investigations, Mutat. Res. Rev. Mutat. Res. 764 (2015) 51–63.

[71] M. Fatahi, A. Reddig, B. Friebe, D. Reinhold, O. Speck, MRI and genetic damage: an update, Curr. Radiol. Rep. 5 (2017) 20.

[72] International Commission on Non-Ionizing Radiation Protection, ICNIRP statement on diagnostic devices using non-ionizing radiation: existing regulations and potential health risks, Health Phys. 112 (2017) 305–321.

[73] European Parliament and Council, Directive 2013/35/EU of 26 June 2013 on the minimum health and safety requirements regarding the exposure of workers to the risks arising from physical agents (electromagnetic fields), in: EU (Ed.), Official Journal of the European Union, L 179/1, 2013, pp. 1–21.

[74] U. Katscher, P. Bornert, Parallel RF transmission in MRI, NMR Biomed. 19 (2006) 393–400.

[75] U. Katscher, P. Bornert, C. Leussler, J.S. van den Brink, Transmit SENSE, Magn. Reson. Med. 49 (2003) 144–150.

[76] Y. Zhu, Parallel excitation with an array of transmit coils, Magn. Reson. Med. 51 (2004) 775–784.

[77] S. Orzada, S. Maderwald, B.A. Poser, A.K. Bitz, H.H. Quick, M.E. Ladd, RF excitation using time interleaved acquisition of modes (TIAMO) to address B1 inhomogeneity in high-field MRI, Magn. Reson. Med. 64 (2010) 327–333.

[78] G.J. Metzger, E.J. Auerbach, C. Akgun, J. Simonson, X. Bi, K. Ugurbil, P.F. van de Moortele, Dynamically applied B1+ shimming solutions for non-contrast enhanced renal angiography at 7.0 Tesla, Magn. Reson. Med. 69 (2013) 114–126.

[79] J. Pauly, D. Nishimura, A. Macovski, A k-space analysis of small-tip-angle excitation, J. Magn. Reson. 81 (1989) 43–56.

[80] W. Grissom, C.Y. Yip, Z. Zhang, V.A. Stenger, J.A. Fessler, D.C. Noll, Spatial domain method for the design of RF pulses in multicoil parallel excitation, Magn. Reson. Med. 56 (2006) 620–629.

[81] F. Padormo, A. Beqiri, J.V. Hajnal, S.J. Malik, Parallel transmission for ultrahigh-field imaging, NMR Biomed. 29 (2016) 1145–1161.

[82] S. Saekho, C.Y. Yip, D.C. Noll, F.E. Boada, V.A. Stenger, Fast-kz three-dimensional tailored radiofrequency pulse for reduced B1 inhomogeneity, Magn. Reson. Med. 55 (2006) 719–724.

[83] K. Setsompop, V. Alagappan, B. Gagoski, T. Witzel, J. Polimeni, A. Potthast, F. Hebrank, U. Fontius, F. Schmitt, L.L. Wald, E. Adalsteinsson, Slice-selective RF pulses for in vivo B1+ inhomogeneity mitigation at 7 tesla using parallel RF excitation with a 16-element coil, Magn. Reson. Med. 60 (2008) 1422–1432.

[84] V. Gras, A. Vignaud, A. Amadon, F. Mauconduit, D. Le Bihan, N. Boulant, New method to characterize and correct with sub-micros precision gradient delays in bipolar multispoke RF pulses, Magn. Reson. Med. 78 (2017) 2194–2202.

[85] D.H.Y. Tse, C.J. Wiggins, B.A. Poser, Estimating and eliminating the excitation errors in bipolar gradient composite excitations caused by radiofrequency-gradient delay: example of bipolar spokes pulses in parallel transmission, Magn. Reson. Med. 78 (2017) 1883–1890.

[86] D.J. Larkman, J.V. Hajnal, A.H. Herlihy, G.A. Coutts, I.R. Young, G. Ehnholm, Use of multicoil arrays for separation of signal from multiple slices simultaneously excited, J. Magn. Reson. Imaging 13 (2001) 313–317.

[87] S. Moeller, E. Yacoub, C.A. Olman, E. Auerbach, J. Strupp, N. Harel, K. Ugurbil, Multiband multislice GE-EPI at 7 tesla, with 16-fold acceleration using partial parallel imaging with application to high spatial and temporal whole-brain fMRI, Magn. Reson. Med. 63 (2010) 1144–1153.

[88] B.A. Poser, R.J. Anderson, B. Guerin, K. Setsompop, W. Deng, A. Mareyam, P. Serano, L.L. Wald, V.A. Stenger, Simultaneous multislice excitation by parallel transmission, Magn. Reson. Med. 71 (2014) 1416–1427.

[89] X. Wu, S. Schmitter, E.J. Auerbach, S. Moeller, K. Ugurbil, P.F. Van de Moortele, Simultaneous multislice multiband parallel radiofrequency excitation with independent slice-specific transmit B1 homogenization, Magn. Reson. Med. 70 (2013) 630–638.

[90] M.A. Cloos, N. Boulant, M. Luong, G. Ferrand, E. Giacomini, D. Le Bihan, A. Amadon, kT-points: short three-dimensional tailored RF pulses for flip-angle homogenization over an extended volume, Magn. Reson. Med. 67 (2012) 72–80.

[91] V. Gras, A. Vignaud, A. Amadon, D. Le Bihan, N. Boulant, Universal pulses: a new concept for calibration-free parallel transmission, Magn. Reson. Med. 77 (2017) 635–643.

[92] M. Davids, L.R. Schad, L.L. Wald, B. Guerin, Fast three-dimensional inner volume excitations using parallel transmission and optimized k-space trajectories, Magn. Reson. Med. 76 (2016) 1170–1182.

[93] V.L. Yarnykh, Actual flip-angle imaging in the pulsed steady state: a method for rapid three-dimensional mapping of the transmitted radiofrequency field, Magn. Reson. Med. 57 (2007) 192–200.

[94] S.J. Malik, G.D. Kenny, J.V. Hajnal, Slice profile correction for transmit sensitivity mapping using actual flip angle imaging, Magn. Reson. Med. 65 (2011) 1393–1399.

[95] K. Nehrke, P. Bornert, DREAM – a novel approach for robust, ultrafast, multislice B1 mapping, Magn. Reson. Med. 68 (2012) 1517–1526.

[96] L.I. Sacolick, F. Wiesinger, I. Hancu, M.W. Vogel, B1 mapping by Bloch-Siegert shift, Magn. Reson. Med. 63 (2010) 1315–1322.

[97] B. Guerin, M. Gebhardt, S. Cauley, E. Adalsteinsson, L.L. Wald, Local specific absorption rate (SAR), global SAR, transmitter power, and excitation accuracy trade-offs in low flip-angle parallel transmit pulse design, Magn. Reson. Med. 71 (2014) 1446–1457.

[98] G. Eichfelder, M. Gebhardt, Local specific absorption rate control for parallel transmission by virtual observation points, Magn. Reson. Med. 66 (2011) 1468–1476.

[99] W.M. Brink, V. Gulani, A.G. Webb, Clinical applications of dual-channel transmit MRI: a review, J. Magn. Reson. Imaging 42 (2015) 855–869.

[100] H.P. Hetherington, N.I. Avdievich, A.M. Kuznetsov, J.W. Pan, RF shimming for spectroscopic localization in the human brain at 7 T, Magn. Reson. Med. 63 (2010) 9–19.

[101] A.T. Curtis, K.M. Gilbert, L.M. Klassen, J.S. Gati, R.S. Menon, Slice-by-slice B1+ shimming at 7 T, Magn. Reson. Med. 68 (2012) 1109–1116.

[102] S. Schmitter, X. Wu, G. Adriany, E.J. Auerbach, K. Ugurbil, P.F. Moortele, Cerebral TOF angiography at 7T: impact of B1 (+) shimming with a 16-channel transceiver array, Magn. Reson. Med. 71 (2014) 966–977.

[103] S. Schmitter, X. Wu, E.J. Auerbach, G. Adriany, J. Pfeuffer, M. Hamm, K. Ugurbil, P.F. van de Moortele, Seven-tesla time-of-flight angiography using a 16-channel parallel transmit system with power-constrained 3-dimensional spoke radiofrequency pulse design, Invest. Radiol. 49 (2014) 314–325.

[104] V.O. Boer, D.W. Klomp, C. Juchem, P.R. Luijten, R.A. de Graaf, Multislice 1H MRSI of the human brain at 7 T using dynamic B0 and B1 shimming, Magn. Reson. Med. 68 (2012) 662–670.

[105] U.E. Emir, E.J. Auerbach, P.F. Van De Moortele, M. Marjanska, K. Ugurbil, M. Terpstra, I. Tkac, G. Oz, Regional neurochemical profiles in the human brain measured by 1H MRS at 7 T using local B1 shimming, NMR Biomed. 25 (2012) 152–160.

[106] M. Marjanska, J.R. McCarten, J. Hodges, L.S. Hemmy, A. Grant, D.K. Deelchand, M. Terpstra, Region-specific aging of the human brain as evidenced by neurochemical profiles measured noninvasively in the posterior cingulate cortex and the occipital lobe using 1H magnetic resonance spectroscopy at 7 T, Neuroscience 354 (2017) 168–177.

[107] D.K. Deelchand, P.F. Van de Moortele, G. Adriany, I. Iltis, P. Andersen, J.P. Strupp, J.T. Vaughan, K. Ugurbil, P.G. Henry, In vivo 1H NMR spectroscopy of the human brain at 9.4 T: initial results, J. Magn. Reson. 206 (2010) 74–80.

[108] F. De Martino, S. Schmitter, M. Moerel, J. Tian, K. Ugurbil, E. Formisano, E. Yacoub, P.F. de Moortele, Spin echo functional MRI in bilateral auditory cortices at 7 T: an application of B1 shimming, Neuroimage 63 (2012) 1313–1320.

[109] K.M. Gilbert, A.T. Curtis, J.S. Gati, L.M. Klassen, R.S. Menon, A radiofrequency coil to facilitate B1+ shimming and parallel imaging acceleration in three dimensions at 7 T, NMR Biomed. 24 (2011) 815–823.

[110] J. Hoffmann, G. Shajan, K. Scheffler, R. Pohmann, Numerical and experimental evaluation of RF shimming in the human brain at 9.4 T using a dual-row transmit array, MAGMA 27 (2014) 373–386.

[111] N.I. Avdievich, J. Hoffmann, G. Shajan, A. Pfrommer, I.A. Giapitzakis, K. Scheffler, A. Henning, Evaluation of transmit efficiency and SAR for a tight fit transceiver human head phased array at 9.4 T, NMR Biomed. 30 (2017).

[112] G. Shajan, M. Kozlov, J. Hoffmann, R. Turner, K. Scheffler, R. Pohmann, A 16-channel dual-row transmit array in combination with a 31-element receive array for human brain imaging at 9.4 T, Magn. Reson. Med. 71 (2014) 870–879.

[113] T. Vaughan, L. DelaBarre, C. Snyder, J. Tian, C. Akgun, D. Shrivastava, W. Liu, C. Olson, G. Adriany, J. Strupp, P. Andersen, A. Gopinath, P.F. van de Moortele, M. Garwood, K. Ugurbil, 9.4T human MRI: preliminary results, Magn. Reson. Med. 56 (2006) 1274–1282.

[114] M.W. Lagemaat, V. Breukels, E.K. Vos, A.B. Kerr, M.J. van Uden, S. Orzada, A.K. Bitz, M.C. Maas, T.W. Scheenen, 1H MR spectroscopic imaging of the prostate at 7T using spectral-spatial pulses, Magn. Reson. Med. 75 (2016) 933–945.

[115] M.C. Maas, E.K. Vos, M.W. Lagemaat, A.K. Bitz, S. Orzada, T. Kobus, O. Kraff, S. Maderwald, M.E. Ladd, T.W. Scheenen, Feasibility of T2-weighted turbo spin echo imaging of the human prostate at 7 tesla, Magn. Reson. Med. 71 (2014) 1711–1719.

[116] G.J. Metzger, C. Snyder, C. Akgun, T. Vaughan, K. Ugurbil, P.F. Van de Moortele, Local B1+ shimming for prostate imaging with transceiver arrays at 7T based on subject-dependent transmit phase measurements, Magn. Reson. Med. 59 (2008) 396–409.

[117] G.J. Metzger, P.F. van de Moortele, C. Akgun, C.J. Snyder, S. Moeller, J. Strupp, P. Andersen, D. Shrivastava, T. Vaughan, K. Ugurbil, G. Adriany, Performance of external and internal coil configurations for prostate investigations at 7 T, Magn. Reson. Med. 64 (2010) 1625–1639.

[118] A.J. Raaijmakers, O. Ipek, D.W. Klomp, C. Possanzini, P.R. Harvey, J.J. Lagendijk, C.A. van den Berg, Design of a radiative surface coil array element at 7 T: the single-side adapted dipole antenna, Magn. Reson. Med. 66 (2011) 1488–1497.

[119] B. van den Bergen, D.W. Klomp, A.J. Raaijmakers, C.A. de Castro, V.O. Boer, H. Kroeze, P.R. Luijten, J.J. Lagendijk, C.A. van den Berg, Uniform prostate imaging and spectroscopy at 7 T: comparison between a microstrip array and an endorectal coil, NMR Biomed. 24 (2011) 358–365.

[120] N. Tayari, A. Heerschap, T.W.J. Scheenen, T. Kobus, In vivo MR spectroscopic imaging of the prostate, from application to interpretation, Anal. Biochem. 529 (2017) 158–170.

[121] C.J. Snyder, L. DelaBarre, G.J. Metzger, P.F. van de Moortele, C. Akgun, K. Ugurbil, J.T. Vaughan, Initial results of cardiac imaging at 7 Tesla, Magn. Reson. Med. 61 (2009) 517–524.

[122] A.T. Hess, M.M. Bissell, N.A. Ntusi, A.J. Lewis, E.M. Tunnicliffe, A. Greiser, A.F. Stalder, J.M. Francis, S.G. Myerson, S. Neubauer, M.D. Robson, Aortic 4D flow: quantification of signal-to-noise ratio as a function of field strength and contrast enhancement for 1.5T, 3T, and 7T, Magn. Reson. Med. 73 (2015) 1864–1871.

[123] S. Schmitter, S. Schnell, K. Ugurbil, M. Markl, P.F. Van de Moortele, Towards high-resolution 4D flow MRI in the human aorta using kt-GRAPPA and B1+ shimming at 7T, J. Magn. Reson. Imaging 44 (2016) 486–499.

[124] T. Frauenrath, F. Hezel, W. Renz, G. d'Orth Tde, M. Dieringer, F. von Knobelsdorff-Brenkenhoff, M. Prothmann, J. Schulz Menger, T. Niendorf, Acoustic cardiac triggering: a practical solution for synchronization and gating of cardiovascular magnetic resonance at 7 Tesla, J. Cardiovasc. Magn. Reson. 12 (2010) 67.

[125] A.T. Hess, E.M. Tunnicliffe, C.T. Rodgers, M.D. Robson, Diaphragm position can be accurately estimated from the scattering of a parallel transmit RF coil at 7 T, Magn. Reson. Med. 79 (2018) 2164–2169.

[126] S. Schmitter, X. Wu, K. Ugurbil, P.F. Van de Moortele, Design of parallel transmission radiofrequency pulses robust against respiration in cardiac MRI at 7 Tesla, Magn. Reson. Med. 74 (2015) 1291–1305.

[127] A. Fischer, O. Kraff, S. Maderwald, K. Beiderwellen, M.E. Ladd, M. Forsting, T.C. Lauenstein, L. Umutlu, Non-enhanced T1-weighted liver vessel imaging at 7 Tesla, PLoS One 9 (2014) e97465.

[128] L. Umutlu, A.K. Bitz, S. Maderwald, S. Orzada, S. Kinner, O. Kraff, I. Brote, S.C. Ladd, T. Schroeder, M. Forsting, G. Antoch, M.E. Ladd, H.H. Quick, T.C. Lauenstein, Contrast-enhanced ultra-high-field liver MRI: a feasibility trial, Eur. J. Radiol. 82 (2013) 760–767.

[129] L. Umutlu, O. Kraff, S. Orzada, A. Fischer, S. Kinner, S. Maderwald, G. Antoch, H.H. Quick, M. Forsting, M.E. Ladd, T.C. Lauenstein, Dynamic contrast-enhanced renal MRI at 7 Tesla: preliminary results, Invest. Radiol. 46 (2011) 425–433.

[130] L. Umutlu, S. Maderwald, S. Kinner, O. Kraff, A.K. Bitz, S. Orzada, S. Johst, K. Wrede, M. Forsting, M.E. Ladd, T.C. Lauenstein, H.H. Quick, First-pass contrast-enhanced renal MRA at 7 Tesla: initial results, Eur. Radiol. 23 (2013) 1059–1066.

[131] L. Umutlu, S. Maderwald, O. Kraff, S. Kinner, L.C. Schaefer, K. Wrede, G. Antoch, M. Forsting, M.E. Ladd, T.C. Lauenstein, H.H. Quick, New look at renal vasculature: 7 tesla nonenhanced T1-weighted FLASH imaging, J. Magn. Reson. Imaging 36 (2012) 714–721.

[132] L. Umutlu, S. Orzada, S. Kinner, S. Maderwald, I. Brote, A.K. Bitz, O. Kraff, S.C. Ladd, G. Antoch, M.E. Ladd, H.H. Quick, T.C. Lauenstein, Renal imaging at 7 Tesla: preliminary results, Eur. Radiol. 21 (2011) 841–849.

[133] X. Wu, S. Schmitter, E.J. Auerbach, K. Ugurbil, P.F. Van de Moortele, Mitigating transmit B 1 inhomogeneity in the liver at 7T using multi-spoke parallel transmit RF pulse design, Quant. Imaging Med. Surg. 4 (2014) 4–10.

[134] C.M. Deniz, R. Brown, R. Lattanzi, L. Alon, D.K. Sodickson, Y. Zhu, Maximum efficiency radiofrequency shimming: theory and initial application for hip imaging at 7 tesla, Magn. Reson. Med. 69 (2013) 1379–1388.

[135] A. Lazik-Palm, O. Kraff, S. Johst, H.H. Quick, M.E. Ladd, C. Geis, K. Korsmeier, S. Landgraeber, J.M. Theysohn, Morphological and quantitative 7 T MRI of hip cartilage transplants in comparison to 3 T-initial experiences, Invest. Radiol. 51 (2016) 552–559.

[136] J. Ellermann, U. Goerke, P. Morgan, K. Ugurbil, J. Tian, S. Schmitter, T. Vaughan, P.F. Van De Moortele, Simultaneous bilateral hip joint imaging at 7 Tesla using fast transmit B1 shimming methods and multichannel transmission – a feasibility study, NMR Biomed. 25 (2012) 1202–1208.

[137] J.M. Theysohn, O. Kraff, S. Orzada, N. Theysohn, T. Classen, S. Landgraeber, M. E. Ladd, T.C. Lauenstein, Bilateral hip imaging at 7 Tesla using a multi-channel transmit technology: initial results presenting anatomical detail in healthy volunteers and pathological changes in patients with avascular necrosis of the femoral head, Skeletal Radiol. 42 (2013) 1555–1563.

[138] R. Brown, C.M. Deniz, B. Zhang, G. Chang, D.K. Sodickson, G.C. Wiggins, Design and application of combined 8-channel transmit and 10-channel receive arrays and radiofrequency shimming for 7-T shoulder magnetic resonance imaging, Invest. Radiol. 49 (2014) 35–47.

[139] A. Henning, W. Koning, A. Fuchs, A. Raaijmakers, J.J. Bluemink, C.A. van den Berg, V.O. Boer, D.W. Klomp, 1H MRS in the human spinal cord at 7 T using a dielectric waveguide transmitter, RF shimming and a high density receive array, NMR Biomed. 29 (2016) 1231–1239.

[140] S. By, J.V. Rispoli, S. Cheshkov, I. Dimitrov, J. Cui, S. Seiler, S. Goudreau, C. Malloy, S.M. Wright, M.P. McDougall, A 16-channel receive, forced current excitation dual-transmit coil for breast imaging at 7T, PLoS One 9 (2014) e113969.

[141] M.L. Hahnemann, O. Kraff, S. Maderwald, S. Johst, S. Orzada, L. Umutlu, M.E. Ladd, H.H. Quick, T.C. Lauenstein, Non-enhanced magnetic resonance imaging of the small bowel at 7 Tesla in comparison to 1.5 Tesla: first steps towards clinical application, Magn. Reson. Imaging 34 (2016) 668–673.

[142] A. Fischer, S. Maderwald, S. Johst, S. Orzada, M.E. Ladd, L. Umutlu, T.C. Lauenstein, H.W. Kniemeyer, K. Nassenstein, Initial evaluation of non-contrast-enhanced magnetic resonance angiography in patients with peripheral arterial occlusive disease at 7 T, Invest. Radiol. 49 (2014) 331–338.

[143] S. Johst, S. Maderwald, A. Fischer, H.H. Quick, M.E. Ladd, S. Orzada, Investigation of the saturation pulse artifact in non-enhanced MR

angiography of the lower extremity arteries at 7 Tesla, PLoS One 10 (2015) e0119845.
[144] J. Hoffmann, C. Mirkes, G. Shajan, K. Scheffler, R. Pohmann, Combination of a multimode antenna and TIAMO for traveling-wave imaging at 9.4 Tesla, Magn. Reson. Med. 75 (2016) 452–462.
[145] B.W.J. Philips, A.S. Fortuin, S. Orzada, T.W.J. Scheenen, M.C. Maas, High resolution MR imaging of pelvic lymph nodes at 7 Tesla, Magn. Reson. Med. 78 (2017) 1020–1028.
[146] S. Orzada, A.K. Bitz, O. Kraff, M. Oehmigen, M. Gratz, S. Johst, M.N. Völker, S.H. G. Rietsch, M. Flöser, T. Fiedler, S. Shooshtary, K. Solbach, H.H. Quick, M.E. Ladd, A 32-channel integrated body coil for 7 Tesla whole-body imaging, in: Proceedings 24th Scientific Meeting, International Society for Magnetic Resonance in Medicine, Singapore, 2016, p. 0167.
[147] L. Dupas, A. Massire, A. Amadon, A. Vignaud, N. Boulant, Two-spoke placement optimization under explicit specific absorption rate and power constraints in parallel transmission at ultra-high field, J. Magn. Reson. 255 (2015) 59–67.
[148] V. Gras, A. Vignaud, A. Amadon, F. Mauconduit, D. Le Bihan, N. Boulant, In vivo demonstration of whole-brain multislice multispoke parallel transmit radiofrequency pulse design in the small and large flip angle regimes at 7 Tesla, Magn. Reson. Med. 78 (2017) 1009–1019.
[149] D.H.Y. Tse, C.J. Wiggins, B.A. Poser, High-resolution gradient-recalled echo imaging at 9.4T using 16-channel parallel transmit simultaneous multislice spokes excitations with slice-by-slice flip angle homogenization, Magn. Reson. Med. 78 (2017) 1050–1058.
[150] X. Wu, G. Adriany, K. Ugurbil, P.F. Van de Moortele, Correcting for strong eddy current induced B0 modulation enables two-spoke RF pulse design with parallel transmission: demonstration at 9.4T in the human brain, PLoS One 8 (2013) e78078.
[151] S. Schmitter, L. DelaBarre, X. Wu, A. Greiser, D. Wang, E.J. Auerbach, J.T. Vaughan, K. Ugurbil, P.F. Van de Moortele, Cardiac imaging at 7 Tesla: single- and two-spoke radiofrequency pulse design with 16-channel parallel excitation, Magn. Reson. Med. 70 (2013) 1210–1219.
[152] M.A. Cloos, N. Boulant, M. Luong, G. Ferrand, E. Giacomini, M.F. Hang, C.J. Wiggins, D. Le Bihan, A. Amadon, Parallel-transmission-enabled magnetization-prepared rapid gradient-echo T1-weighted imaging of the human brain at 7 T, Neuroimage 62 (2012) 2140–2150.
[153] S.J. Malik, S. Keihaninejad, A. Hammers, J.V. Hajnal, Tailored excitation in 3D with spiral nonselective (SPINS) RF pulses, Magn. Reson. Med. 67 (2012) 1303–1315.
[154] D.H. Tse, C.J. Wiggins, D. Ivanov, D. Brenner, J. Hoffmann, C. Mirkes, G. Shajan, K. Scheffler, K. Uludag, B.A. Poser, Volumetric imaging with homogenised excitation and static field at 9.4 T, MAGMA 29 (2016) 333–345.
[155] F. Eggenschwiler, K.R. O'Brien, R. Gruetter, J.P. Marques, Improving T2-weighted imaging at high field through the use of kT-points, Magn. Reson. Med. 71 (2014) 1478–1488.
[156] S.J. Malik, A. Beqiri, F. Padormo, J.V. Hajnal, Direct signal control of the steady-state response of 3D-FSE sequences, Magn. Reson. Med. 73 (2015) 951–963.
[157] A. Massire, A. Vignaud, B. Robert, D. Le Bihan, N. Boulant, A. Amadon, Parallel-transmission-enabled three-dimensional T2-weighted imaging of the human brain at 7 Tesla, Magn. Reson. Med. 73 (2015) 2195–2203.
[158] A. Sbrizzi, H. Hoogduin, J.V. Hajnal, C.A. van den Berg, P.R. Luijten, S.J. Malik, Optimal control design of turbo spin-echo sequences with applications to parallel-transmit systems, Magn. Reson. Med. 77 (2017) 361–373.
[159] S.J. Malik, F. Padormo, A.N. Price, J.V. Hajnal, Spatially resolved extended phase graphs: modeling and design of multipulse sequences with parallel transmission, Magn. Reson. Med. 68 (2012) 1481–1494.
[160] S.J. Malik, J.V. Hajnal, Phase relaxed localized excitation pulses for inner volume fast spin echo imaging, Magn. Reson. Med. 76 (2016) 848–861.
[161] R. Mooiweer, A. Sbrizzi, A.J.E. Raaijmakers, C.A.T. van den Berg, P.R. Luijten, H. Hoogduin, Combining a reduced field of excitation with SENSE-based parallel imaging for maximum imaging efficiency, Magn. Reson. Med. 78 (2017) 88–96.
[162] G. Patel, M. Haas, N. Darji, O. Speck, Evaluation of 2D spatially selective MR spectroscopy using parallel excitation at 7 T, Quant. Imaging Med. Surg. 5 (2015) 344–355.
[163] P. Waxmann, R. Mekle, F. Schubert, R. Bruhl, A. Kuehne, T.D. Lindel, F. Seifert, O. Speck, B. Ittermann, A new sequence for shaped voxel spectroscopy in the human brain using 2D spatially selective excitation and parallel transmission, NMR Biomed. 29 (2016) 1028–1037.
[164] V. Gras, M. Boland, A. Vignaud, G. Ferrand, A. Amadon, F. Mauconduit, D. Le Bihan, T. Stocker, N. Boulant, Homogeneous non-selective and slice-selective parallel-transmit excitations at 7 Tesla with universal pulses: a validation study on two commercial RF coils, PLoS One 12 (2017) e0183562.
[165] V. Gras, F. Mauconduit, A. Vignaud, A. Amadon, D. Le Bihan, T. Stocker, N. Boulant, Design of universal parallel-transmit refocusing kT-point pulses and application to 3D T2-weighted imaging at 7T, Magn. Reson. Med. 80 (2018) 53–65.
[166] M.A. Cloos, F. Knoll, T. Zhao, K.T. Block, M. Bruno, G.C. Wiggins, D.K. Sodickson, Multiparametric imaging with heterogeneous radiofrequency fields, Nat. Commun. 7 (2016) 12445.
[167] D. Ma, V. Gulani, N. Seiberlich, K. Liu, J.L. Sunshine, J.L. Duerk, M.A. Griswold, Magnetic resonance fingerprinting, Nature 495 (2013) 187–192.
[168] A. Deshmane, V. Gulani, M.A. Griswold, N. Seiberlich, Parallel MR imaging, J. Magn. Reson. Imaging 36 (2012) 55–72.
[169] J.B. Andre, B.W. Bresnahan, M. Mossa-Basha, M.N. Hoff, C.P. Smith, Y. Anzai, W.A. Cohen, Toward quantifying the prevalence, severity, and cost associated with patient motion during clinical MR examinations, J. Am. Coll. Radiol. 12 (2015) 689–695.
[170] K. Butts, A. de Crespigny, J.M. Pauly, M. Moseley, Diffusion-weighted interleaved echo-planar imaging with a pair of orthogonal navigator echoes, Magn. Reson. Med. 35 (1996) 763–770.
[171] R.L. Ehman, J.P. Felmlee, Adaptive technique for high-definition MR imaging of moving structures, Radiology 173 (1989) 255–263.
[172] Z.W. Fu, Y. Wang, R.C. Grimm, P.J. Rossman, J.P. Felmlee, S.J. Riederer, R.L. Ehman, Orbital navigator echoes for motion measurements in magnetic resonance imaging, Magn. Reson. Med. 34 (1995) 746–753.
[173] H.A. Ward, S.J. Riederer, R.C. Grimm, R.L. Ehman, J.P. Felmlee, C.R. Jack Jr., Prospective multiaxial motion correction for fMRI, Magn. Reson. Med. 43 (2000) 459–469.
[174] M.D. Tisdall, A.T. Hess, M. Reuter, E.M. Meintjes, B. Fischl, A.J. van der Kouwe, Volumetric navigators for prospective motion correction and selective reacquisition in neuroanatomical MRI, Magn. Reson. Med. 68 (2012) 389–399.
[175] N. White, C. Roddey, A. Shankaranarayanan, E. Han, D. Rettmann, J. Santos, J. Kuperman, A. Dale, PROMO: real-time prospective motion correction in MRI using image-based tracking, Magn. Reson. Med. 63 (2010) 91–105.
[176] C. Liu, R. Bammer, D.H. Kim, M.E. Moseley, Self-navigated interleaved spiral (SNAILS): application to high-resolution diffusion tensor imaging, Magn. Reson. Med. 52 (2004) 1388–1396.
[177] J.G. Pipe, Motion correction with PROPELLER MRI: application to head motion and free-breathing cardiac imaging, Magn. Reson. Med. 42 (1999) 963–969.
[178] M. Aksoy, C. Forman, M. Straka, T. Cukur, J. Hornegger, R. Bammer, Hybrid prospective and retrospective head motion correction to mitigate cross-calibration errors, Magn. Reson. Med. 67 (2012) 1237–1251.
[179] J. Maclaren, B.S. Armstrong, R.T. Barrows, K.A. Danishad, T. Ernst, C.L. Foster, K. Gumus, M. Herbst, I.Y. Kadashevich, T.P. Kusik, Q. Li, C. Lovell-Smith, T. Prieto, P. Schulze, O. Speck, D. Stucht, M. Zaitsev, Measurement and correction of microscopic head motion during magnetic resonance imaging of the brain, PLoS One 7 (2012) e48088.
[180] L. Qin, P. van Gelderen, J.A. Derbyshire, F. Jin, J. Lee, J.A. de Zwart, Y. Tao, J. H. Duyn, Prospective head-movement correction for high-resolution MRI using an in-bore optical tracking system, Magn. Reson. Med. 62 (2009) 924–934.
[181] J. Schulz, T. Siegert, E. Reimer, C. Labadie, J. Maclaren, M. Herbst, M. Zaitsev, R. Turner, An embedded optical tracking system for motion-corrected magnetic resonance imaging at 7T, MAGMA 25 (2012) 443–453.
[182] M. Zaitsev, C. Dold, G. Sakas, J. Hennig, O. Speck, Magnetic resonance imaging of freely moving objects: prospective real-time motion correction using an external optical motion tracking system, Neuroimage 31 (2006) 1038–1050.
[183] S. Krueger, T. Schaeffter, S. Weiss, K. Nehrke, T. Rozijn, P. Boernert, Prospective intra-image compensation for non-periodic rigid body motion using active markers, in: Proceedings 14th Scientific Meeting, International Society for Magnetic Resonance in Medicine, Seattle, 2006, p. 3196.
[184] M.B. Ooi, S. Krueger, W.J. Thomas, S.V. Swaminathan, T.R. Brown, Prospective real-time correction for arbitrary head motion using active markers, Magn. Reson. Med. 62 (2009) 943–954.
[185] F. Godenschweger, U. Kagebein, D. Stucht, U. Yarach, A. Sciarra, R. Yakupov, F. Lusebrink, P. Schulze, O. Speck, Motion correction in MRI of the brain, Phys. Med. Biol. 61 (2016) R32–56.
[186] J. Maclaren, M. Herbst, O. Speck, M. Zaitsev, Prospective motion correction in brain imaging: a review, Magn. Reson. Med. 69 (2013) 621–636.
[187] R.B. van Heeswijk, G. Bonanno, S. Coppo, A. Coristine, T. Kober, M. Stuber, Motion compensation strategies in magnetic resonance imaging, Crit. Rev. Biomed. Eng. 40 (2012) 99–119.
[188] M. Zaitsev, J. Maclaren, M. Herbst, Motion artifacts in MRI: a complex problem with many partial solutions, J. Magn. Reson. Imaging 42 (2015) 887–901.
[189] J. Maclaren, O. Speck, D. Stucht, P. Schulze, J. Hennig, M. Zaitsev, Navigator accuracy requirements for prospective motion correction, Magn. Reson. Med. 63 (2010) 162–170.
[190] D. Gallichan, J.P. Marques, R. Gruetter, Retrospective correction of involuntary microscopic head movement using highly accelerated fat image navigators (3D FatNavs) at 7T, Magn. Reson. Med. 75 (2016) 1030–1039.
[191] U. Yarach, C. Luengviriya, A. Danishad, D. Stucht, F. Godenschweger, P. Schulze, O. Speck, Correction of gradient nonlinearity artifacts in prospective motion correction for 7T MRI, Magn. Reson. Med. 73 (2015) 1562–1569.
[192] U. Yarach, C. Luengviriya, D. Stucht, F. Godenschweger, P. Schulze, O. Speck, Correction of B 0-induced geometric distortion variations in prospective motion correction for 7T MRI, MAGMA 29 (2016) 319–332.
[193] C. Federau, D. Gallichan, Motion-correction enabled ultra-high resolution in-vivo 7T-MRI of the brain, PLoS One 11 (2016) e0154974.
[194] B. Zahneisen, B. Keating, A. Singh, M. Herbst, T. Ernst, Reverse retrospective motion correction, Magn. Reson. Med. 75 (2016) 2341–2349.
[195] H. Mattern, A. Sciarra, F. Godenschweger, D. Stucht, F. Lusebrink, G. Rose, O. Speck, Prospective motion correction enables highest resolution time-of-flight angiography at 7T, Magn. Reson. Med. 80 (2018) 248–258.
[196] E.M. Haacke, Y. Xu, Y.C. Cheng, J.R. Reichenbach, Susceptibility weighted imaging (SWI), Magn. Reson. Med. 52 (2004) 612–618.

[197] E.M. Haacke, S. Liu, S. Buch, W. Zheng, D. Wu, Y. Ye, Quantitative susceptibility mapping: current status and future directions, Magn. Reson. Imaging 33 (2015) 1–25.

[198] Y. Wang, T. Liu, Quantitative susceptibility mapping (QSM): decoding MRI data for a tissue magnetic biomarker, Magn. Reson. Med. 73 (2015) 82–101.

[199] C. Liu, H. Wei, N.J. Gong, M. Cronin, R. Dibb, K. Decker, Quantitative susceptibility mapping: contrast mechanisms and clinical applications, Tomography 1 (2015) 3–17.

[200] A.M. Abduljalil, P. Schmalbrock, V. Novak, D.W. Chakeres, Enhanced gray and white matter contrast of phase susceptibility-weighted images in ultra-high-field magnetic resonance imaging, J. Magn. Reson. Imaging 18 (2003) 284–290.

[201] J.H. Duyn, P. van Gelderen, T.Q. Li, J.A. de Zwart, A.P. Koretsky, M. Fukunaga, High-field MRI of brain cortical substructure based on signal phase, Proc. Natl. Acad. Sci. USA 104 (2007) 11796–11801.

[202] A.M. Peters, M.J. Brookes, F.G. Hoogenraad, P.A. Gowland, S.T. Francis, P.G. Morris, R. Bowtell, T2* measurements in human brain at 1.5, 3 and 7 T, Magn. Reson. Imaging 25 (2007) 748–753.

[203] M. Fukunaga, T.Q. Li, P. van Gelderen, J.A. de Zwart, K. Shmueli, B. Yao, J. Lee, D. Maric, M.A. Aronova, G.F. Zhang, R.D. Leapman, J.F. Schenck, H. Merkle, J.H. Duyn, Layer-specific variation of iron content in cerebral cortex as a source of MRI contrast, Proc. Natl. Acad. Sci. USA 107 (2010) 3834–3839.

[204] C. Langkammer, F. Schweser, N. Krebs, A. Deistung, W. Goessler, E. Scheurer, K. Sommer, G. Reishofer, K. Yen, F. Fazekas, S. Ropele, J.R. Reichenbach, Quantitative susceptibility mapping (QSM) as a means to measure brain iron? A post mortem validation study, Neuroimage 62 (2012) 1593–1599.

[205] S. Wharton, R. Bowtell, Effects of white matter microstructure on phase and susceptibility maps, Magn. Reson. Med. 73 (2015) 1258–1269.

[206] S. Wharton, R. Bowtell, Fiber orientation-dependent white matter contrast in gradient echo MRI, Proc. Natl. Acad. Sci. USA 109 (2012) 18559–18564.

[207] X. Li, D.S. Vikram, I.A.L. Lim, C.K. Jones, J.A.D. Farrell, P.C.M. van Zijl, Mapping magnetic susceptibility anisotropies of white matter in vivo in the human brain at 7 T, Neuroimage 62 (2012) 314–330.

[208] W. Li, B. Wu, C. Liu, Quantitative susceptibility mapping of human brain reflects spatial variation in tissue composition, Neuroimage 55 (2011) 1645–1656.

[209] J. Lee, K. Shmueli, M. Fukunaga, P. van Gelderen, H. Merkle, A.C. Silva, J.H. Duyn, Sensitivity of MRI resonance frequency to the orientation of brain tissue microstructure, Proc. Natl. Acad. Sci. USA 107 (2010) 5130–5135.

[210] A.L. Sukstanskii, D.A. Yablonskiy, On the role of neuronal magnetic susceptibility and structure symmetry on gradient echo MR signal formation, Magn. Reson. Med. 71 (2014) 345–353.

[211] K. Zhong, J. Leupold, D. von Elverfeldt, O. Speck, The molecular basis for gray and white matter contrast in phase imaging, Neuroimage 40 (2008) 1561–1566.

[212] S. Sood, J. Urriola, D. Reutens, K. O'Brien, S. Bollmann, M. Barth, V. Vegh, Echo time-dependent quantitative susceptibility mapping contains information on tissue properties, Magn. Reson. Med. 77 (2017) 1946–1958.

[213] J.P. Marques, D. Khabipova, R. Gruetter, Studying cyto and myeloarchitecture of the human cortex at ultra-high field with quantitative imaging: R1, R2* and magnetic susceptibility, Neuroimage 147 (2017) 152–163.

[214] S. Wang, T. Liu, W.W. Chen, P. Spincemaille, C. Wisnieff, A.J. Tsiouris, W.Z. Zhu, C. Pan, L.Y. Zhao, Y. Wang, Noise effects in various quantitative susceptibility mapping methods, IEEE Trans. Biomed. Eng. 60 (2013) 3441–3448.

[215] E.M. Haacke, S. Mittal, Z. Wu, J. Neelavalli, Y.C. Cheng, Susceptibility-weighted imaging: technical aspects and clinical applications, part 1, AJNR Am. J. Neuroradiol. 30 (2009) 19–30.

[216] A. Deistung, A. Rauscher, J. Sedlacik, J. Stadler, S. Witoszynskyj, J.R. Reichenbach, Susceptibility weighted imaging at ultra high magnetic field strengths: theoretical considerations and experimental results, Magn. Reson. Med. 60 (2008) 1155–1168.

[217] B. Bilgic, B.A. Gagoski, S.F. Cauley, A.P. Fan, J.R. Polimeni, P.E. Grant, L.L. Wald, K. Setsompop, Wave-CAIPI for highly accelerated 3D imaging, Magn. Reson. Med. 73 (2015) 2152–2162.

[218] D. Stab, S. Bollmann, C. Langkammer, K. Bredies, M. Barth, Accelerated mapping of magnetic susceptibility using 3D planes-on-a-paddlewheel (POP) EPI at ultra-high field strength, NMR Biomed. 30 (2017).

[219] S.D. Robinson, K. Bredies, D. Khabipova, B. Dymerska, J.P. Marques, F. Schweser, An illustrated comparison of processing methods for MR phase imaging and QSM: combining array coil signals and phase unwrapping, NMR Biomed. 30 (2017).

[220] F. Schweser, S.D. Robinson, L. de Rochefort, W. Li, K. Bredies, An illustrated comparison of processing methods for phase MRI and QSM: removal of background field contributions from sources outside the region of interest, NMR Biomed. 30 (2017).

[221] T. Liu, W. Xu, P. Spincemaille, A.S. Avestimehr, Y. Wang, Accuracy of the morphology enabled dipole inversion (MEDI) algorithm for quantitative susceptibility mapping in MRI, IEEE Trans. Med. Imaging 31 (2012) 816–824.

[222] F. Schweser, K. Sommer, A. Deistung, J.R. Reichenbach, Quantitative susceptibility mapping for investigating subtle susceptibility variations in the human brain, Neuroimage 62 (2012) 2083–2100.

[223] K. Shmueli, J.A. de Zwart, P. van Gelderen, T.Q. Li, S.J. Dodd, J.H. Duyn, Magnetic susceptibility mapping of brain tissue in vivo using MRI phase data, Magn. Reson. Med. 62 (2009) 1510–1522.

[224] S. Wharton, A. Schafer, R. Bowtell, Susceptibility mapping in the human brain using threshold-based k-space division, Magn. Reson. Med. 63 (2010) 1292–1304.

[225] B. Wu, W. Li, A. Guidon, C. Liu, Whole brain susceptibility mapping using compressed sensing, Magn. Reson. Med. 67 (2012) 137–147.

[226] A. Abosch, E. Yacoub, K. Ugurbil, N. Harel, An assessment of current brain targets for deep brain stimulation surgery with susceptibility-weighted imaging at 7 tesla, Neurosurgery 67 (2010) 1745–1756.

[227] A. Schafer, B.U. Forstmann, J. Neumann, S. Wharton, A. Mietke, R. Bowtell, R. Turner, Direct visualization of the subthalamic nucleus and its iron distribution using high-resolution susceptibility mapping, Hum. Brain Mapp. 33 (2012) 2831–2842.

[228] S. Maderwald, M. Thurling, M. Kuper, N. Theysohn, O. Muller, A. Beck, V. Aurich, M.E. Ladd, D. Timmann, Direct visualization of cerebellar nuclei in patients with focal cerebellar lesions and its application for lesion-symptom mapping, Neuroimage 63 (2012) 1421–1431.

[229] A. Deistung, A. Schafer, F. Schweser, U. Biedermann, R. Turner, J.R. Reichenbach, Toward in vivo histology: A comparison of quantitative susceptibility mapping (QSM) with magnitude-, phase-, and R-2*-imaging at ultra-high magnetic field strength, Neuroimage 65 (2013) 299–314.

[230] G. Schaltenbrand, W. Wahren, R. Hassler, Atlas for Stereotaxy of the Human Brain, 1977.

[231] A. Deistung, A. Schafer, F. Schweser, U. Biedermann, D. Gullmar, R. Trampel, R. Turner, J.R. Reichenbach, High-resolution MR imaging of the human brainstem in vivo at 7 Tesla, Front. Hum. Neurosci. 7 (2013).

[232] K. Amunts, C. Lepage, L. Borgeat, H. Mohlberg, T. Dickscheid, M.E. Rousseau, S. Bludau, P.L. Bazin, L.B. Lewis, A.M. Oros-Peusquens, N.J. Shah, T. Lippert, K. Zilles, A.C. Evans, BigBrain: an ultrahigh-resolution 3D human brain model, Science 340 (2013) 1472–1475.

[233] M. Cosottini, D. Frosini, I. Pesaresi, G. Donatelli, P. Cecchi, M. Costagli, L. Biagi, R. Ceravolo, U. Bonuccelli, M. Tosetti, Comparison of 3T and 7T susceptibility-weighted angiography of the substantia nigra in diagnosing Parkinson disease, Am. J. Neuroradiol. 36 (2015) 461–466.

[234] B.R. Plantinga, Y. Temel, A. Roebroeck, K. Uludag, D. Ivanov, M.L. Kuijf, B.M. Ter Haar Romenij, Ultra-high field magnetic resonance imaging of the basal ganglia and related structures, Front. Hum. Neurosci. 8 (2014) 876.

[235] R.M. Weisskoff, S. Kiihne, MRI susceptometry: image-based measurement of absolute susceptibility of MR contrast agents and human blood, Magn. Reson. Med. 24 (1992) 375–383.

[236] J.F. Schenck, Health and physiological effects of human exposure to whole-body four-tesla magnetic fields during MRI, Ann. N. Y. Acad. Sci. 649 (1992) 285–301.

[237] A.P. Fan, A. Schafer, L. Huber, L. Lampe, S. von Smuda, H.E. Moller, A. Villringer, C.J. Gauthier, Baseline oxygenation in the brain: correlation between respiratory-calibration and susceptibility methods, Neuroimage 125 (2016) 920–931.

[238] S. Monti, S. Cocozza, P. Borrelli, S. Straub, M.E. Ladd, M. Salvatore, E. Tedeschi, G. Palma, MAVEN: an algorithm for multi-parametric automated segmentation of brain veins from gradient echo acquisitions, IEEE Trans. Med. Imaging 36 (2017) 1054–1065.

[239] B.P. Thomas, E.B. Welch, B.D. Niederhauser, W.O. Whetsell Jr., A.W. Anderson, J.C. Gore, M.J. Avison, J.L. Creasy, High-resolution 7T MRI of the human hippocampus in vivo, J. Magn. Reson. Imaging 28 (2008) 1266–1272.

[240] A. Di Ieva, M. Tschabitscher, R.J. Galzio, G. Grabner, C. Kronnerwetter, G. Widhalm, C. Matula, S. Trattnig, The veins of the nucleus dentatus: anatomical and radiological findings, Neuroimage 54 (2011) 74–79.

[241] Y.B. Lee, Y.B. Seo, C.A. Park, C.K. Kang, Imaging method for changes in venous dynamics: a preliminary study, Neuroreport 26 (2015) 333–340.

[242] D.Z. Balla, R.M. Sanchez-Panchuelo, S.J. Wharton, G.E. Hagberg, K. Scheffler, S.T. Francis, R. Bowtell, Functional quantitative susceptibility mapping (fQSM), Neuroimage 100 (2014) 112–124.

[243] S. Buch, Y.N. Cheng, J. Hu, S. Liu, J. Beaver, R. Rajagovindan, E.M. Haacke, Determination of detection sensitivity for cerebral microbleeds using susceptibility-weighted imaging, NMR Biomed. 30 (2017).

[244] J.M. Theysohn, O. Kraff, S. Maderwald, M. Barth, S.C. Ladd, M. Forsting, M.E. Ladd, E.R. Gizewski, 7 Tesla MRI of microbleeds and white matter lesions as seen in vascular dementia, J. Magn. Reson. Imag. 33 (2011) 782–791.

[245] A. Deistung, F. Schweser, B. Wiestler, M. Abello, M. Roethke, F. Sahm, W. Wick, A.M. Nagel, S. Heiland, H.P. Schlemmer, M. Bendszus, J.R. Reichenbach, A. Radbruch, Quantitative susceptibility mapping differentiates between blood depositions and calcifications in patients with glioblastoma, PLoS One 8 (2013).

[246] J.M. Lupo, C.F. Chuang, S.M. Chang, I.J. Barani, B. Jimenez, C.P. Hess, S.J. Nelson, 7-Tesla susceptibility-weighted imaging to assess the effects of radiotherapy on normal-appearing brain in patients with glioma, Int. J. Radiat. Oncol. Biol. Phys. 82 (2012) E493–E500.

[247] A. Dal-Bianco, S. Hametner, G. Grabner, M. Schernthaner, C. Kronnerwetter, A. Reitner, C. Vass, K. Kircher, E. Auff, F. Leutmezer, K. Vass, S. Trattnig, Veins in plaques of multiple sclerosis patients – a longitudinal magnetic resonance imaging study at 7 Tesla, Eur. Radiol. 25 (2015) 2913–2920.

[248] S. Chawla, I. Kister, J. Wuerfel, J.C. Brisset, S. Liu, T. Sinnecker, P. Dusek, E.M. Haacke, F. Paul, Y. Ge, Iron and non-iron-related characteristics of multiple sclerosis and neuromyelitis optica lesions at 7T MRI, AJNR Am. J. Neuroradiol. 37 (2016) 1223–1230.

[249] M. Absinta, P. Sati, M. Schindler, E.C. Leibovitch, J. Ohayon, T.X. Wu, A. Meani, M. Filippi, S. Jacobson, I.C.M. Cortese, D.S. Reich, Persistent 7-tesla phase rim

predicts poor outcome in new multiple sclerosis patient lesions, J. Clin. Invest. 126 (2016) 2597–2609.

[250] P. Schmalbrock, R.S. Prakash, B. Schirda, A. Janssen, G.K. Yang, M. Russell, M.V. Knopp, A. Boster, J.A. Nicholas, M. Racke, D. Pitt, Basal ganglia iron in patients with multiple sclerosis measured with 7T quantitative susceptibility mapping correlates with inhibitory control, AJNR Am. J. Neuroradiol. 37 (2016) 439–446.

[251] M.J. Cronin, S. Wharton, A. Al-Radaideh, C. Constantinescu, N. Evangelou, R. Bowtell, P.A. Gowland, A comparison of phase imaging and quantitative susceptibility mapping in the imaging of multiple sclerosis lesions at ultrahigh field, Magn. Reson. Mater. Phys., Biol. Med. 29 (2016) 543–557.

[252] W. Bian, E. Tranvinh, T. Tourdias, M. Han, T. Liu, Y. Wang, B. Rutt, M.M. Zeineh, In vivo 7T MR quantitative susceptibility mapping reveals opposite susceptibility contrast between cortical and white matter lesions in multiple sclerosis, Am. J. Neuroradiol. 37 (2016) 1808–1815.

[253] M.A. Smith, P.L.R. Harris, L.M. Sayre, G. Perry, Iron accumulation in Alzheimer disease is a source of redox-generated free radicals, Proc. Natl. Acad. Sci. USA 94 (1997) 9866–9868.

[254] S. van Rooden, M.J. Versluis, M.K. Liem, J. Milles, A.B. Maier, A.M. Oleksik, A.G. Webb, M.A. van Buchem, J. van der Grond, Cortical phase changes in Alzheimer's disease at 7T MRI: a novel imaging marker, Alzheimers Dement 10 (2014) e19–26.

[255] J.M.G. van Bergen, J. Hua, P.G. Unschuld, I.A.L. Lim, C.K. Jones, R.L. Margolis, C. A. Ross, P.C.M. van Zijl, X. Li, Quantitative susceptibility mapping suggests altered brain iron in premanifest Huntington disease, Am. J. Neuroradiol. 37 (2016) 789–796.

[256] C. Thalhammer, W. Renz, L. Winter, F. Hezel, J. Rieger, H. Pfeiffer, A. Graessl, F. Seifert, W. Hoffmann, F. von Knobelsdorff-Brenkenhoff, V. Tkachenko, J. Schulz-Menger, P. Kellman, T. Niendorf, Two-dimensional sixteen channel transmit/receive coil array for cardiac MRI at 7.0 T: design, evaluation, and application, J. Magn. Reson. Imaging 36 (2012) 847–857.

[257] T. Hülnhagen, F. Hezel, T. Niendorf, Toward probing myocardial microstructure using susceptibility sensitized MRI of the human heart at 7.0 T: assessment and implications of static magnetic field variations, in: Proceedings of the 3rd International Workshop on MRI Phase Contrast & Quantitative Susceptibility Mapping, Duke University, Durham, NC, USA, 2013.

[258] H. Wei, R. Dibb, K. Decker, N. Wang, Y. Zhang, X. Zong, W. Lin, D.B. Nissman, C. Liu, Investigating magnetic susceptibility of human knee joint at 7 Tesla, Magn. Reson. Med. 78 (2017) 1933–1943.

[259] J.W. Pan, K.M. Lo, H.P. Hetherington, Role of very high order and degree B0 shimming for spectroscopic imaging of the human brain at 7 tesla, Magn. Reson. Med. 68 (2012) 1007–1017.

[260] S.B. Reeder, C.A. McKenzie, A.R. Pineda, H.Z. Yu, A. Shimakawa, A.C. Brau, B.A. Hargreaves, G.E. Gold, J.H. Brittain, Water-fat separation with IDEAL gradient-echo imaging, J. Magn. Reson. Imaging 25 (2007) 644–652.

[261] S.D. Sharma, D. Hernando, D.E. Horng, S.B. Reeder, Quantitative susceptibility mapping in the abdomen as an imaging biomarker of hepatic iron overload, Magn. Reson. Med. 74 (2015) 673–683.

[262] A.M. Nagel, X-nuclei MRI at UHF, in: Workshop on Ultra High Field MRI: Technological Advances & Clinical Applications, International Society for Magnetic Resonance in Medicine, Heidelberg, 2016.

[263] A.M. Nagel, Sodium MRI in the clinic: what you can learn from a 10 min scan, in: Proceedings 25th Scientific Meeting, International Society for Magnetic Resonance in Medicine, Honolulu, 2017.

[264] R.K. Harris, E.D. Becker, S.M. Cabral de Menezes, R. Goodfellow, P. Granger, NMR nomenclature: nuclear spin properties and conventions for chemical shifts. IUPAC Recommendations 2001. International Union of Pure and Applied Chemistry. Physical Chemistry Division. Commission on Molecular Structure and Spectroscopy, Magn. Reson. Chem. 40 (2002) 489–505.

[265] H. Neeb, K. Zilles, N.J. Shah, A new method for fast quantitative mapping of absolute water content in vivo, Neuroimage 31 (2006) 1156–1168.

[266] A. Moreno, S. Bluml, J.H. Hwang, B.D. Ross, Alternative 1-13C glucose infusion protocols for clinical 13C MRS examinations of the brain, Magn. Reson. Med. 46 (2001) 39–48.

[267] J. Ruiz-Cabello, B.P. Barnett, P.A. Bottomley, J.W. Bulte, Fluorine (19F) MRS and MRI in biomedicine, NMR Biomed. 24 (2011) 114–129.

[268] H.P. Hetherington, D.D. Spencer, J.T. Vaughan, J.W. Pan, Quantitative 31P spectroscopic imaging of human brain at 4 Tesla: assessment of gray and white matter differences of phosphocreatine and ATP, Magn. Reson. Med. 45 (2001) 46–52.

[269] S.C. Niesporek, S.H. Hoffmann, M.C. Berger, N. Benkhedah, A. Kujawa, P. Bachert, A.M. Nagel, Partial volume correction for in vivo 23Na-MRI data of the human brain, Neuroimage 112 (2015) 353–363.

[270] G. Madelin, J.S. Lee, R.R. Regatte, A. Jerschow, Sodium MRI: methods and applications, Prog. Nucl. Magn. Reson. Spectrosc. 79 (2014) 14–47.

[271] A.M. Nagel, F. Lehmann-Horn, M.A. Weber, K. Jurkat-Rott, M.B. Wolf, A. Radbruch, R. Umathum, W. Semmler, In vivo 35Cl MR imaging in humans: a feasibility study, Radiology 271 (2014) 585–595.

[272] R. Umathum, M.B. Rosler, A.M. Nagel, In vivo 39K MR imaging of human muscle and brain, Radiology 269 (2013) 569–576.

[273] S.C. Niesporek, R. Umathum, J.M. Lommen, N.G.R. Behl, D. Paech, P. Bachert, M.E. Ladd, A.M. Nagel, Reproducibility of CMRO2 determination using dynamic 17O MRI, Magn. Reson. Med. 79 (2018) 2923–2934.

[274] D.I. Hoult, P.C. Lauterbur, The sensitivity of the zeugmatographic experiment involving human samples, J. Magn. Reson. 34 (1979) (1969) 425–433.

[275] T.F. Budinger, M.D. Bird, L. Frydman, J.R. Long, T.H. Mareci, W.D. Rooney, B. Rosen, J.F. Schenck, V.D. Schepkin, A.D. Sherry, D.K. Sodickson, C.S. Springer, K.R. Thulborn, K. Ugurbil, L.L. Wald, Toward 20 T magnetic resonance for human brain studies: opportunities for discovery and neuroscience rationale, Magn. Reson. Mater. Phys., Biol. Med. 29 (2016) 617–639.

[276] T.F. Budinger, M.D. Bird, MRI and MRS of the human brain at magnetic fields of 14T to 20T: technical feasibility, safety, and neuroscience horizons, Neuroimage 168 (2018) 509–531.

[277] R.A. de Graaf, P.B. Brown, S. McIntyre, T.W. Nixon, K.L. Behar, D.L. Rothman, High magnetic field water and metabolite proton T1 and T2 relaxation in rat brain in vivo, Magn. Reson. Med. 56 (2006) 386–394.

[278] J.L. Sudmeier, S.E. Anderson, J. Frye, Calculation of nuclear spin relaxation times, Concepts Magn. Reson. (1990) 197–212.

[279] C.T. Rodgers, W.T. Clarke, C. Snyder, J.T. Vaughan, S. Neubauer, M.D. Robson, Human cardiac 31P magnetic resonance spectroscopy at 7 Tesla, Magn. Reson. Med. 72 (2014) 304–315.

[280] A.M. Nagel, R. Umathum, M.B. Rosler, M.E. Ladd, I. Litvak, P.L. Gor'kov, W.W. Brey, V.D. Schepkin, 39K and 23Na relaxation times and MRI of rat head at 21.1 T, NMR Biomed. 29 (2016) 759–766.

[281] R. Stobbe, C. Beaulieu, In vivo sodium magnetic resonance imaging of the human brain using soft inversion recovery fluid attenuation, Magn. Reson. Med. 54 (2005) 1305–1310.

[282] A.M. Nagel, M. Bock, C. Hartmann, L. Gerigk, J.O. Neumann, M.A. Weber, M. Bendszus, A. Radbruch, W. Wick, H.P. Schlemmer, W. Semmler, A. Biller, The potential of relaxation-weighted sodium magnetic resonance imaging as demonstrated on brain tumors, Invest. Radiol. 46 (2011) 539–547.

[283] A.M. Nagel, S. Schmitter, M. Bock, E. Moser, W. Semmler, L.R. Schad, Parameter optimization for 7T 23Na-MRI, in: Proceedings 17th Scientific Meeting, International Society for Magnetic Resonance in Medicine, Honolulu, 2009, p. 2465.

[284] A.M. Nagel, F.B. Laun, M.A. Weber, C. Matthies, W. Semmler, L.R. Schad, Sodium MRI using a density-adapted 3D radial acquisition technique, Magn. Reson. Med. 62 (2009) 1565–1573.

[285] N.G. Behl, C. Gnahm, P. Bachert, M.E. Ladd, A.M. Nagel, Three-dimensional dictionary-learning reconstruction of 23Na MRI data, Magn. Reson. Med. 75 (2016) 1605–1616.

[286] N. Benkhedah, S.H. Hoffmann, A. Biller, A.M. Nagel, Evaluation of adaptive combination of 30-channel head receive coil array data in 23Na MR imaging, Magn. Reson. Med. 75 (2016) 527–536.

[287] O. Kraff, A. Fischer, A.M. Nagel, C. Monninghoff, M.E. Ladd, MRI at 7 Tesla and above: demonstrated and potential capabilities, J. Magn. Reson. Imaging 41 (2015) 13–33.

[288] S. Haneder, S. Konstandin, J.N. Morelli, A.M. Nagel, F.G. Zoellner, L.R. Schad, S. O. Schoenberg, H.J. Michaely, Quantitative and qualitative 23Na MR imaging of the human kidneys at 3 T: before and after a water load, Radiology 260 (2011) 857–865.

[289] D. Hausmann, S. Konstandin, F. Wetterling, S. Haneder, A.M. Nagel, D.J. Dinter, S.O. Schonberg, F.G. Zollner, L.R. Schad, Apparent diffusion coefficient and sodium concentration measurements in human prostate tissue via hydrogen-1 and sodium-23 magnetic resonance imaging in a clinical setting at 3T, Invest. Radiol. 47 (2012) 677–682.

[290] F. Wetterling, D.M. Corteville, R. Kalayciyan, A. Rennings, S. Konstandin, A.M. Nagel, H. Stark, L.R. Schad, Whole body sodium MRI at 3T using an asymmetric birdcage resonator and short echo time sequence: first images of a male volunteer, Phys. Med. Biol. 57 (2012) 4555–4567.

[291] J. Loring, W.J. van der Kemp, S. Almujayyaz, J.W. van Oorschot, P.R. Luijten, D. W. Klomp, Whole-body radiofrequency coil for 31P MRSI at 7 T, NMR Biomed. 29 (2016) 709–720.

[292] T. Platt, R. Umathum, T.M. Fiedler, A.M. Nagel, A.K. Bitz, F. Maier, P. Bachert, M.E. Ladd, M.O. Wielputz, H.U. Kauczor, N.G.R. Behl, In vivo self-gated 23Na MRI at 7 T using an oval-shaped body resonator, Magn. Reson. Med. (2018).

[293] S. Haneder, V. Juras, H.J. Michaely, X. Deligianni, O. Bieri, S.O. Schoenberg, S. Trattnig, S. Zbyn, In vivo sodium 23Na imaging of the human kidneys at 7 T: preliminary results, Eur. Radiol. 24 (2014) 494–501.

[294] A. Graessl, A. Ruehle, H. Waiczies, A. Resetar, S.H. Hoffmann, J. Rieger, F. Wetterling, L. Winter, A.M. Nagel, T. Niendorf, Sodium MRI of the human heart at 7.0 T: preliminary results, NMR Biomed. 28 (2015) 967–975.

[295] P.B. Roemer, W.A. Edelstein, C.E. Hayes, S.P. Souza, O.M. Mueller, The NMR phased array, Magn. Reson. Med. 16 (1990) 192–225.

[296] G. Shajan, C. Mirkes, K. Buckenmaier, J. Hoffmann, R. Pohmann, K. Scheffler, Three-layered radio frequency coil arrangement for sodium MRI of the human brain at 9.4 Tesla, Magn. Reson. Med. 75 (2016) 906–916.

[297] Y. Qian, T. Zhao, G.C. Wiggins, L.L. Wald, H. Zheng, J. Weimer, F.E. Boada, Sodium imaging of human brain at 7 T with 15-channel array coil, Magn. Reson. Med. 68 (2012) 1807–1814.

[298] J.M. Lommen, F. Resmer, N.G.R. Behl, M. Sauer, N. Benkhedah, A.K. Bitz, R. Umathum, M.E. Ladd, T. Lanz, A.M. Nagel, Comparison of of a 30-channel head array with a birdcage for 23Na MRI at 7 Tesla, in: Proceedings 24th Scientific Meeting, International Society for Magnetic Resonance in Medicine, Singapore, 2016, p. 3974.

[299] G.C. Wiggins, R. Brown, K. Lakshmanan, High-performance radiofrequency coils for 23Na MRI: brain and musculoskeletal applications, NMR Biomed. 29 (2016) 96–106.

[300] N.K. Bangerter, J.D. Kaggie, M.D. Taylor, J.R. Hadley, Sodium MRI radiofrequency coils for body imaging, NMR Biomed. 29 (2016) 107–118.

[301] B.L. van de Bank, S. Orzada, F. Smits, M.W. Lagemaat, C.T. Rodgers, A.K. Bitz, T. W. Scheenen, Optimized 31P MRS in the human brain at 7 T with a dedicated RF coil setup, NMR Biomed. 28 (2015) 1570–1578.

[302] P.W. de Bruin, P. Koken, M.J. Versluis, S.A. Aussenhofer, I. Meulenbelt, P. Bornert, A.G. Webb, Time-efficient interleaved human 23Na and 1H data acquisition at 7 T, NMR Biomed. 28 (2015) 1228–1235.

[303] M. Meyerspeer, A.W. Magill, A. Kuehne, R. Gruetter, E. Moser, A.I. Schmid, Simultaneous and interleaved acquisition of NMR signals from different nuclei with a clinical MRI scanner, Magn. Reson. Med. 76 (2016) 1636–1641.

[304] S.W. Lee, S.K. Hilal, Z.H. Cho, A multinuclear magnetic resonance imaging technique – simultaneous proton and sodium imaging, Magn. Reson. Imaging 4 (1986) 343–350.

[305] J. Lommen, S. Konstandin, P. Kramer, L.R. Schad, Enhancing the quantification of tissue sodium content by MRI: time-efficient sodium B1 mapping at clinical field strengths, NMR Biomed. 29 (2016) 129–136.

[306] A. Lu, I.C. Atkinson, T.C. Claiborne, F.C. Damen, K.R. Thulborn, Quantitative sodium imaging with a flexible twisted projection pulse sequence, Magn. Reson. Med. 63 (2010) 1583–1593.

[307] S. Konstandin, A.M. Nagel, Measurement techniques for magnetic resonance imaging of fast relaxing nuclei, Magn. Reson. Mater. Phys., Biol. Med. 27 (2014) 5–19.

[308] S. Konstandin, A.M. Nagel, P.M. Heiler, L.R. Schad, Two-dimensional radial acquisition technique with density adaption in sodium MRI, Magn. Reson. Med. 65 (2011) 1090–1096.

[309] S. Konstandin, A.M. Nagel, Performance of sampling density-weighted and postfiltered density-adapted projection reconstruction in sodium magnetic resonance imaging, Magn. Reson. Med. 69 (2013) 495–502.

[310] F.E. Boada, J.S. Gillen, G.X. Shen, S.Y. Chang, K.R. Thulborn, Fast three dimensional sodium imaging, Magn. Reson. Med. 37 (1997) 706–715.

[311] I.C. Atkinson, A. Lu, K.R. Thulborn, Clinically constrained optimization of flexTPI acquisition parameters for the tissue sodium concentration bioscale, Magn. Reson. Med. 66 (2011) 1089–1099.

[312] P.T. Gurney, B.A. Hargreaves, D.G. Nishimura, Design and analysis of a practical 3D cones trajectory, Magn. Reson. Med. 55 (2006) 575–582.

[313] J.G. Pipe, N.R. Zwart, E.A. Aboussouan, R.K. Robison, A. Devaraj, K.O. Johnson, A new design and rationale for 3D orthogonally oversampled k-space trajectories, Magn. Reson. Med. 66 (2011) 1303–1311.

[314] C.T. Rodgers, M.D. Robson, Coil combination for receive array spectroscopy: are data-driven methods superior to methods using computed field maps?, Magn Reson. Med. 75 (2016) 473–487.

[315] K.P. Pruessmann, M. Weiger, M.B. Scheidegger, P. Boesiger, SENSE: sensitivity encoding for fast MRI, Magn. Reson. Med. 42 (1999) 952–962.

[316] S.C. Niesporek, R. Umathum, T.M. Fiedler, P. Bachert, M.E. Ladd, A.M. Nagel, Improved T^*_2 determination in 23Na, 35Cl, and 17O MRI using iterative partial volume correction based on 1H MRI segmentation, MAGMA 30 (2017) 519–536.

[317] C. Gnahm, M. Bock, P. Bachert, W. Semmler, N.G. Behl, A.M. Nagel, Iterative 3D projection reconstruction of 23Na data with an 1H MRI constraint, Magn. Reson. Med. 71 (2014) 1720–1732.

[318] C. Gnahm, A.M. Nagel, Anatomically weighted second-order total variation reconstruction of 23Na MRI using prior information from 1H MRI, Neuroimage 105 (2015) 452–461.

[319] E.J. Candes, J. Romberg, T. Tao, Robust uncertainty principles: Exact signal reconstruction from highly incomplete frequency information, IEEE T Inform Theory 52 (2006) 489–509.

[320] D.L. Donoho, Compressed sensing, IEEE Trans. Inform Theory 52 (2006) 1289–1306.

[321] G. Madelin, G. Chang, R. Otazo, A. Jerschow, R.R. Regatte, Compressed sensing sodium MRI of cartilage at 7T: preliminary study, J. Magn. Reson. 214 (2012) 360–365.

[322] T. Kampf, A. Fischer, T.C. Basse-Lusebrink, G. Ladewig, F. Breuer, G. Stoll, P.M. Jakob, W.R. Bauer, Application of compressed sensing to in vivo 3D 19F CSI, J. Magn. Reson. 207 (2010) 262–273.

[323] R. Stobbe, C. Beaulieu, Sodium imaging optimization under specific absorption rate constraint, Magn. Reson. Med. 59 (2008) 345–355.

[324] D. Idiyatullin, C. Corum, J.-Y. Park, M. Garwood, Fast and quiet MRI using a swept radiofrequency, J. Magn. Reson. 181 (2006) 342–349.

[325] M.C. Koch, K. Steinmeyer, C. Lorenz, K. Ricker, F. Wolf, M. Otto, B. Zoll, F. Lehmann-Horn, K.H. Grzeschik, T.J. Jentsch, The skeletal muscle chloride channel in dominant and recessive human myotonia, Science 257 (1992) 797–800.

[326] P. Boulenguez, S. Liabeuf, R. Bos, H. Bras, C. Jean-Xavier, C. Brocard, A. Stil, P. Darbon, D. Cattaert, E. Delpire, M. Marsala, L. Vinay, Down-regulation of the potassium-chloride cotransporter KCC2 contributes to spasticity after spinal cord injury, Nat. Med. 16 (2010) 302–307.

[327] T.J. Jentsch, V. Stein, F. Weinreich, A.A. Zdebik, Molecular structure and physiological function of chloride channels, Physiol. Rev. 82 (2002) 503–568.

[328] V.A. Cuddapah, H. Sontheimer, Ion channels and transporters [corrected] in cancer. 2. Ion channels and the control of cancer cell migration, Am. J. Physiol. Cell Physiol. 301 (2011) C541–549.

[329] C.W. Habela, N.J. Ernest, A.F. Swindall, H. Sontheimer, Chloride accumulation drives volume dynamics underlying cell proliferation and migration, J. Neurophysiol. 101 (2009) 750–757.

[330] S.K. Hilal, A.A. Maudsley, J.B. Ra, H.E. Simon, P. Roschmann, S. Wittekoek, Z.H. Cho, S.K. Mun, In vivo NMR imaging of sodium-23 in the human head, J. Comput. Assist. Tomogr. 9 (1985) 1–7.

[331] I.C. Atkinson, T.C. Claiborne, K.R. Thulborn, Feasibility of 39-potassium MR imaging of a human brain at 9.4 Tesla, Magn. Reson. Med. 71 (2014) 1819–1825.

[332] M. Augath, P. Heiler, S. Kirsch, L.R. Schad, In vivo 39K, 23Na and 1H MR imaging using a triple resonant RF coil setup, J. Magn. Reson. 200 (2009) 134–136.

[333] S. Kirsch, M. Augath, D. Seiffge, L. Schilling, L.R. Schad, In vivo chlorine-35, sodium-23 and proton magnetic resonance imaging of the rat brain, NMR Biomed. 23 (2010) 592–600.

[334] V.D. Schepkin, M. Elumalai, J.A. Kitchen, C. Qian, P.L. Gor'kov, W.W. Brey, In vivo chlorine and sodium MRI of rat brain at 21.1 T, Magn. Reson. Mater. Phys. Biol. Med. 27 (2014) 63–70.

[335] G. Madelin, R.R. Regatte, Biomedical applications of sodium MRI in vivo, J. Magn. Reson. Imaging 38 (2013) 511–529.

[336] R.R. Regatte, Advances in sodium MRI: biomedical applications from head to foot, NMR Biomed. 29 (2016) 94–95.

[337] V.D. Schepkin, Sodium MRI of glioma in animal models at ultrahigh magnetic fields, NMR Biomed. 29 (2016) 175–186.

[338] N.J. Shah, W.A. Worthoff, K.J. Langen, Imaging of sodium in the brain: a brief review, NMR Biomed. 29 (2016) 162–174.

[339] K.R. Thulborn, Quantitative sodium MR imaging: a review of its evolving role in medicine, Neuroimage 168 (2018) 250–268.

[340] F.E. Boada, G. Laverde, C. Jungreis, E. Nemoto, C. Tanase, I. Hancu, Loss of cell ion homeostasis and cell viability in the brain: what sodium MRI can tell us, Curr. Top. Dev. Biol. 70 (2005) 77–101.

[341] R. Ouwerkerk, Sodium MRI, Methods Mol. Biol. 711 (2011) 175–201.

[342] M.A. Weber, A.M. Nagel, A.M. Marschar, P. Glemser, K. Jurkat-Rott, M.B. Wolf, M.E. Ladd, H.P. Schlemmer, H.U. Kauczor, F. Lehmann-Horn, 7-T Cl and Na MR imaging for detection of mutation-dependent alterations in muscular edema and fat fraction with sodium and chloride concentrations in muscular periodic paralyses, Radiology 280 (2016) 848–859.

[343] A. Biller, S. Badde, A. Nagel, J.O. Neumann, W. Wick, A. Hertenstein, M. Bendszus, F. Sahm, N. Benkhedah, J. Kleesiek, Improved brain tumor classification by sodium MR imaging: prediction of IDH mutation status and tumor progression, AJNR Am. J. Neuroradiol. 37 (2016) 66–73.

[344] K.R. Thulborn, A. Lu, I.C. Atkinson, F. Damen, J.L. Villano, Quantitative sodium MR imaging and sodium bioscales for the management of brain tumors, Neuroimaging Clin. N. Am. 19 (2009) 615–624.

[345] R. Ouwerkerk, K.B. Bleich, J.S. Gillen, M.G. Pomper, P.A. Bottomley, Tissue sodium concentration in human brain tumors as measured with 23Na MR imaging, Radiology 227 (2003) 529–537.

[346] C.M. Laymon, M.J. Oborski, V.K. Lee, D.K. Davis, E.C. Wiener, F.S. Lieberman, F. E. Boada, J.M. Mountz, Combined imaging biomarkers for therapy evaluation in glioblastoma multiforme: correlating sodium MRI and F-18 FLT PET on a voxel-wise basis, Magn. Reson. Imaging 30 (2012) 1268–1278.

[347] K.R. Thulborn, T.S. Gindin, D. Davis, P. Erb, Comprehensive MR imaging protocol for stroke management: tissue sodium concentration as a measure of tissue viability in nonhuman primate studies and in clinical studies, Radiology 213 (1999) 156–166.

[348] K.R. Thulborn, D. Davis, J. Snyder, H. Yonas, A. Kassam, Sodium MR imaging of acute and subacute stroke for assessment of tissue viability, Neuroimaging Clin. N. Am. 15 (2005) 639–653, xi-xii.

[349] E.A. Mellon, D.T. Pilkinton, C.M. Clark, M.A. Elliott, W.R. Witschey 2nd, A. Borthakur, R. Reddy, Sodium MR imaging detection of mild Alzheimer disease: preliminary study, AJNR Am. J. Neuroradiol. 30 (2009) 978–984.

[350] K. Reetz, S. Romanzetti, I. Dogan, C. Sass, C.J. Werner, J. Schiefer, J.B. Schulz, N. J. Shah, Increased brain tissue sodium concentration in Huntington's Disease – a sodium imaging study at 4 T, Neuroimage 63 (2012) 517–524.

[351] B. Ridley, A. Marchi, J. Wirsich, E. Soulier, S. Confort-Gouny, L. Schad, F. Bartolomei, J.P. Ranjeva, M. Guye, W. Zaaraoui, Brain sodium MRI in human epilepsy: disturbances of ionic homeostasis reflect the organization of pathological regions, Neuroimage 157 (2017) 173–183.

[352] K. Thulborn, E. Lui, J. Guntin, S. Jamil, Z. Sun, T.C. Claiborne, I.C. Atkinson, Quantitative sodium MRI of the human brain at 9.4 T provides assessment of tissue sodium concentration and cell volume fraction during normal aging, NMR Biomed. 29 (2016) 137–143.

[353] G. Madelin, J.M. Silver, T. Bushnik, I.I. Kirov, Quantitative sodium MRI in traumatic brain injury (TBI): pilot study, in: Proceedings 24th Scientific Meeting, International Society for Magnetic Resonance in Medicine, Singapore, 2016, p. 1210.

[354] M. Petracca, L. Fleysher, N. Oesingmann, M. Inglese, Sodium MRI of multiple sclerosis, NMR Biomed. 29 (2016) 153–161.

[355] S.G. Waxman, Axonal conduction and injury in multiple sclerosis: the role of sodium channels, Nat. Rev. Neurosci. 7 (2006) 932–941.

[356] K.J. Smith, Sodium channels and multiple sclerosis: roles in symptom production, damage and therapy, Brain Pathol. 17 (2007) 230–242.

[357] A. Tsang, R.W. Stobbe, N. Asdaghi, M.S. Hussain, Y.A. Bhagat, C. Beaulieu, D. Emery, K.S. Butcher, Relationship between sodium intensity and perfusion deficits in acute ischemic stroke, J. Magn. Reson. Imaging 33 (2011) 41–47.

[358] T. Kushnir, T. Knubovets, Y. Itzchak, U. Eliav, M. Sadeh, L. Rapoport, E. Kott, G. Navon, In vivo 23Na NMR studies of myotonic dystrophy, Magn. Reson. Med. 37 (1997) 192–196.

[359] C.D. Constantinides, J.S. Gillen, F.E. Boada, M.G. Pomper, P.A. Bottomley, Human skeletal muscle: sodium MR imaging and quantification-potential applications in exercise and disease, Radiology 216 (2000) 559–568.

[360] M.A. Weber, A.M. Nagel, K. Jurkat-Rott, F. Lehmann-Horn, Sodium 23Na MRI detects elevated muscular sodium concentration in Duchenne muscular dystrophy, Neurology 77 (2011) 2017–2024.

[361] M.A. Weber, A.M. Nagel, M.B. Wolf, K. Jurkat-Rott, H.U. Kauczor, W. Semmler, F. Lehmann-Horn, Permanent muscular sodium overload and persistent muscle edema in Duchenne muscular dystrophy: a possible contributor of progressive muscle degeneration, J. Neurol. 259 (2012) 2385–2392.

[362] C. Kopp, P. Linz, A. Dahlmann, M. Hammon, J. Jantsch, D.N. Muller, R.E. Schmieder, A. Cavallaro, K.U. Eckardt, M. Uder, F.C. Luft, J. Titze, 23Na magnetic resonance imaging-determined tissue sodium in healthy subjects and hypertensive patients, Hypertension 61 (2013) 635–640.

[363] A. Dahlmann, K. Dorfelt, F. Eicher, P. Linz, C. Kopp, I. Mossinger, S. Horn, B. Buschges-Seraphin, P. Wabel, M. Hammon, A. Cavallaro, K.U. Eckardt, P. Kotanko, N.W. Levin, B. Johannes, M. Uder, F.C. Luft, D.N. Muller, J.M. Titze, Magnetic resonance-determined sodium removal from tissue stores in hemodialysis patients, Kidney Int. 87 (2015) 434–441.

[364] M. Hammon, S. Grossmann, P. Linz, C. Kopp, A. Dahlmann, C. Garlichs, R. Janka, A. Cavallaro, F.C. Luft, M. Uder, J. Titze, 23Na magnetic resonance imaging of the lower leg of acute heart failure patients during diuretic treatment, PLoS One 10 (2015) e0141336.

[365] E. Amarteifio, A.M. Nagel, M.A. Weber, K. Jurkat-Rott, F. Lehmann-Horn, Hyperkalemic periodic paralysis and permanent weakness: 3-T MR imaging depicts intracellular 23Na overload–initial results, Radiology 264 (2012) 154–163.

[366] A.M. Nagel, E. Amarteifio, F. Lehmann-Horn, K. Jurkat-Rott, W. Semmler, L.R. Schad, M.A. Weber, 3 Tesla sodium inversion recovery magnetic resonance imaging allows for improved visualization of intracellular sodium content changes in muscular channelopathies, Invest. Radiol. 46 (2011) 759–766.

[367] M.A. Weber, S. Nielles-Vallespin, M. Essig, K. Jurkat-Rott, H.U. Kauczor, F. Lehmann-Horn, Muscle Na+ channelopathies: MRI detects intracellular 23Na accumulation during episodic weakness, Neurology 67 (2006) 1151–1158.

[368] G. Chang, L. Wang, M.E. Schweitzer, R.R. Regatte, 3D 23Na MRI of human skeletal muscle at 7 Tesla: initial experience, Eur. Radiol. 20 (2010) 2039–2046.

[369] S. Zbyn, V. Mlynarik, V. Juras, P. Szomolanyi, S. Trattnig, Evaluation of cartilage repair and osteoarthritis with sodium MRI, NMR Biomed. 29 (2016) 206–215.

[370] A.M. Nagel, M.A. Weber, A. Borthakur, R. Reddy, Skeletal muscle MR imaging beyond protons: with a focus on sodium MRI in musculoskeletal applications, in: M.A. Weber (Ed.), Magnetic Resonance Imaging of the Skeletal Musculature, Springer, Heidelberg, 2014, pp. 115–133.

[371] E.M. Shapiro, A. Borthakur, A. Gougoutas, R. Reddy, 23Na MRI accurately measures fixed charge density in articular cartilage, Magn. Reson. Med. 47 (2002) 284–291.

[372] A. Borthakur, E.M. Shapiro, S.V. Akella, A. Gougoutas, J.B. Kneeland, R. Reddy, Quantifying sodium in the human wrist in vivo by using MR imaging, Radiology 224 (2002) 598–602.

[373] S. Trattnig, G.H. Welsch, V. Juras, P. Szomolanyi, M.E. Mayerhoefer, D. Stelzeneder, T.C. Mamisch, O. Bieri, K. Scheffler, S. Zbyn, 23Na MR imaging at 7 T after knee matrix-associated autologous chondrocyte transplantation preliminary results, Radiology 257 (2010) 175–184.

[374] I.M. Noebauer-Huhmann, V. Juras, C.W. Pfirrmann, P. Szomolanyi, S. Zbyn, A. Messner, J. Wimmer, M. Weber, K.M. Friedrich, D. Stelzeneder, S. Trattnig, Sodium MR imaging of the lumbar intervertebral disk at 7 T: correlation with T2 mapping and modified Pfirrmann score at 3 T-preliminary results, Radiology 265 (2012) 555–564.

[375] S. Zbyn, M.O. Brix, V. Juras, S.E. Domayer, S.M. Walzer, V. Mlynarik, S. Apprich, K. Buckenmaier, R. Windhager, S. Trattnig, Sodium magnetic resonance imaging of ankle joint in cadaver specimens, volunteers, and patients after different cartilage repair techniques at 7 T: initial results, Invest. Radiol. 50 (2015) 246–254.

[376] R. Reddy, E.K. Insko, E.A. Noyszewski, R. Dandora, J.B. Kneeland, J.S. Leigh, Sodium MRI of human articular cartilage in vivo, Magn. Reson. Med. 39 (1998) 697–701.

[377] A. Borthakur, E.M. Shapiro, J. Beers, S. Kudchodkar, J.B. Kneeland, R. Reddy, Sensitivity of MRI to proteoglycan depletion in cartilage: comparison of sodium and proton MRI, Osteoarthritis Cartilage 8 (2000) 288–293.

[378] G. Madelin, J.S. Lee, S. Inati, A. Jerschow, R.R. Regatte, Sodium inversion recovery MRI of the knee joint in vivo at 7T, J. Magn. Reson. 207 (2010) 42–52.

[379] R. Ouwerkerk, M.A. Jacobs, K.J. Macura, A.C. Wolff, V. Stearns, S.D. Mezban, N. F. Khouri, D.A. Bluemke, P.A. Bottomley, Elevated tissue sodium concentration in malignant breast lesions detected with non-invasive 23Na MRI, Breast Cancer Res. Treat. 106 (2007) 151–160.

[380] O. Zaric, K. Pinker, S. Zbyn, B. Strasser, S. Robinson, L. Minarikova, S. Gruber, A. Farr, C. Singer, T.H. Helbich, S. Trattnig, W. Bogner, Quantitative sodium MR imaging at 7 T: initial results and comparison with diffusion-weighted imaging in patients with breast tumors, Radiology 280 (2016) 39–48.

[381] M.A. Jacobs, R. Ouwerkerk, A.C. Wolff, E. Gabrielson, H. Warzecha, S. Jeter, D. A. Bluemke, R. Wahl, V. Stearns, Monitoring of neoadjuvant chemotherapy using multiparametric, 23Na sodium MR, and multimodality (PET/CT/MRI) imaging in locally advanced breast cancer, Breast Cancer Res. Treat. 128 (2011) 119–126.

[382] T. Henzler, S. Konstandin, G. Schmid-Bindert, P. Apfaltrer, S. Haneder, F. Wenz, L. Schad, C. Manegold, S.O. Schoenberg, C. Fink, Imaging of tumor viability in lung cancer: initial results using 23Na-MRI, Rofo 184 (2012) 340–344.

[383] F.G. Zollner, S. Konstandin, J. Lommen, J. Budjan, S.O. Schoenberg, L.R. Schad, S. Haneder, Quantitative sodium MRI of kidney, NMR Biomed. 29 (2016) 197–205.

[384] A. Machnik, W. Neuhofer, J. Jantsch, A. Dahlmann, T. Tammela, K. Machura, J. K. Park, F.X. Beck, D.N. Muller, W. Derer, J. Goss, A. Ziomber, P. Dietsch, H. Wagner, N. van Rooijen, A. Kurtz, K.F. Hilgers, K. Alitalo, K.U. Eckardt, F.C. Luft, D. Kerjaschki, J. Titze, Macrophages regulate salt-dependent volume and blood pressure by a vascular endothelial growth factor-C-dependent buffering mechanism, Nat. Med. 15 (2009) 545–552.

[385] P. Linz, D. Santoro, W. Renz, J. Rieger, A. Ruehle, J. Ruff, M. Deimling, N. Rakova, D.N. Muller, F.C. Luft, J. Titze, T. Niendorf, Skin sodium measured with Na MRI at 7.0 T, NMR Biomed. 28 (2015) 54–62.

[386] T. Niendorf, K. Paul, C. Oezerdem, A. Graessl, S. Klix, T. Huelnhagen, F. Hezel, J. Rieger, H. Waiczies, J. Frahm, A.M. Nagel, E. Oberacker, L. Winter, W(h)ither human cardiac and body magnetic resonance at ultrahigh fields? Technical advances, practical considerations, applications, and clinical opportunities, NMR Biomed. (2015).

[387] A. Resetar, S.H. Hoffmann, A. Graessl, L. Winter, H. Waiczies, M.E. Ladd, T. Niendorf, A.M. Nagel, Retrospectively-gated CINE 23Na imaging of the heart at 7.0 Tesla using density-adapted 3D projection reconstruction, Magn. Reson. Imaging 33 (2015) 1091–1097.

[388] S. Zbyn, D. Stelzeneder, G.H. Welsch, L.L. Negrin, V. Juras, M.E. Mayerhoefer, P. Szomolanyi, W. Bogner, S.E. Domayer, M. Weber, S. Trattnig, Evaluation of native hyaline cartilage and repair tissue after two cartilage repair surgery techniques with 23Na MR imaging at 7 T: initial experience, Osteoarthritis Cartilage 20 (2012) 837–845.

[389] J. Pekar, L. Ligeti, Z. Ruttner, R.C. Lyon, T.M. Sinnwell, P. van Gelderen, D. Fiat, C.T. Moonen, A.C. McLaughlin, In vivo measurement of cerebral oxygen consumption and blood flow using 17O magnetic resonance imaging, Magn. Reson. Med. 21 (1991) 313–319.

[390] D. Fiat, J. Hankiewicz, S. Liu, S. Trbovic, S. Brint, 17O magnetic resonance imaging of the human brain, Neurol. Res. 26 (2004) 803–808.

[391] X.H. Zhu, N. Zhang, Y. Zhang, X. Zhang, K. Ugurbil, W. Chen, In vivo 17O NMR approaches for brain study at high field, NMR Biomed. 18 (2005) 83–103.

[392] I.C. Atkinson, K.R. Thulborn, Feasibility of mapping the tissue mass corrected bioscale of cerebral metabolic rate of oxygen consumption using 17-oxygen and 23-sodium MR imaging in a human brain at 9.4 T, Neuroimage 51 (2010) 723–733.

[393] A. Gordji-Nejad, K. Mollenhoff, A.M. Oros-Peusquens, D.R. Pillai, N.J. Shah, Characterizing cerebral oxygen metabolism employing oxygen-17 MRI/MRS at high fields, Magn. Reson. Mater. Phys., Biol. Med. 27 (2014) 81–93.

[394] K.A. Miles, R.E. Williams, Warburg revisited: imaging tumour blood flow and metabolism, Cancer Imaging 8 (2008) 81–86.

[395] M.F. Beal, Does impairment of energy metabolism result in excitotoxic neuronal death in neurodegenerative illnesses?, Ann Neurol. 31 (1992) 119–130.

[396] M. Wong-Riley, P. Antuono, K.C. Ho, R. Egan, R. Hevner, W. Liebl, Z. Huang, R. Rachel, J. Jones, Cytochrome oxidase in Alzheimer's disease: biochemical, histochemical, and immunohistochemical analyses of the visual and other systems, Vision Res. 37 (1997) 3593–3608.

[397] J.E. Baumgardner, E.A. Mellon, D.R. Tailor, K. Mallikarjunarao, A. Borthakur, R. Reddy, Mechanical ventilator for delivery of 17O2 in brief pulses, Open Biomed. Eng. J. 2 (2008) 57–63.

[398] S.H. Hoffmann, P. Begovatz, A.M. Nagel, R. Umathum, K. Schommer, P. Bachert, M. Bock, A measurement setup for direct 17O MRI at 7 T, Magn. Reson. Med. 66 (2011) 1109–1115.

[399] R. Borowiak, J. Groebner, M. Haas, J. Hennig, M. Bock, Direct cerebral and cardiac 17O-MRI at 3 Tesla: initial results at natural abundance, Magn. Reson. Mater. Phys., Biol. Med. 27 (2014) 95–99.

[400] M. Lu, Y. Zhang, K. Ugurbil, W. Chen, X.H. Zhu, In vitro and in vivo studies of 17O NMR sensitivity at 9.4 and 16.4 T, Magn. Reson. Med. 69 (2013) 1523–1527.

[401] V. Schepkin, A. Neubauer, C. Schuch, T. Glaeser, M. Kieverl, S.L. Ranner, W.W. Brey, S. Helsper, L.R. Schad, The first observation of 17O MRI in normal rats at 21.1 T, in: Proceedings 25th Scientific Meeting, International Society for Magnetic Resonance in Medicine, Honolulu, 2017, pp. 4546.

[402] S.H. Hoffmann, A. Radbruch, M. Bock, W. Semmler, A.M. Nagel, Direct O-17 MRI with partial volume correction: first experiences in a glioblastoma patient, Magn. Reson. Mater. Phys., Biol. Med. 27 (2014) 579–587.

[403] B. Chance, S. Eleff, J.S. Leigh Jr., D. Sokolow, A. Sapega, Mitochondrial regulation of phosphocreatine/inorganic phosphate ratios in exercising human muscle: a gated 31P NMR study, Proc. Natl. Acad. Sci. USA 78 (1981) 6714–6718.

[404] R.E. Gordon, P.E. Hanley, D. Shaw, D.G. Gadian, G.K. Radda, P. Styles, P.J. Bore, L. Chan, Localization of metabolites in animals using 31P topical magnetic resonance, Nature 287 (1980) 736–738.

[405] P.L. Hope, A.M. Costello, E.B. Cady, D.T. Delpy, P.S. Tofts, A. Chu, P.A. Hamilton, E.O. Reynolds, D.R. Wilkie, Cerebral energy metabolism studied with phosphorus NMR spectroscopy in normal and birth-asphyxiated infants, Lancet 2 (1984) 366–370.

[406] D.I. Hoult, S.J. Busby, D.G. Gadian, G.K. Radda, R.E. Richards, P.J. Seeley, Observation of tissue metabolites using 31P nuclear magnetic resonance, Nature 252 (1974) 285–287.

[407] G.K. Radda, The use of NMR spectroscopy for the understanding of disease, Science 233 (1986) 640–645.

[408] P.A. Bottomley, H.C. Charles, P.B. Roemer, D. Flamig, H. Engeseth, W.A. Edelstein, O.M. Mueller, Human in vivo phosphate metabolite imaging with 31P NMR, Magn. Reson. Med. 7 (1988) 319–336.

[409] P.R. Luyten, J.P. Groen, J.W. Vermeulen, J.A. den Hollander, Experimental approaches to image localized human 31P NMR spectroscopy, Magn. Reson. Med. 11 (1989) 1–21.

[410] W. Bogner, S. Gruber, S. Trattnig, M. Chmelik, High-resolution mapping of human brain metabolites by free induction decay 1H MRSI at 7 T, NMR Biomed. 25 (2012) 873–882.

[411] L.A. Brandao, M. Castillo, Adult brain tumors: clinical applications of magnetic resonance spectroscopy, Magn. Reson. Imaging Clin. N. Am. 24 (2016) 781–809.

[412] T. Martin Noguerol, J. Sanchez-Gonzalez, J.P. Martinez Barbero, R. Garcia-Figueiras, S. Baleato-Gonzalez, A. Luna, Clinical imaging of tumor metabolism with 1H magnetic resonance spectroscopy, Magn. Reson. Imaging Clin. N. Am. 24 (2016) 57–86.

[413] W.G. Negendank, R. Sauter, T.R. Brown, J.L. Evelhoch, A. Falini, E.D. Gotsis, A. Heerschap, K. Kamada, B.C. Lee, M.M. Mengeot, E. Moser, K.A. Padavic-Shaller, J.A. Sanders, T.A. Spraggins, A.E. Stillman, B. Terwey, T.J. Vogl, K. Wicklow, R.A. Zimmerman, Proton magnetic resonance spectroscopy in patients with glial tumors: a multicenter study, J. Neurosurg. 84 (1996) 449–458.

[414] M. Toussaint, S. Pinel, F. Auger, N. Durieux, M. Thomassin, E. Thomas, A. Moussaron, D. Meng, F. Plenat, M. Amouroux, T. Bastogne, C. Frochot, O. Tillement, F. Lux, M. Barberi-Heyob, Proton MR spectroscopy and diffusion MR imaging monitoring to predict tumor response to interstitial photodynamic therapy for glioblastoma, Theranostics 7 (2017) 436–451.

[415] M. Zarifi, A.A. Tzika, Proton MRS imaging in pediatric brain tumors, Pediatr. Radiol. 46 (2016) 952–962.

[416] E. Moser, E. Laistler, F. Schmitt, G. Kontaxis, Ultra-high field NMR and MRI – the role of magnet technology to increase sensitivity and specificity, Front. Phys. 5 (2017) 33.

[417] O. Gonen, S. Gruber, B.S.Y. Li, V. Mlynárik, E. Moser, Multivoxel 3D proton spectroscopy in the brain at 1.5 versus 3.0 T: signal-to-noise ratio and resolution comparison, Am. J. Neuroradiol. 22 (2001) 1727–1731.

[418] S. Gruber, V. Mlynárik, E. Moser, High-resolution 3D proton spectroscopic imaging of the human brain at 3 T: SNR issues and application for anatomy-matched voxel sizes, Magn. Reson. Med. 49 (2003) 299–306.

[419] A.D. Harris, M.G. Saleh, R.A.E. Edden, Edited 1H magnetic resonance spectroscopy in vivo: methods and metabolites, Magn. Reson. Med. 77 (2017) 1377–1389.

[420] I. Tkáč, P. Andersen, G. Adriany, H. Merkle, K. Ugurbil, R. Gruetter, In vivo 1H NMR spectroscopy of the human brain at 7 T, Magn. Reson. Med. 46 (2001) 451–456.

[421] S. Yang, J. Hu, Z. Kou, Y. Yang, Spectral simplification for resolved glutamate and glutamine measurement using a standard STEAM sequence with optimized timing parameters at 3, 4, 4.7, 7, and 9.4T, Magn. Reson. Med. 59 (2008) 236–244.

[422] R.A. de Graaf, In Vivo NMR Spectroscopy: Principles and Techniques, second ed., 2007.

[423] R. Gruetter, G. Adriany, I.Y. Choi, P.G. Henry, H. Lei, G. Oz, Localized in vivo 13C NMR spectroscopy of the brain, NMR Biomed. 16 (2003) 313–338.

[424] H. Bachelard, R. Badar-Goffer, NMR spectroscopy in neurochemistry, J. Neurochem. 61 (1993) 412–429.

[425] E.M. Chance, S.H. Seeholzer, K. Kobayashi, J.R. Williamson, Mathematical analysis of isotope labeling in the citric acid cycle with applications to 13C NMR studies in perfused rat hearts, J. Biol. Chem. 258 (1983) 13785–13794.

[426] C.R. Malloy, A.D. Sherry, F.M. Jeffrey, Analysis of tricarboxylic acid cycle of the heart using 13C isotope isomers, Am. J. Physiol. 259 (1990) H987–995.

[427] M.A. Garcia-Espinosa, T.B. Rodrigues, A. Sierra, M. Benito, C. Fonseca, H.L. Gray, B.L. Bartnik, M.L. Garcia-Martin, P. Ballesteros, S. Cerdan, Cerebral glucose metabolism and the glutamine cycle as detected by in vivo and in vitro 13C NMR spectroscopy, Neurochem. Int. 45 (2004) 297–303.

[428] C. Zwingmann, D. Leibfritz, Regulation of glial metabolism studied by 13C-NMR, NMR Biomed. 16 (2003) 370–399.

[429] S. Goluch, R. Frass-Kriegl, M. Meyerspeer, M. Pichler, J. Sieg, M. Gajdošík, M. Krššák, E. Laistler, Proton-decoupled carbon magnetic resonance spectroscopy in human calf muscles at 7 T using a multi-channel radiofrequency coil, Sci. Rep. 8 (2018) 6211.

[430] E. Seres Roig, A.W. Magill, G. Donati, M. Meyerspeer, L. Xin, O. Ipek, R. Gruetter, A double-quadrature radiofrequency coil design for proton-decoupled carbon-13 magnetic resonance spectroscopy in humans at 7T, Magn. Reson. Med. 73 (2015) 894–900.

[431] M. Meyerspeer, E. Seres Roig, R. Gruetter, A.W. Magill, An improved trap design for decoupling multinuclear RF coils, Magn. Reson. Med. 72 (2014) 584–590.

[432] M.C. Stephenson, F. Gunner, A. Napolitano, P.L. Greenhaff, I.A. Macdonald, N. Saeed, W. Vennart, S.T. Francis, P.G. Morris, Applications of multi-nuclear magnetic resonance spectroscopy at 7T, World J. Radiol. 3 (2011) 105–113.

[433] S.J. Bawden, M.C. Stephenson, E. Ciampi, K. Hunter, L. Marciani, I.A. Macdonald, G.P. Aithal, P.G. Morris, P.A. Gowland, Investigating the effects of an oral fructose challenge on hepatic ATP reserves in healthy volunteers: a 31P MRS study, Clin. Nutr. 35 (2016) 645–649.

[434] M.M. Chaumeil, J. Valette, M. Guillermier, E. Brouillet, F. Boumezbeur, A.S. Herard, G. Bloch, P. Hantraye, V. Lebon, Multimodal neuroimaging provides a highly consistent picture of energy metabolism, validating 31P MRS for measuring brain ATP synthesis, Proc. Natl. Acad. Sci. USA 106 (2009) 3988–3993.

[435] G.B. Fiedler, A.I. Schmid, S. Goluch, K. Schewzow, E. Laistler, F. Niess, E. Unger, M. Wolzt, A. Mirzahosseini, G.J. Kemp, E. Moser, M. Meyerspeer, Skeletal muscle ATP synthesis and cellular H(+) handling measured by localized 31P-MRS during exercise and recovery, Sci. Rep. 6 (2016) 32037.

[436] C. Holloway, M. ten Hove, K. Clarke, S. Neubauer, MR spectroscopy in heart failure, Front. Biosci. (Schol Ed) 3 (2011) 331–340.

[437] S.F. Solga, A. Horska, J.M. Clark, A.M. Diehl, Hepatic 31P magnetic resonance spectroscopy: a hepatologist's user guide, Liver Int. 25 (2005) 490–500.

[438] X.H. Zhu, F. Du, N. Zhang, Y. Zhang, H. Lei, X. Zhang, H. Qiao, K. Ugurbil, W. Chen, Advanced in vivo heteronuclear MRS approaches for studying brain bioenergetics driven by mitochondria, Methods Mol. Biol. 489 (2009) 317–357.

[439] G.J. Kemp, M. Meyerspeer, E. Moser, Absolute quantification of phosphorus metabolite concentrations in human muscle in vivo by 31P MRS: a quantitative review, NMR Biomed. 20 (2007) 555–565.

[440] B. Strasser, M. Povazan, G. Hangel, L. Hingerl, M. Chmelik, S. Gruber, S. Trattnig, W. Bogner, (2 + 1)D-CAIPIRINHA accelerated MR spectroscopic imaging of the brain at 7T, Magn. Reson. Med. 78 (2017) 429–440.

[441] B. Strasser, M. Chmelik, S.D. Robinson, G. Hangel, S. Gruber, S. Trattnig, W. Bogner, Coil combination of multichannel MRSI data at 7 T: MUSICAL, NMR Biomed. 26 (2013) 1796–1805.

[442] G. Hangel, B. Strasser, M. Povazan, S. Gruber, M. Chmelik, M. Gajdosik, S. Trattnig, W. Bogner, Lipid suppression via double inversion recovery with symmetric frequency sweep for robust 2D-GRAPPA-accelerated MRSI of the brain at 7 T, NMR Biomed. 28 (2015) 1413–1425.

[443] G. Goelman, S. Liu, R. Fleysher, L. Fleysher, R.I. Grossman, O. Gonen, Chemical-shift artifact reduction in Hadamard-encoded MR spectroscopic imaging at high (3T and 7T) magnetic fields, Magn. Reson. Med. 58 (2007) 167–173.

[444] G. Hangel, B. Strasser, M. Povazan, E. Heckova, L. Hingerl, R. Boubela, S. Gruber, S. Trattnig, W. Bogner, Ultra-high resolution brain metabolite mapping at 7 T by short-TR Hadamard-encoded FID-MRSI, Neuroimage 168 (2018) 199–210.

[445] M. Považan, G. Hangel, B. Strasser, S. Gruber, M. Chmelik, S. Trattnig, W. Bogner, Mapping of brain macromolecules and their use for spectral processing of 1H-MRSI data with an ultra-short acquisition delay at 7T, Neuroimage 121 (2015) 126–135.

[446] M. Považan, B. Strasser, G. Hangel, E. Heckova, S. Gruber, S. Trattnig, W. Bogner, Simultaneous mapping of metabolites and individual macromolecular components via ultra-short acquisition delay 1H MRSI in the brain at 7T, Magn. Reson. Med. 00 (2017) 1–10.

[447] F. Lam, C. Ma, B. Clifford, C.L. Johnson, Z.P. Liang, High-resolution 1H-MRSI of the brain using SPICE: data acquisition and image reconstruction, Magn. Reson. Med. 76 (2016) 1059–1070.

[448] C. Ma, F. Lam, C.L. Johnson, Z.P. Liang, Removal of nuisance signals from limited and sparse 1H MRSI data using a union-of-subspaces model, Magn. Reson. Med. 75 (2016) 488–497.

[449] V.O. Boer, B.L. vd Bank, G. van Vliet, P.R. Luijten, D.W.J. Klomp, Direct B0 field monitoring and real-time B0 field updating in the human breast at 7 tesla, Magn. Reson. Med. 67 (2012) 586–591.

[450] S. Jain, D.M. Sima, F. Sanaei Nezhad, G. Hangel, W. Bogner, S. Williams, S. Van Huffel, F. Maes, D. Smeets, Patch-based super-resolution of MR spectroscopic images: application to multiple sclerosis, Front. Neurosci. 11 (2017) 13.

[451] H. Prinsen, R.A. de Graaf, G.F. Mason, D. Pelletier, C. Juchem, Reproducibility measurement of glutathione, GABA, and glutamate: Towards in vivo neurochemical profiling of multiple sclerosis with MR spectroscopy at 7T, J. Magn. Reson. Imaging 45 (2017) 187–198.

[452] R. Gruetter, E.R. Seaquist, S. Kim, K. Ugurbil, Localized in vivo 13C-NMR of glutamate metabolism in the human brain: initial results at 4 tesla, Dev. Neurosci. 20 (1998) 380–388.

[453] R. Gruetter, E.R. Seaquist, K. Ugurbil, A mathematical model of compartmentalized neurotransmitter metabolism in the human brain, Am. J. Physiol. Endocrinol. Metab. 281 (2001) E100–112.

[454] F.D. Morgenthaler, R.B. van Heeswijk, L. Xin, S. Laus, H. Frenkel, H. Lei, R. Gruetter, Non-invasive quantification of brain glycogen absolute concentration, J. Neurochem. 107 (2008) 1414–1423.

[455] D.L. Rothman, I. Magnusson, L.D. Katz, R.G. Shulman, G.I. Shulman, Quantitation of hepatic glycogenolysis and gluconeogenesis in fasting humans with 13C NMR, Science 254 (1991) 573–576.

[456] A.F. Soares, R. Gruetter, H. Lei, Technical and experimental features of Magnetic Resonance Spectroscopy of brain glycogen metabolism, Anal. Biochem. 529 (2017) 117–126.

[457] R. Roussel, G. Velho, P.G. Carlier, L. Jouvensal, G. Bloch, In vivo NMR evidence for moderate glucose accumulation in human skeletal muscle during hyperglycemia, Am. J. Physiol. 271 (1996) E434–E438.

[458] M. Krssak, H. Hofer, F. Wrba, M. Meyerspeer, A. Brehm, A. Lohninger, P. Steindl-Munda, E. Moser, P. Ferenci, M. Roden, Non-invasive assessment of hepatic fat accumulation in chronic hepatitis C by 1H magnetic resonance spectroscopy, Eur. J. Radiol. 74 (2010) e60–66.

[459] M. Roden, Mechanisms of Disease: hepatic steatosis in type 2 diabetes–pathogenesis and clinical relevance, Nat. Clin. Practice. Endocrinol. Metab. 2 (2006) 335–348.

[460] D.E. Befroy, R.J. Perry, N. Jain, S. Dufour, G.W. Cline, J.K. Trimmer, J. Brosnan, D. L. Rothman, K.F. Petersen, G.I. Shulman, Direct assessment of hepatic

mitochondrial oxidative and anaplerotic fluxes in humans using dynamic 13C magnetic resonance spectroscopy, Nat. Med. 20 (2014) 98–102.
[461] J. Szendroedi, M. Chmelik, A.I. Schmid, P. Nowotny, A. Brehm, M. Krssak, E. Moser, M. Roden, Abnormal hepatic energy homeostasis in type 2 diabetes, Hepatology 50 (2009) 1079–1086.
[462] A.I. Schmid, J. Szendroedi, M. Chmelik, M. Krššák, E. Moser, M. Roden, Liver ATP synthesis is lower and relates to insulin sensitivity in patients with type 2 diabetes, Diab. Care 34 (2011) 448–453.
[463] M. Chmelík, L. Valkovič, P. Wolf, W. Bogner, M. Gajdošík, E. Halilbasic, S. Gruber, M. Trauner, M. Krebs, S. Trattnig, M. Krššák, Phosphatidylcholine contributes to in vivo 31P MRS signal from the human liver, Eur. Radiol. 25 (2015) 2059–2066.
[464] M. Chmelik, M. Považan, M. Krššák, S. Gruber, M. Tkačov, S. Trattnig, W. Bogner, In vivo 31P magnetic resonance spectroscopy of the human liver at 7 T: an initial experience, NMR Biomed. 27 (2014) 478–485.
[465] L.A.B. Purvis, W.T. Clarke, L. Valkovic, C. Levick, M. Pavlides, E. Barnes, J.F. Cobbold, M.D. Robson, C.T. Rodgers, Phosphodiester content measured in human liver by in vivo 31P MR spectroscopy at 7 tesla, Magn. Reson. Med. 78 (2017) 2095–2105.
[466] M. Chmelík, I. Just Kukurová, S. Gruber, M. Krššák, L. Valkovič, S. Trattnig, W. Bogner, Fully adiabatic 31P 2D-CSI with reduced chemical shift displacement error at 7 T – GOIA-1D-ISIS/2D-CSI, Magn. Reson. Med. 69 (2013) 1233–1244.
[467] G.J. Kemp, Muscle studies by 31P MRS, eMagRes 4 (2015) 525–534.
[468] E. Moser, Ultra-high-field magnetic resonance: why and when?, World J Radiol. 2 (2010) 37–40.
[469] W. Bogner, M. Chmelik, A.I. Schmid, E. Moser, S. Trattnig, S. Gruber, Assessment of 31P relaxation times in the human calf muscle: a comparison between 3 T and 7 T in vivo, Magn. Reson. Med. 62 (2009) 574–582.
[470] M. Meyerspeer, M. Krššák, E. Moser, Relaxation times of 31P-metabolites in human calf muscle at 3 T, Magn. Reson. Med. 49 (2003) 620–625.
[471] H. Lei, X.H. Zhu, X.L. Zhang, K. Ugurbil, W. Chen, In vivo 31P magnetic resonance spectroscopy of human brain at 7 T: an initial experience, Magn. Reson. Med. 49 (2003) 199–205.
[472] M. Meyerspeer, M. Krssak, G.J. Kemp, M. Roden, E. Moser, Dynamic interleaved 1H/31P STEAM MRS at 3 Tesla using a pneumatic force-controlled plantar flexion exercise rig, MAGMA 18 (2005) 257–262.
[473] M. Meyerspeer, T. Scheenen, A.I. Schmid, T. Mandl, E. Unger, E. Moser, Semi-LASER localized dynamic 31P magnetic resonance spectroscopy in exercising muscle at ultra-high magnetic field, Magn. Reson. Med. 65 (2011) 1207–1215.
[474] A.I. Schmid, K. Schewzow, G.B. Fiedler, S. Goluch, E. Laistler, M. Wolzt, E. Moser, M. Meyerspeer, Exercising calf muscle T2* changes correlate with pH, PCr recovery and maximum oxidative phosphorylation, NMR Biomed. 27 (2014) 553–560.
[475] S. Goluch, A. Kuehne, M. Meyerspeer, R. Kriegl, A.I. Schmid, G.B. Fiedler, T. Herrmann, J. Mallow, S.M. Hong, Z.H. Cho, J. Bernarding, E. Moser, E. Laistler, A form-fitted three channel 31P, two channel 1H transceiver coil array for calf muscle studies at 7 T, Magn. Reson. Med. 73 (2015) 2376–2389.
[476] G.B. Fiedler, M. Meyerspeer, A.I. Schmid, S. Goluch, K. Schewzow, E. Laistler, A. Mirzahosseini, F. Niess, E. Unger, M. Wolzt, E. Moser, Localized semi-LASER dynamic 31P magnetic resonance spectroscopy of the soleus during and following exercise at 7 T, MAGMA 28 (2015) 493–501.
[477] A.I. Schmid, M. Meyerspeer, S.D. Robinson, S. Goluch, M. Wolzt, G.B. Fiedler, W. Bogner, E. Laistler, M. Krssak, E. Moser, S. Trattnig, L. Valkovic, Dynamic PCr and pH imaging of human calf muscles during exercise and recovery using 31P gradient-Echo MRI at 7 Tesla, Magn. Reson. Med. 75 (2016) 2324–2331.
[478] M. Meyerspeer, S. Robinson, C.I. Nabuurs, T. Scheenen, A. Schoisengeier, E. Unger, G.J. Kemp, E. Moser, Comparing localized and nonlocalized dynamic 31P magnetic resonance spectroscopy in exercising muscle at 7 T, Magn. Reson. Med. 68 (2012) 1713–1723.
[479] F. Niess, G.B. Fiedler, A.I. Schmid, S. Goluch, R. Kriegl, M. Wolzt, E. Moser, M. Meyerspeer, Interleaved multivoxel 31 P MR spectroscopy, Magn. Reson. Med. 77 (2017) 921–927.
[480] L. Valkovič, M. Chmelík, M. Meyerspeer, B. Gagoski, C.T. Rodgers, M. Krššák, O. C. Andronesi, S. Trattnig, W. Bogner, Dynamic 31P–MRSI using spiral spectroscopic imaging can map mitochondrial capacity in muscles of the human calf during plantar flexion exercise at 7 T, NMR Biomed. 29 (2016) 1825–1834.
[481] K. Schewzow, G.B. Fiedler, M. Meyerspeer, S. Goluch, E. Laistler, M. Wolzt, E. Moser, A.I. Schmid, Dynamic ASL and T2-weighted MRI in exercising calf muscle at 7 T: a feasibility study, Magn. Reson. Med. 73 (2015) 1190–1195.
[482] P. Parasoglou, D. Xia, G. Chang, R.R. Regatte, 3D-mapping of phosphocreatine concentration in the human calf muscle at 7 T: Comparison to 3 T, Magn. Reson. Med. 70 (2013) 1619–1625.
[483] M. Krššák, K.F. Petersen, R. Bergeron, T. Price, D. Laurent, D.L. Rothman, M. Roden, G.I. Shulman, Intramuscular glycogen and intramyocellular lipid utilization during prolonged exercise and recovery in man: a 13C and 1H nuclear magnetic resonance spectroscopy study, J. Clin. Endocrinol. Metab. 85 (2000) 748–754.
[484] G. Perseghin, T.B. Price, K.F. Petersen, M. Roden, G.W. Cline, K. Gerow, D.L. Rothman, G.I. Shulman, Increased glucose transport-phosphorylation and muscle glycogen synthesis after exercise training in insulin-resistant subjects, N. Engl. J. Med. 335 (1996) 1357–1362.
[485] A.J. van den Bergh, S. Houtman, A. Heerschap, N.J. Rehrer, H.J.V.D. Boogert, B. Oeseburg, M.T. Hopman, Muscle glycogen recovery after exercise during glucose and fructose intake monitored by 13C-NMR, J. Appl. Physiol. 81 (1996) 1495–1500.
[486] T. Buehler, L. Bally, A.S. Dokumaci, C. Stettler, C. Boesch, Methodological and physiological test-retest reliability of 13C-MRS glycogen measurements in liver and in skeletal muscle of patients with type 1 diabetes and matched healthy controls, NMR Biomed. 29 (2016) 796–805.
[487] M.B. Bizino, S. Hammer, H.J. Lamb, Metabolic imaging of the human heart: clinical application of magnetic resonance spectroscopy, Heart 100 (2014) 881–890.
[488] S. Hammer, M. Snel, H.J. Lamb, I.M. Jazet, R.W. van der Meer, H. Pijl, E.A. Meinders, J.A. Romijn, A. de Roos, J.W.A. Smit, Prolonged caloric restriction in obese patients with type 2 diabetes mellitus decreases myocardial triglyceride content and improves myocardial function, J. Am. Coll. Cardiol. 52 (2008) 1006–1012.
[489] V.M. Stoll, W.T. Clarke, E. Levelt, A. Liu, S.G. Myerson, M.D. Robson, S. Neubauer, C.T. Rodgers, Dilated cardiomyopathy: phosphorus 31 MR spectroscopy at 7 T, Radiology 281 (2016) 409–417.
[490] K. Golman, J.S. Petersson, P. Magnusson, E. Johansson, P. Åkeson, C.M. Chai, G. Hansson, S. Månsson, Cardiac metabolism measured noninvasively by hyperpolarized 13C MRI, Magn. Reson. Med. 59 (2008) 1005–1013.
[491] S. Forsen, R.A. Hoffman, Study of moderately rapid chemical exchange reactions by means of nuclear magnetic double resonance, J. Chem. Phys. 39 (1963) 2892–2901.
[492] K.M. Ward, A.H. Aletras, R.S. Balaban, A new class of contrast agents for MRI based on proton chemical exchange dependent saturation transfer (CEST), J. Magn. Reson. 143 (2000) 79–87.
[493] J. Zhou, J.-F. Payen, D.A. Wilson, R.J. Traystman, P.C.M.v. Zijl, Using the amide proton signals of intracellular proteins and peptides to detect pH effects in MRI, Nat. Med. 9 (2003) 1085–1090.
[494] M. Zaiss, G. Angelovski, E. Demetriou, M.T. McMahon, X. Golay, K. Scheffler, QUESP and QUEST revisited – fast and accurate quantitative CEST experiments, Magn. Reson. Med. 79 (2018) 1708–1721.
[495] C.K. Jones, A. Huang, J. Xu, R.A. Edden, M. Schar, J. Hua, N. Oskolkov, D. Zaca, J. Zhou, M.T. McMahon, J.J. Pillai, P.C. van Zijl, Nuclear Overhauser enhancement (NOE) imaging in the human brain at 7T, Neuroimage 77 (2013) 114–124.
[496] Z. Wen, S. Hu, F. Huang, X. Wang, L. Guo, X. Quan, S. Wang, J. Zhou, MR imaging of high-grade brain tumors using endogenous protein and peptide-based contrast, Neuroimage 51 (2010) 616–622.
[497] M. Zaiss, J. Windschuh, S. Goerke, D. Paech, J.E. Meissner, S. Burth, P. Kickingereder, W. Wick, M. Bendszus, H.P. Schlemmer, M.E. Ladd, P. Bachert, A. Radbruch, Downfield-NOE-suppressed amide-CEST-MRI at 7 Tesla provides a unique contrast in human glioblastoma, Magn. Reson. Med. 77 (2017) 196–208.
[498] M. Zaiss, J. Windschuh, D. Paech, J.-E. Meissner, S. Burth, B. Schmitt, P. Kickingereder, B. Wiestler, W. Wick, M. Bendszus, H.-P. Schlemmer, M.E. Ladd, P. Bachert, A. Radbruch, Relaxation-compensated CEST-MRI of the human brain at 7T: unbiased insight into NOE and amide signal changes in human glioblastoma, Neuroimage 112 (2015) 180–188.
[499] F. Kogan, M. Haris, A. Singh, K. Cai, C. Debrosse, R.P.R. Nanga, H. Hariharan, R. Reddy, Method for high-resolution imaging of creatine in vivo using chemical exchange saturation transfer, Magn. Reson. Med. 71 (2014) 164–172.
[500] E. Rerich, M. Zaiss, A. Korzowski, M.E. Ladd, P. Bachert, Relaxation-compensated CEST-MRI at 7 T for mapping of creatine content and pH-preliminary application in human muscle tissue in vivo, NMR Biomed. 28 (2015) 1402–1412.
[501] K. Cai, M. Haris, A. Singh, F. Kogan, J.H. Greenberg, H. Hariharan, J.A. Detre, R. Reddy, Magnetic resonance imaging of glutamate, Nat. Med. 18 (2012) 302–306.
[502] M. Haris, K. Nath, K. Cai, A. Singh, R. Crescenzi, F. Kogan, G. Verma, S. Reddy, H. Hariharan, E.R. Melhem, R. Reddy, Imaging of glutamate neurotransmitter alterations in Alzheimer's disease, NMR Biomed. 26 (2013) 386–391.
[503] S. Aime, L. Calabi, L. Biondi, M. De Miranda, S. Ghelli, L. Paleari, C. Rebaudengo, E. Terreno, Iopamidol: exploring the potential use of a well-established X-ray contrast agent for MRI, Magn. Reson. Med. 53 (2005) 830–834.
[504] K.M. Jones, E.A. Randtke, C.M. Howison, J. Cárdenas-Rodríguez, P.J. Sime, M.R. Kottmann, M.D. Pagel, Measuring extracellular pH in a lung fibrosis model with acidoCEST MRI, Mol. Imaging Biol.: MIB 17 (2015) 177–184.
[505] D.L. Longo, W. Dastru, G. Digilio, J. Keupp, S. Langereis, S. Lanzardo, S. Prestigio, O. Steinbach, E. Terreno, F. Uggeri, S. Aime, Iopamidol as a responsive MRI-chemical exchange saturation transfer contrast agent for pH mapping of kidneys: In vivo studies in mice at 7 T, Magn. Reson. Med. 65 (2011) 202–211.
[506] K.W.Y. Chan, M.T. McMahon, Y. Kato, G. Liu, J.W.M. Bulte, Z.M. Bhujwalla, D. Artemov, P.C.M. van Zijl, Natural D-glucose as a biodegradable MRI contrast agent for detecting cancer, Magn. Reson. Med. 68 (2012) 1764–1773.
[507] P. Schuenke, C. Koehler, A. Korzowski, J. Windschuh, P. Bachert, M.E. Ladd, S. Mundiyanapurath, D. Paech, S. Bickelhaupt, D. Bonekamp, H.-P. Schlemmer, A. Radbruch, M. Zaiss, Adiabatically prepared spin-lock approach for T1ρ-based dynamic glucose enhanced MRI at ultrahigh fields, Magn. Reson. Med. 78 (2017) 215–225.
[508] S. Walker-Samuel, R. Ramasawmy, F. Torrealdea, M. Rega, V. Rajkumar, S.P. Johnson, S. Richardson, M. Goncalves, H.G. Parkes, E. Arstad, D.L. Thomas, R.B.

Pedley, M.F. Lythgoe, X. Golay, In vivo imaging of glucose uptake and metabolism in tumors, Nat. Med. 19 (2013) 1067–1072.

[509] X. Xu, N.N. Yadav, L. Knutsson, J. Hua, R. Kalyani, E. Hall, J. Laterra, J. Blakeley, R. Strowd, M. Pomper, P. Barker, K. Chan, G. Liu, M.T. McMahon, R.D. Stevens, P.C. van Zijl, Dynamic glucose-enhanced (DGE) MRI: translation to human scanning and first results in glioma patients, Tomography 1 (2015) 105–114.

[510] F.A. Nasrallah, G. Pagès, P.W. Kuchel, X. Golay, K.-H. Chuang, Imaging brain deoxyglucose uptake and metabolism by glucoCEST MRI, J. Cereb. Blood Flow Metab. 33 (2013) 1270–1278.

[511] M. Rivlin, I. Tsarfaty, G. Navon, Functional molecular imaging of tumors by chemical exchange saturation transfer MRI of 3-O-Methyl-D-glucose, Magn. Reson. Med. 72 (2014) 1375–1380.

[512] J.J. Chung, W. Choi, T. Jin, J.H. Lee, S.G. Kim, Chemical-exchange-sensitive MRI of amide, amine and NOE at 9.4 T versus 15.2 T, NMR Biomed. 30 (2017).

[513] A. Singh, M. Haris, K. Cai, V.B. Kassey, F. Kogan, D. Reddy, H. Hariharan, R. Reddy, Chemical exchange saturation transfer magnetic resonance imaging of human knee cartilage at 3 T and 7 T, Magn. Reson. Med. 68 (2012) 588–594.

[514] D. Longo, S. Colombo, W. Dastru, L. Poggi, F. Tedoldi, E. Terreno, F. Uggeri, S. Aime, CMR2009: 11.02: evaluating iopamidol as pH-responsive CEST agent at 3 and 7 T, Contrast Media Mol. Imaging 4 (2009) 294–295.

[515] H.-Y. Heo, Y. Zhang, S. Jiang, D.-H. Lee, J. Zhou, Quantitative assessment of amide proton transfer (APT) and nuclear overhauser enhancement (NOE) imaging with extrapolated semisolid magnetization transfer reference (EMR) signals: II. Comparison of three EMR models and application to human brain glioma at 3 Tesla, Magn. Reson. Med. 75 (2016) 1630–1639.

[516] M. Zaiss, P. Ehses, K. Scheffler, Snapshot-CEST: Optimizing spiral-centric-reordered gradient echo acquisition for fast and robust 3D CEST MRI at 9.4 T, NMR Biomed. 31 (2018) e3879.

[517] K.L. Desmond, F. Moosvi, G.J. Stanisz, Mapping of amide, amine, and aliphatic peaks in the CEST spectra of murine xenografts at 7 T, Magn. Reson. Med. (2013).

[518] C.K. Jones, D. Polders, J. Hua, H. Zhu, H.J. Hoogduin, J. Zhou, P. Luijten, P.C. van Zijl, In vivo three-dimensional whole-brain pulsed steady-state chemical exchange saturation transfer at 7 T, Magn. Reson. Med. 67 (2012) 1579–1589.

[519] P.C.M. van Zijl, W.W. Lam, J. Xu, L. Knutsson, G.J. Stanisz, Magnetization transfer contrast and chemical exchange saturation transfer MRI. Features and analysis of the field-dependent saturation spectrum, Neuroimage 168 (2018) 222–241.

[520] W. Wei, G. Jia, D. Flanigan, J. Zhou, M.V. Knopp, Chemical exchange saturation transfer MR imaging of articular cartilage glycosaminoglycans at 3 T: accuracy of B0 Field Inhomogeneity corrections with gradient echo method, Magn. Reson. Imaging 32 (2014) 41–47.

[521] J. Windschuh, M. Zaiss, J.-E. Meissner, D. Paech, A. Radbruch, M.E. Ladd, P. Bachert, Correction of B1-inhomogeneities for relaxation-compensated CEST imaging at 7 T, NMR Biomed. 28 (2015) 529–537.

[522] A. Singh, K. Cai, M. Haris, H. Hariharan, R. Reddy, On B1 inhomogeneity correction of in vivo human brain glutamate chemical exchange saturation transfer contrast at 7T, Magn. Reson. Med. (2012).

[523] D.H.Y. Tse, N.A. da Silva, B.A. Poser, N.J. Shah, B1+ inhomogeneity mitigation in CEST using parallel transmission, Magn. Reson. Med. 78 (2017) 2216–2225.

[524] H. Mehrabian, K.L. Desmond, H. Soliman, A. Sahgal, G.J. Stanisz, Differentiation between radiation necrosis and tumor progression using chemical exchange saturation transfer, Clin. Cancer Res. 23 (2017) 3667–3675.

[525] O. Togao, T. Yoshiura, J. Keupp, A. Hiwatashi, K. Yamashita, K. Kikuchi, Y. Suzuki, S.O. Suzuki, T. Iwaki, N. Hata, M. Mizoguchi, K. Yoshimoto, K. Sagiyama, M. Takahashi, H. Honda, Amide proton transfer imaging of adult diffuse gliomas: correlation with histopathological grades, Neuro-Oncology 16 (2014) 441–448.

[526] S. Jiang, T. Zou, C.G. Eberhart, M.A.V. Villalobos, H.-Y. Heo, Y. Zhang, Y. Wang, X. Wang, H. Yu, Y. Du, P.C.M. Zijl, Z. Wen, J. Zhou, Predicting IDH mutation status in grade II gliomas using amide proton transfer-weighted (APTw) MRI, Magn. Reson. Med. 78 (2017) 1100–1109.

[527] S. Jiang, Q. Rui, Y. Wang, H.Y. Heo, T. Zou, H. Yu, Y. Zhang, X. Wang, Y. Du, X. Wen, F. Chen, J. Wang, C.G. Eberhart, J. Zhou, Z. Wen, Discriminating MGMT promoter methylation status in patients with glioblastoma employing amide proton transfer-weighted MRI metrics, Eur. Radiol. 28 (2018) 2115–2123.

[528] R.J. Harris, T.F. Cloughesy, L.M. Liau, R.M. Prins, J.P. Antonios, D. Li, W.H. Yong, W.B. Pope, A. Lai, P.L. Nghiemphu, B.M. Ellingson, pH-weighted molecular imaging of gliomas using amine chemical exchange saturation transfer MRI, Neuro-Oncology 17 (2015) 1514–1524.

[529] G.W.J. Harston, Y.K. Tee, N. Blockley, T.W. Okell, S. Thandeswaran, G. Shaya, F. Sheerin, M. Cellerini, S. Payne, P. Jezzard, M. Chappell, J. Kennedy, Identifying the ischaemic penumbra using pH-weighted magnetic resonance imaging, Brain: J. Neurol. 138 (2015) 36–42.

[530] Y.K. Tee, G.W. Harston, N. Blockley, T.W. Okell, J. Levman, F. Sheerin, M. Cellerini, P. Jezzard, J. Kennedy, S.J. Payne, M.A. Chappell, Comparing different analysis methods for quantifying the MRI amide proton transfer (APT) effect in hyperacute stroke patients, NMR Biomed. 27 (2014) 1019–1029.

[531] A. Tietze, J. Blicher, I.K. Mikkelsen, L. Østergaard, M.K. Strother, S.A. Smith, M. J. Donahue, Assessment of ischemic penumbra in patients with hyperacute stroke using amide proton transfer (APT) chemical exchange saturation transfer (CEST) MRI, NMR Biomed. 27 (2014) 163–174.

[532] S. Goerke, K.S. Milde, R. Bukowiecki, P. Kunz, K.D. Klika, T. Wiglenda, A. Mogk, E.E. Wanker, B. Bukau, M.E. Ladd, P. Bachert, M. Zaiss, Aggregation-induced changes in the chemical exchange saturation transfer (CEST) signals of proteins, NMR Biomed. 30 (2017).

[533] S. Goerke, M. Zaiss, P. Kunz, K.D. Klika, J.D. Windschuh, A. Mogk, B. Bukau, M. E. Ladd, P. Bachert, Signature of protein unfolding in chemical exchange saturation transfer imaging, NMR Biomed. 28 (2015) 906–913.

[534] M. Zaiss, P. Kunz, S. Goerke, A. Radbruch, P. Bachert, MR imaging of protein folding in vitro employing nuclear-Overhauser-mediated saturation transfer, NMR Biomed. 26 (2013) 1815–1822.

[535] K. Cai, A. Singh, H. Poptani, W. Li, S. Yang, Y. Lu, H. Hariharan, X.J. Zhou, R. Reddy, CEST signal at 2 ppm (CEST@2ppm) from Z-spectral fitting correlates with creatine distribution in brain tumor, NMR Biomed. 28 (2015) 1–8.

[536] L. Chen, H. Zeng, X. Xu, N.N. Yadav, S. Cai, N.A. Puts, P.B. Barker, T. Li, R.G. Weiss, P.C.M. van Zijl, J. Xu, Investigation of the contribution of total creatine to the CEST Z-spectrum of brain using a knockout mouse model, NMR Biomed. 30 (2017).

[537] X.-Y. Zhang, J. Xie, F. Wang, E.C. Lin, J. Xu, D.F. Gochberg, J.C. Gore, Z. Zu, Assignment of the molecular origins of CEST signals at 2 ppm in rat brain, Magn. Reson. Med. 78 (2017) 881–887.

[538] B. Schmitt, S. Zbyn, D. Stelzeneder, V. Jellus, D. Paul, L. Lauer, P. Bachert, S. Trattnig, Cartilage quality assessment by using glycosaminoglycan chemical exchange saturation transfer and 23Na MR imaging at 7 T, Radiology 260 (2011) 257–264.

[539] D. Paech, P. Schuenke, C. Koehler, J. Windschuh, S. Mundiyanapurath, S. Bickelhaupt, D. Bonekamp, P. Baumer, P. Bachert, M.E. Ladd, M. Bendszus, W. Wick, A. Unterberg, H.P. Schlemmer, M. Zaiss, A. Radbruch, T1rho-weighted dynamic glucose-enhanced MR imaging in the human brain, Radiology 285 (2017) 914–922.

[540] P. Schuenke, D. Paech, C. Koehler, J. Windschuh, P. Bachert, M.E. Ladd, H.P. Schlemmer, A. Radbruch, M. Zaiss, Fast and quantitative T1rho-weighted dynamic glucose enhanced MRI, Sci. Rep. 7 (2017) 42093.

[541] K. Ugurbil, Magnetic resonance imaging at ultrahigh fields, IEEE Trans. Biomed. Eng. 61 (2014) 1364–1379.

[542] S.P. Lee, A.C. Silva, K. Ugurbil, S.G. Kim, Diffusion-weighted spin-echo fMRI at 9.4 T: microvascular/tissue contribution to BOLD signal changes, Magn. Reson. Med. 42 (1999) 919–928.

[543] D.G. Norris, Principles of magnetic resonance assessment of brain function, J. Magn. Reson. Imaging 23 (2006) 794–807.

[544] T.Q. Duong, E. Yacoub, G. Adriany, X.P. Hu, K. Ugurbil, S.G. Kim, Microvascular BOLD contribution at 4 and 7 T in the human brain: gradient-echo and spin-echo fMRI with suppression of blood effects, Magn. Reson. Med. 49 (2003) 1019–1027.

[545] G. Krüger, G.H. Glover, Physiological noise in oxygenation-sensitive magnetic resonance imaging, Magn. Reson. Med. 46 (2001) 631–637.

[546] C. Triantafyllou, J.R. Polimeni, B. Keil, L.L. Wald, Coil-to-coil physiological noise correlations and their impact on functional MRI time-series signal-to-noise ratio, Magn. Reson. Med. 76 (2016) 1708–1719.

[547] C. Triantafyllou, J.R. Polimeni, L.L. Wald, Physiological noise and signal-to-noise ratio in fMRI with multi-channel array coils, Neuroimage 55 (2011) 597–606.

[548] C. Triantafyllou, R.D. Hoge, G. Krüger, C.J. Wiggins, A. Potthast, G.C. Wiggins, L. L. Wald, Comparison of physiological noise at 1.5 T, 3 T and 7 T and optimization of fMRI acquisition parameters, Neuroimage 26 (2005) 243–250.

[549] D.K. Sodickson, W.J. Manning, Simultaneous acquisition of spatial harmonics (SMASH): fast imaging with radiofrequency coil arrays, Magn. Reson. Med. 38 (1997) 591–603.

[550] M.A. Griswold, P.M. Jakob, R.M. Heidemann, M. Nittka, V. Jellus, J. Wang, B. Kiefer, A. Haase, Generalized autocalibrating partially parallel acquisitions (GRAPPA), Magn. Reson. Med. 47 (2002) 1202–1210.

[551] D.A. Feinberg, S. Moeller, S.M. Smith, E. Auerbach, S. Ramanna, M.F. Glasser, K. L. Miller, K. Ugurbil, E. Yacoub, Multiplexed echo planar imaging for sub-second whole brain fMRI and fast diffusion imaging, PLoS One 5 (2010).

[552] M. Barth, F. Breuer, P.J. Koopmans, D.G. Norris, B.A. Poser, Simultaneous multislice (SMS) imaging techniques, Magn. Reson. Med. 75 (2016) 63–81.

[553] F.A. Breuer, M. Blaimer, R.M. Heidemann, M.F. Mueller, M.A. Griswold, P.M. Jakob, Controlled aliasing in parallel imaging results in higher acceleration (CAIPIRINHA) for multi-slice imaging, Magn. Reson. Med. 53 (2005) 684–691.

[554] K. Setsompop, B.A. Gagoski, J.R. Polimeni, T. Witzel, V.J. Wedeen, L.L. Wald, Blipped-controlled aliasing in parallel imaging for simultaneous multislice echo planar imaging with reduced g-factor penalty, Magn. Reson. Med. 67 (2012) 1210–1224.

[555] J.P. Marques, D.G. Norris, How to choose the right MR sequence for your research question at 7T and above?, Neuroimage 168 (2018) 119–140

[556] Connectome Coordination Facility, 2017. <https://www.humanconnectome.org/> (accessed 29 December 2017).

[557] B.A. Poser, P.J. Koopmans, T. Witzel, L.L. Wald, M. Barth, Three dimensional echo-planar imaging at 7 Tesla, Neuroimage 51 (2010) 261–266.

[558] A. Lutti, D.L. Thomas, C. Hutton, N. Weiskopf, High-resolution functional MRI at 3 T: 3D/2D echo-planar imaging with optimized physiological noise correction, Magn. Reson. Med. 69 (2013) 1657–1664.

[559] J. Jorge, P. Figueiredo, W. van der Zwaag, J.P. Marques, Signal fluctuations in fMRI data acquired with 2D-EPI and 3D-EPI at 7 Tesla, Magn. Reson. Imaging 31 (2013) 212–220.

[560] E. Yacoub, T.Q. Duong, P.F. Van de Moortele, M. Lindquist, G. Adriany, S.G. Kim, K. Ugurbil, X. Hu, Spin-echo fMRI in humans using high spatial resolutions and high magnetic fields, Magn. Reson. Med. 49 (2003) 655–664.

[561] R. Boyacioglu, J. Schulz, N.C.J. Muller, P.J. Koopmans, M. Barth, D.G. Norris, Whole brain, high resolution multiband spin-echo EPI fMRI at 7 T: a comparison with gradient-echo EPI using a color-word Stroop task, Neuroimage 97 (2014) 142–150.

[562] D.G. Norris, P.J. Koopmans, R. Boyacioglu, M. Barth, Power Independent of Number of Slices (PINS) radiofrequency pulses for low-power simultaneous multislice excitation, Magn. Reson. Med. 66 (2011) 1234–1240.

[563] C. Eichner, L.L. Wald, K. Setsompop, A low power radiofrequency pulse for simultaneous multislice excitation and refocusing, Magn. Reson. Med. 72 (2014) 949–958.

[564] J.B.M. Goense, N.K. Logothetis, Laminar specificity in monkey V1 using high-resolution SE-fMRI, Magn. Reson. Imaging 24 (2006) 381–392.

[565] D.G. Norris, Spin-echo fMRI: the poor relation?, Neuroimage 62 (2012) 1109–1115

[566] D.J. DeDora, S. Nedic, P. Katti, S. Arnab, L.L. Wald, A. Takahashi, K.R. Van Dijk, H.H. Strey, L.R. Mujica-Parodi, Signal fluctuation sensitivity: An improved metric for optimizing detection of resting-state fMRI networks, Front. Neurosci. 10 (2016) 180.

[567] A. Shmuel, E. Yacoub, D. Chaimow, N.K. Logothetis, K. Ugurbil, Spatio-temporal point-spread function of fMRI signal in human gray matter at 7 Tesla, Neuroimage 35 (2007) 539–552.

[568] C.A. Olman, P.F. Van de Moortele, K. Ugurbil, Point spread function for gradient echo and spin echo BOLD fMRI at 7 Tesla, in: Proceedings 12th Scientific Meeting, International Society for Magnetic Resonance in Medicine, Kyoto, 2004, p. 1066.

[569] J. Budde, G. Shajan, M. Zaitsev, K. Scheffler, R. Pohmann, Functional MRI in human subjects with gradient-echo and spin-echo EPI at 9.4 T, Magn. Reson. Med. 71 (2014) 209–218.

[570] K. Oshio, D.A. Feinberg, GRASE (gradient- and spin-echo) imaging: a novel fast MRI technique, Magn. Reson. Med. 20 (1991) 344–349.

[571] A.W. Song, E.C. Wong, J.S. Hyde, Echo-volume imaging, Magn. Reson. Med. 32 (1994) 668–671.

[572] D.A. Feinberg, N. Harel, S. Ramanna, K. Ugurbil, E. Yacoub, Sub-millimeter single-shot 3D GRASE with inner volume selection for T2 weighted fMRI applications at 7 Tesla, in: Proceedings 16th Scientific Meeting, International Society for Magnetic Resonance in Medicine, Toronto, 2008, p. 2373.

[573] V.G. Kemper, F. De Martino, E. Yacoub, R. Goebel, Variable flip angle 3D-GRASE for high resolution fMRI at 7 Tesla, Magn. Reson. Med. 76 (2016) 897–904.

[574] K. Scheffler, E. Seifritz, D. Bilecen, R. Venkatesan, J. Hennig, M. Deimling, E.M. Haacke, Detection of BOLD changes by means of a frequency-sensitive true FISP technique: preliminary results, NMR Biomed. 14 (2001) 490–496.

[575] K.L. Miller, B.A. Hargreaves, J. Lee, D. Ress, R.C. de Charms, J.M. Pauly, Functional brain imaging using a blood oxygenation sensitive steady state, Magn. Reson. Med. 50 (2003) 675–683.

[576] K.L. Miller, P. Jezzard, Modeling SSFP functional MRI contrast in the brain, Magn. Reson. Med. 60 (2008) 661–673.

[577] O. Bieri, K. Scheffler, Effect of diffusion in inhomogeneous magnetic fields on balanced steady-state free precession, NMR Biomed. 20 (2007) 1–10.

[578] R. Dharmakumar, X. Qi, J. Hong, G.A. Wright, Detecting microcirculatory changes in blood oxygen state with steady-state free precession imaging, Magn. Reson. Med. 55 (2006) 1372–1380.

[579] E.J. Auerbach, K. Heberlein, X. Hu, High-resolution T2 fMRI at high magnetic fields using PSIF, in: Proceedings 10th Scientific Meeting, International Society for Magnetic Resonance in Medicine, Honolulu, 2002, p. 123.

[580] M. Barth, H. Meyer, S.A.R. Kannengiesser, J.R. Polimeni, L.L. Wald, D.G. Norris, T-2-weighted 3D fMRI using S-2-SSFP at 7 Tesla, Magn. Reson. Med. 63 (2010) 1015–1020.

[581] M.L. Gyngell, The application of steady-state free precession in rapid 2DFT NMR imaging: FAST and CE-FAST sequences, Magn. Reson. Imag. 6 (1988) 415–419.

[582] K.L. Miller, FMRI using balanced steady-state free precession (SSFP), Neuroimage 62 (2012) 713–719.

[583] E. Formisano, D.S. Kim, F. Di Salle, P.F. van de Moortele, K. Ugurbil, R. Goebel, Mirror-symmetric tonotopic maps in human primary auditory cortex, Neuron 40 (2003) 859–869.

[584] F. De Martino, M. Moerel, P.F. van de Moortele, K. Ugurbil, R. Goebel, E. Yacoub, E. Formisano, Spatial organization of frequency preference and selectivity in the human inferior colliculus, Nat. Commun. 4 (2013) 1386.

[585] R.M. Sanchez-Panchuelo, S. Francis, R. Bowtell, D. Schluppeck, Mapping human somatosensory cortex in individual subjects with 7T functional MRI, J. Neurophysiol. 103 (2010) 2544–2556.

[586] R.M. Sanchez-Panchuelo, J. Besle, A. Beckett, R. Bowtell, D. Schluppeck, S. Francis, Within-digit functional parcellation of Brodmann areas of the human primary somatosensory cortex using functional magnetic resonance imaging at 7 Tesla, J. Neurosci. 32 (2012) 15815–15822.

[587] W. van der Zwaag, R. Kusters, A. Magill, R. Gruetter, R. Martuzzi, O. Blanke, J.P. Marques, Digit somatotopy in the human cerebellum: a 7T fMRI study, Neuroimage 67 (2013) 354–362.

[588] M. Kuper, M. Thurling, R. Stefanescu, S. Maderwald, J. Roths, H.G. Elles, M.E. Ladd, J. Diedrichsen, D. Timmann, Evidence for a motor somatotopy in the cerebellar dentate nucleus – an FMRI study in humans, Hum. Brain Mapp. 33 (2012) 2741–2749.

[589] S. Nasr, J.R. Polimeni, R.B. Tootell, Interdigitated color- and disparity-selective columns within human visual cortical areas V2 and V3, J. Neurosci. 36 (2016) 1841–1857.

[590] S.A. Engel, G.H. Glover, B.A. Wandell, Retinotopic organization in human visual cortex and the spatial precision of functional MRI, Cereb. Cortex 7 (1997) 181–192.

[591] J.R. Polimeni, B. Fischl, D.N. Greve, L.L. Wald, Laminar analysis of 7 T BOLD using an imposed spatial activation pattern in human V1, Neuroimage 52 (2010) 1334–1346.

[592] P.J. Koopmans, M. Barth, S. Orzada, D.G. Norris, Multi-echo fMRI of the cortical laminae in humans at 7 T, Neuroimage 56 (2011) 1276–1285.

[593] L. Muckli, F. De Martino, L. Vizioli, L.S. Petro, F.W. Smith, K. Ugurbil, R. Goebel, E. Yacoub, Contextual feedback to superficial layers of V1, Curr. Biol. 25 (2015) 2690–2695.

[594] P. Kok, L.J. Bains, T. van Mourik, D.G. Norris, F.P. de Lange, Selective activation of the deep layers of the human primary visual cortex by top-down feedback, Curr. Biol. 26 (2016) 371–376.

[595] I. Markuerkiaga, M. Barth, D.G. Norris, A cortical vascular model for examining the specificity of the laminar BOLD signal, Neuroimage 132 (2016) 491–498.

[596] C.A. Olman, N. Harel, D.A. Feinberg, S. He, P. Zhang, K. Ugurbil, E. Yacoub, Layer-specific fMRI reflects different neuronal computations at different depths in human V1, PLoS One 7 (2012) e32536.

[597] F. De Martino, J. Zimmermann, L. Muckli, K. Ugurbil, E. Yacoub, R. Goebel, Cortical depth dependent functional responses in humans at 7T: improved specificity with 3D GRASE, PLoS One 8 (2013).

[598] E. Yacoub, A. Shmuel, N. Logothetis, K. Ugurbil, Robust detection of ocular dominance columns in humans using Hahn Spin Echo BOLD functional MRI at 7 Tesla, Neuroimage 37 (2007) 1161–1177.

[599] E. Yacoub, N. Harel, K. Ugurbil, High-field fMRI unveils orientation columns in humans, Proc. Natl. Acad. Sci. USA 105 (2008) 10607–10612.

[600] F. De Martino, M. Moerel, K. Ugurbil, R. Goebel, E. Yacoub, E. Formisano, Frequency preference and attention effects across cortical depths in the human primary auditory cortex, Proc. Natl. Acad. Sci. USA 112 (2015) 16036–16041.

[601] M.E. Ladd, The quest for higher sensitivity in MRI through higher magnetic fields, Z. Med. Phys. 28 (2018) 1–3.

[602] O. Kraff, H.H. Quick, 7T: physics, safety, and potential clinical applications, J. Magn. Reson. Imaging 46 (2017) 1573–1589.

[603] M.E. Ladd, M. Bock, Problems and chances of high field magnetic resonance imaging, Radiologe 53 (2013) 401–410.

[604] K. Ugurbil, Imaging at ultrahigh magnetic fields: history, challenges, and solutions, Neuroimage 168 (2018) 7–32.

[605] T.M. Fiedler, M. Flöser, S. Rietsch, S. Orzada, H.H. Quick, M.E. Ladd, A.K. Bitz, Comparison of a 32-channel remote body coil for 7 Tesla with local and remote 8- and 16-channel transmit coil arrays, in: Proceedings 25th Scientific Meeting, International Society for Magnetic Resonance in Medicine, Honolulu, 2017, p. 4306.

[606] M.A. Erturk, X. Wu, Y. Eryaman, P.F. Van de Moortele, E.J. Auerbach, R.L. Lagore, L. DelaBarre, J.T. Vaughan, K. Ugurbil, G. Adriany, G.J. Metzger, Toward imaging the body at 10.5 tesla, Magn. Reson. Med. 77 (2017) 434–443.

[607] B. Denis Le, S. Thierry, Human brain MRI at 500 MHz, scientific perspectives and technological challenges, Supercond. Sci. Technol. 30 (2017) 033003.

[608] Wissenschaftsrat (German Council of Science and Humanities), Report on the Science-driven Evaluation of Large-scale Research Infrastructure Projects for Inclusion in an National Roadmap, Cologne, 2017, pp. 39–41. <www.wissenschaftsrat.de/download/archiv/6410-17_engl.pdf>.

[609] M.D. Bird, I.R. Dixon, J. Toth, Large, high-field magnet projects at the NHMFL, IEEE Trans. Appl. Supercond. 25 (2015) 1–6.

Glossary of abbreviations

ADC: adaptive combination
ASL: arterial spin labeling
B_0: static magnetic field
B_1: transverse RF magnetic field
B_1^+: transmit transverse RF magnetic field
B_{1rms}: root-mean-square amplitude of transmit transverse RF magnetic field
BOLD: blood-oxygen-level-dependent
bSSFP: balanced steady-state free precession
CAIPI: controlled aliasing in parallel imaging
CAIPIRINHA: controlled aliasing in parallel imaging results in higher acceleration
CAT: computational anatomy toolbox
CE-FAST: contrast-enhanced Fourier-acquired steady state
CEST: chemical exchange saturation transfer
$CMRO_2$: cerebral metabolic rate of oxygen consumption
CNR: contrast-to-noise ratio
CP: circularly polarized
CS: compressed sensing
CSI: chemical shift imaging
CT: computed tomography
CV: coefficient of variation
DA: density-adapted
DGE: dynamic glucose-enhanced (CEST imaging)

DLCS: dictionary learning compressed sensing
DSB: double-strand break
DTI: diffusion tensor imaging
DWI: diffusion-weighted imaging
E: RF electric field
EPI: echo-planar imaging
EPSI: echo-planar spectroscopic imaging
FDA: U.S. Food and Drug Administration
FFA: free fatty acids
FLAIR: fluid-attenuated inversion recovery
FLORET: Fermat-looped orthogonally-encoded trajectories
FOX: field of excitation
GAG: glycosaminoglycan
gagCEST: glycosaminoglycan CEST
γ*-H2AX:* gamma histone 2AX
glucoCEST: glucose CEST
GM: gray matter
GRASE: gradient and spin echo
GRE: gradient echo
ICNIRP: International Commission on Non-Ionizing Radiation Protection
IDH: isocitrate dehydrogenase
IR: inversion recovery
ISIS: imaging-selected in-vivo spectroscopy
M_0: thermal equilibrium water magnetization
MFX: microfracture
MGMT: O^6-methylguanine-DNA methyltransferase
mIP: minimum intensity projection
MPRAGE: magnetization-prepared rapid gradient echo
MP2RAGE: magnetization-prepared 2 rapid gradient echoes
MRF: magnetic resonance fingerprinting
MRI: magnetic resonance imaging
MRS: magnetic resonance spectroscopy
MRSI: magnetic resonance spectroscopic imaging
MS: multiple sclerosis
NAFL: non-alcoholic fatty liver
NMR: nuclear magnetic resonance
NOE: nuclear Overhauser effect
PINS: power independent of number of slices
PMC: prospective motion correction
PR: projection reconstruction
PROPELLER: periodically rotated overlapping parallel lines with enhanced reconstruction
PSF: point spread function
pTx: parallel transmission
QSM: quantitative susceptibility mapping
RF: radiofrequency
RMS: root mean square
RMSE: root-mean-square error
rNOE: relayed nuclear Overhauser effect
Rx: receive
SAR: specific absorption rate
SENSE: sensitivity encoding
SMS: simultaneous multi-slice imaging
SNR: signal-to-noise ratio
SOS: sum of squares
SPINS: spiral nonselective
SSB: single-strand break
SSFP: steady-state free precession
ssMT: semi-solid magnetization transfer
STA: small-tip-angle approximation
SWI: susceptibility-weighted imaging
SWIFT: sweep imaging with Fourier transformation
TE: echo time
TIAMO: time-interleaved acquisition of modes
TOF: time-of-flight
TPI: twisted projection imaging
TR: repetition time
TSE: turbo spin echo
tSNR: time-course SNR
Tx: transmit
UHF: ultra-high field ($\geq$7 T)
UTE: ultra-short echo time
uiSNR: ultimate intrinsic SNR
WM: white matter